

Analysis of Multiple Wavelength Lidar Backscatter From Cirrus

John R. Roadcap, LtCol, USAF
Phan D. Dao
Patrick J. McNicholl

1 Feb 2003

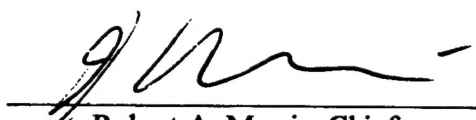
20030916 091

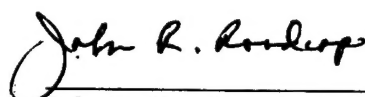
Approved for public release; distribution unlimited

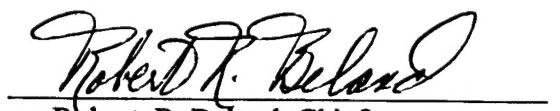


AIR FORCE RESEARCH LABORATORY
Space Vehicles Directorate
29 Randolph Rd
AIR FORCE MATERIEL COMMAND
Hanscom AFB, MA 01731-3010

This technical report has been reviewed and is approved for publication


Robert A. Morris, Chief
Battlespace Environment Division


John R. Roadcap, Lt Col, USAF
Author


Robert R. Beland, Chief
Tactical Environmental Support Branch

This document has been reviewed by the AFRL/VS Public Affairs Office (PA) and is releasable to the National Technical Information Service (NTIS).

Qualified requestors may obtain additional copies from the Defense Technical Information Center (DTIC). All others should apply to the National Technical Information Service (NTIS).

If your address has changed, if you wish to be removed from the mailing list, or if the addressee is no longer employed by your organization, please notify AFRL/VSIM, 29 Randolph Road, Hanscom AFB, MA 01731-3010. This will assist us in maintaining a current mailing list.

Do not return copies of this report unless contractual obligations or notices on a specific document require that it be returned.

REPORT DOCUMENTATION PAGE				Form Approved OMB No. 0704-01-0188		
The public reporting burden for this collection of information is estimated to average 1 hour per response, including the time for reviewing instructions, searching existing data sources, gathering and maintaining the data needed, and completing and reviewing the collection of information. Send comments regarding this burden estimate or any other aspect of this collection of information, including suggestions for reducing the burden to Department of Defense, Washington Headquarters Services, Directorate for Information Operations and Reports (0704-0188), 1215 Jefferson Davis Highway, Suite 1204, Arlington VA 22202-4302. Respondents should be aware that notwithstanding any other provision of law, no person shall be subject to any penalty for failing to comply with a collection of information if it does not display a currently valid OMB control number.						
PLEASE DO NOT RETURN YOUR FORM TO THE ABOVE ADDRESS.						
1. REPORT DATE (DD-MM-YYYY) 01-02-2003		2. REPORT TYPE Scientific Interim		3. DATES COVERED (From - To) Aug 01 - Feb 03		
4. TITLE AND SUBTITLE Analysis of Multiple Wavelength Lidar Backscatter from Cirrus				5a. CONTRACT NUMBER 10100TA1		
				5b. GRANT NUMBER None		
				5c. PROGRAM ELEMENT NUMBER 62101F		
				5d. PROJECT NUMBER 1010		
6. AUTHORS Roadcap, John R., Lt Col, USAF Dao, Phan D., PhD McNicholl, Patrick J.*, PhD *Boston College Chestnut Hill, MA 02467				5e. TASK NUMBER 0T		
				5f. WORK UNIT NUMBER A1		
7. PERFORMING ORGANIZATION NAME(S) AND ADDRESS(ES) Air Force Research Laboratory (AFRL/VSBL) 29 Randolph Road Hanscom AFB, Massachusetts 01731-3010				8. PERFORMING ORGANIZATION REPORT NUMBER AFRL-VS-TR-2003-1567		
9. SPONSORING/MONITORING AGENCY NAME(S) AND ADDRESS(ES)				10. SPONSOR/MONITOR'S ACRONYM(S)		
				11. SPONSOR/MONITOR'S REPORT NUMBER(S)		
12. DISTRIBUTION/AVAILABILITY STATEMENT Approved for Public Release ; Distribution Unlimited						
13. SUPPLEMENTARY NOTES						
14. ABSTRACT Lidar backscatter from cirrus cloud particles at multiple wavelengths (532 nm, 1064 nm, 10591 nm) was measured at Hanscom AFB, MA in August 2001. Range-resolved measurements were made for several hours daily at altitudes from 9 km to 16 km over a temperature range of -30C to -70C. Three days were selected for study -- 9 August, 14 August, and 16 August 2001. Cirrus backscatter measurements were analyzed in combination with scattering theory for ice spheres and long ice cylinders to better understand their behavior. For 532 nm and 1064 nm, the logarithm (base 10) of backscatter magnitudes (/m-sr) ranged from -4.5 to -6.0 within the cloud area while backscatter magnitudes for 10591 nm ranged from -6.5 to -8.5. Agreement existed between the range of measured backscatter wavelength ratio magnitudes and those computed from scattering theory but no consistent information was discerned concerning modal particle sizes. Calculations of cirrus ice water content, extinction-to-backscatter ratio, and optical depth yielded magnitudes consistent with published values for in-situ and remote measurements.						
15. SUBJECT TERMS lidar backscatter cirrus particles scattering theory						
16. SECURITY CLASSIFICATION OF:			17. LIMITATION OF ABSTRACT	18. NUMBER OF PAGES	19a. NAME OF RESPONSIBLE PERSON	
a. REPORT	b. ABSTRACT	c. THIS PAGE	UU	93	John R. Roadcap	
UNCLASS	UNCLASS	UNCLASS			19b. TELEPHONE NUMBER (Include area code) 781 377 3016	

Contents

1. INTRODUCTION.....	1
2. BACKSCATTER FOR SINGLE, INDEPENDENT SCATTERERS.....	1
3. LIDAR CHARACTERISTICS AND MEASURED LIDAR BACKSCATTER.....	3
4. MEASUREMENT LOCATION AND SYNOPTIC WEATHER CONDITIONS.....	6
5. CALCULATION OF BACKSCATTER COEFFICIENT FROM SCATTERING THEORY.....	18
6. COMPARISON OF MEASURED LIDAR BACKSCATTER RATIOS WITH THEORY.....	22
7. ESTIMATES OF ICE WATER CONTENT FROM CIRRUS BACKSCATTER.....	39
8. RANGE-RESOLVED EXTINCTION IN CIRRUS AT LIDAR WAVELENGTHS.....	46
9. SUMMARY AND CONCLUSION.....	56
REFERENCES.....	59
APPENDIX A CALCULATION OF SCATTERING COEFFICIENTS FOR A SPHERE.....	61
APPENDIX B CALCULATION OF SCATTERING EFFICIENCIES FOR A LONG CIRCULAR CYLINDER (ROD).....	67
APPENDIX C NORMALIZED BACKSCATTER AND EXTINCTION KERNEL FUNCTIONS FOR ICE SPHERES.....	73
APPENDIX D RAYLEIGH BACKSCATTER CROSS-SECTION AND VOLUME BACKSCATTER COEFFICIENT FOR AIR.....	77

Illustrations

1. Incident light from below on a scattering particle or object. θ represents the scattering angle.....	2
2. Incident light from below on a long cylinder. θ represents the scattering angle and α is the angle of obliquity.	2
3. 300 mb. analysis 10 August/00Z 2001.....	7
4. 300 mb. analysis 15 August/00Z 2001.....	8
5. 300 mb. analysis 17 August/00Z, 2001.....	9
6. Time vs. altitude cross-section of lidar backscatter return for 10.6 μm for 9 August 2002.....	11
7. Time vs. altitude cross-section of lidar backscatter return for 10.6 μm for 14 August 2002.....	12
8. Time vs. altitude cross-section of lidar backscatter return for 10.6 μm for 16 August 2002.....	13
9. Radiosonde temperature (C) and relative humidity profile (%) for 9 August 19 GMT Hanscom AFB, MA. On the right is the diagnosed area-averaged vertical velocity (cm s^{-1}) for 10 Aug 00Z.....	14
10. Radiosonde temperature (C) and relative humidity (%) profile 14 Aug 19 GMT Hanscom AFB MA.....	15
11. Radiosonde temperature (C) and relative humidity (%) vertical profile: 16 August 19 GMT Hanscom AFB, MA	16
12. Normalized modified gamma particle size distribution calculated from Eq. (12) used to represent the cirrus cloud.....	21
13. $\log_{10}(\beta_r)$ for 9 August 2001: contour intervals are -5.8, -5.5, -5.0, -4.5 ($\text{m}^{-1} \text{sr}^{-1}$).....	24
14. $\gamma_r(10.6\mu\text{m}/0.532\mu\text{m})$ for 9 August 2001 contour interval: 0.003, 0.005, 0.007, 0.01.....	24
15. $\log_{10}(\beta_r)$ for 9 August 2001: contour intervals: -6.0, -5.5, -5.0 ($\text{m}^{-1} \text{sr}^{-1}$).....	26
16. $\gamma_r(10.6\mu\text{m}/0.532\mu\text{m})$ for 9 August 2001 contour interval: 0.003, 0.005, 0.007, 0.01.....	26
17.. Backscatter coefficient ratio γ_r for ice spheres as function of equivalent radius for $\lambda=10.6\mu\text{m}$, 0.532 μm	27
18. Measured $\gamma_r(1.064/0.532)$ for 9 August: contour interval: 0.5, 0.75, 1.0, 1.25.....	28
19. Backscatter ratio γ_r for ice spheres as function of equivalent radius for $\lambda=1.064\mu\text{m}$, 0.532 μm	29
20. $\log_{10}(\beta_r)$ at $\lambda=0.532\mu\text{m}$ for 14 August 2001: contour intervals -5.8, -5.5, -5.0, -4.5 ($\text{m}^{-1} \text{sr}^{-1}$).....	30
21. $\log_{10}(\beta_r)$ at 10.6 μm for 14 August contour intervals -8.5, -8.0, -7.5, -7.0, -6.5 ($\text{m}^{-1} \text{sr}^{-1}$).....	30

22. $\log_{10}(\beta_{\pi})$ at $\lambda = 1.06 \mu\text{m}$ for 14 August: contour intervals: -6.5, -6.0, -5.5, -5.0, -4.5 ($\text{m}^{-1}\text{sr}^{-1}$).....	31
23. $\gamma_{\pi}(10.6/0.532)$ for 14 August. contour interval: 0.003, 0.01, 0.1, 0.3.....	31
24. $\gamma_{\pi}(1.064/0.532)$ for 14 August 2002: contour interval: 0.01, 0.25, 0.5, 1.0.....	32
25. $\log_{10}(\beta_{\pi})$ at $\lambda = 0.532 \mu\text{m}$ for 16 August 2001: contour intervals -6.0, -5.5, -5.0, -4.5.....	32
26. $\log_{10}(\beta_{\pi})$ at $\lambda = 10.6 \mu\text{m}$ for 16 August 2001 contour interval: -8.5, -8.0, -7.5, -7.0 ($\text{m}^{-1}\text{sr}^{-1}$).....	33
27. $\log_{10}(\beta_{\pi})$ at $\lambda = 1.064 \mu\text{m}$ for 16 August 2001 contour intervals: -6.5, -6.0, -5.5, -5.0, -4.5.....	33
28. $\gamma_{\pi}(10.6/0.532)$ analysis for 16 August 2001: contour interval 0.003, 0.01, 0.10.....	34
29. $\gamma_{\pi}(1.064/0.532)$ for 16 August 2001: analysis for contour intervals: 0.1, 0.5, 1.0, 1.5.....	34
30. Backscatter ratio γ_{π} for long perpendicularly-oriented ice cylinders as function of cylinder radius for $\lambda=10.6 \mu\text{m}$, $0.532 \mu\text{m}$	35
31. Backscatter ratio γ_{π} for long perpendicularly-oriented cylinders as function of cylinder diameter for $\lambda=1.064 \mu\text{m}$, $0.532 \mu\text{m}$	36
32. Ice water content (iwc) calculations for 9 Aug using backscatter measurements and assuming a modified gamma polydispersion of ice spheres.....	41
33. Ice water content (g m^{-3}) calculations for 14 Aug using backscatter measurements and assuming a modified gamma polydispersion of ice spheres.....	42
34. Ice water content (g m^{-3}) calculations for 16 Aug using backscatter measurements and assuming a modified gamma polydispersion of ice spheres.....	43
35. Ice water content (iwc) calculations using backscatter measurements and assuming a polydispersion of long circular cylindrical scatterers.....	44
36. Time series of ρ_{iwc} computed for 9 August at 14 km from the derived β_{ext} measurements for $\lambda = 0.532 \mu\text{m}$ for the two equivalent radii $10 \mu\text{m}$ and $100 \mu\text{m}$	45
37. Time series of ice water content ρ_{iwc} calculated from extinction and backscatter measurements at $\lambda = 0.532 \mu\text{m}$ for the two equivalent radii $10 \mu\text{m}$ and $100 \mu\text{m}$	45
38. Rayleigh volume backscatter coefficient β_{π} for air molecules for 9 August 2001 19 GMT Hanscom AFB.....	50
39. Extinction to backscatter ratio S : Measured vs. theoretical calculations of S at $\lambda = 0.532 \mu\text{m}$ for polydispersion of ice spheres (dashed line) and long ice cylinders with light at perpendicular incidence (solid line).....	51
40. Measured β_{ext} (km^{-1}) at $\lambda = 0.532 \mu\text{m}$ on 9 August 2001 contour intervals: 0.1, 0.3, 0.5 km^{-1}	52

41. Measured β_{ext} (km^{-1}) at $\lambda = 0.532 \mu\text{m}$ for 14 August 2001: contour intervals: 0.1, 0.3, 0.5 km^{-1}	53
42. Measured β_{ext} (km^{-1}) at $\lambda = 0.532 \mu\text{m}$ for 16 August 2001: contour intervals: 0.1, 0.3, 0.5 km^{-1}	54
43. Time series of measured cirrus optical depth τ_c ($\lambda = 0.532 \mu\text{m}$) for 9 August, 14 August, and 16 August 2002	55
Figure C1. $K_{\pi}(r, \lambda, m)$ (normalized) for wavelengths $\lambda = 0.532 \mu\text{m}$, 1.064 μm , and 10.6 μm	74
Figure C2. $K_{ext}(r, \lambda, m)$ (normalized) for wavelengths $\lambda = 0.532 \mu\text{m}$, 1.064 μm , and 10.6 μm	74

Tables

1. Lidar Characteristics.....	4
2. Refractive Index for Ice.....	18
3. Numerical Integration Limits for Size Parameter x as a Function of Wavelength and Particle Type.....	20
4. Measured Lidar Cirrus Backscatter Coefficient $\log_{10}(\beta_{\pi})$ Ranges for 9, 14, 16 August 2001.....	37
5. Measured Lidar Cirrus Backscatter Coefficient Ratio γ_{π} Ranges for 9, 14, 16 August 2001.....	38

Acknowledgments

The authors are grateful to Dr. Robert R. Beland of the Air Force Research Laboratory (AFRL) for his continual encouragement and support of this work. The authors also gratefully acknowledge the skilled contributions of MSgt Mitchell H. Laird of AFRL and Dr. Anthony Dentamaro of Boston College, without whose help the lidar measurements would not have been possible. The expert radiosonde launches by Mr. George Clement of Utah State University are very much appreciated. Portions of the described measurements were supported by the U.S. Missile Defense Agency (MDA/SER).

1. INTRODUCTION

Lidar backscatter from cirrus cloud particles at multiple wavelengths was measured on several days at Hanscom AFB, Massachusetts in August 2001. The range-resolved measurements were made for several hours each day at altitudes from 9 km to 16 km over a temperature range of -30°C to -70°C . The wavelengths of the lidar measurements were $0.532\text{ }\mu\text{m}$, $1.064\text{ }\mu\text{m}$, and $10.6\text{ }\mu\text{m}$. Lidar backscatter provides useful information on the vertical structure of cirrus and its temporal variation. Backscatter measurements are analyzed using scattering theory calculations to better understand their behavior with respect to wavelength and characteristic cirrus particle sizes. The backscatter also yields information on microphysical and optical properties of cirrus such as number density (ice water content), extinction, and extinction-to-backscatter ratio, which can be useful in laser propagation and atmospheric science applications. This report describes these measurements, relevant calculations, and their comparison with previously-published results.

2. BACKSCATTER FOR SINGLE, INDEPENDENT SCATTERERS

Backscatter is the efficiency of an object for scattering electromagnetic radiation back toward the source at the scattering angle $\theta = \pi$. Figure 1 (after van de Hulst, 1957) depicts light from below, incident on a scattering particle and an associated scattering angle. Backscatter is quantitatively represented as the scattering cross section for scattering angle $\theta = \pi$ divided by the object's geometrical cross-section. For a homogeneous sphere, the backscatter efficiency Q_{bsct} can be expressed in terms of the scattering amplitude function S_1 as

$$Q_{bsct} = \frac{4|S_1(\pi)|^2}{x^2} \quad (1)$$

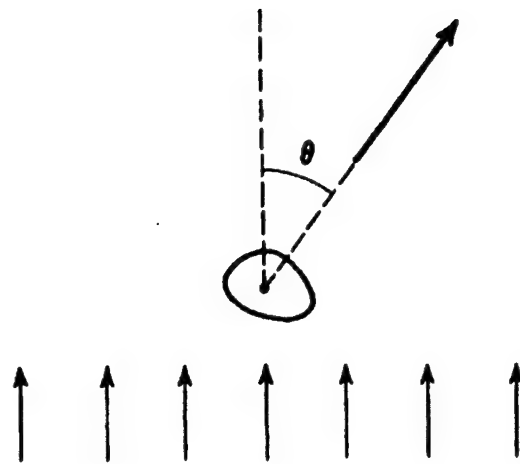


Figure 1. Incident light from below on a scattering particle or object. θ represents the scattering angle. (after van de Hulst, 1957)

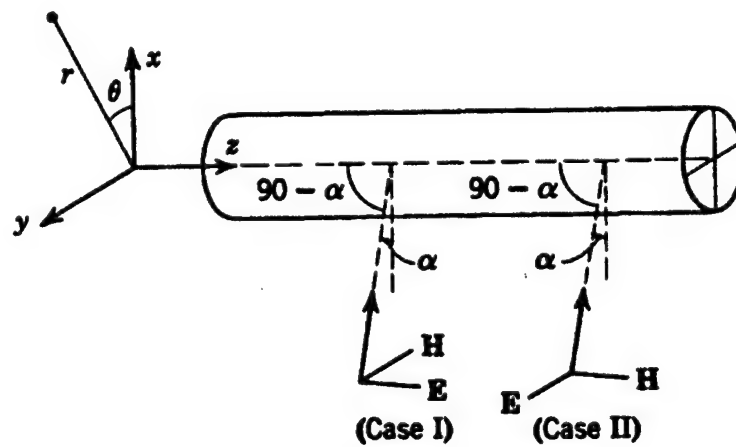


Figure 2. Incident light from below on a long cylinder. θ represents the scattering angle and α is the angle of obliquity. (after van de Hulst, 1957)

where S_1 is the scattering amplitude function evaluated at $\theta = \pi$ and $x = kr = \frac{2\pi r}{\lambda}$ is the particle size parameter (van de Hulst, 1957). Here, λ is the wavelength of incident radiation and r is the sphere radius. The scattering amplitude S_1 is a function of the incident energy wavelength λ , particle size or radius r , and particle refractive index m , which is a complex number. For a collection of spheres of different sizes, i.e. a polydispersion, the volume backscatter coefficient is written as

$$\beta_\pi = \int_0^\infty \frac{Q_{bsct}(r, \lambda, m)}{4\pi} n(r) \pi r^2 dr \quad (\text{m}^{-1} \text{ sr}^{-1}) \quad (2)$$

where $n(r)$ is the particle number density size distribution (the number of particles $\text{m}^{-3} \mu\text{m}^{-1}$). The variables shown in Eqs. (1) and (2) will be described further in this report in addition to the scattering geometry associated with light incident from below on a long cylinder, as depicted in Figure 2.

3. LIDAR CHARACTERISTICS AND MEASURED LIDAR BACKSCATTER

Lidar provides measurements of range-gated or range-resolved backscatter from scattering particles at optical wavelengths. For the measurements described in this report, two lidar systems were used to provide the range-resolved backscatter. The first system employed was a Nd:YAG lidar capable of backscatter measurements at three wavelengths (0.355 μm , 0.532 μm , and 1.064 μm). However, only two wavelengths, 0.532 μm and 1.064 μm , were operating during the described measurements. A second lidar, a CO₂ heterodyne detection lidar, was used and made range-resolved backscatter measurements at 10.591 μm . The two lidar systems were physically adjacent to one another during these measurements. Table 1 lists the operating characteristics of each lidar system.

Table 1. Lidar Characteristics

Lidar	Nd:YAG	CO ₂
Wavelengths (μm)	0.532, 1.064	10.591
Telescope aperture diam.	30 cm	30 cm
Range gate	120 m	120 m
Pulse rep. frequency	30 Hz	30 Hz
Pulse integration period	30 sec	30 sec
Pulse Energy	250 mJ (0.532 μm) 400 mJ (1.064 μm)	60 mJ
Nominal meas. range	> 100 km	60 km
Full hemispheric field-of-view scan (both lidars)		

While these lidars can take measurements at any azimuth or elevation angle above 0°, most of the lidar cirrus backscatter measurements were usually taken at near-zenith elevation angles. The exceptions were for most contrail measurements and for some distant cirrus shields, where the lidar pointing between systems was generally co-aligned. However, these off-vertical axis measurements are not analyzed in this report. In addition to the lidar measurements, radiosondes were launched near the lidars every 3 hours during the measurement period. The radiosondes measured vertical profiles of temperature, relative humidity, pressure, and horizontal wind velocity from the surface to 20 km above sea level.

The lidar volume backscatter coefficient is calculated from the CO₂ heterodyne lidar measurements by

$$\beta_{\pi}(z) = k_{cal} \cdot \frac{P_r(z)}{E_p} \quad (m^{-1}sr^{-1}) \quad (3)$$

where k_{cal} is the absolute calibration coefficient ($s \, m^{-1} \, sr^{-1}$), P_r is the range- and extinction-compensated power ($J \, s^{-1}$), and E_p is the transmitted pulse energy (J). For the Nd:YAG lidar measurements, the measured lidar backscatter is determined as

$$\beta_{\pi}(z) = \beta_{\pi \, Rayleigh} \cdot \frac{P_r(z)}{P_r(clear)} \quad (m^{-1}sr^{-1}) \quad (4)$$

where $\beta_{\pi \text{ Rayleigh}}$ is the Rayleigh volume backscatter coefficient for air molecules and $P_r(\text{clear})$ is the range-compensated power in the clear air immediately at the base of the cloud. Rayleigh backscatter from air molecules is a function of wavelength and air density and varies as λ^{-4} . At cirrus altitudes (10 km), typical Rayleigh backscatter values are $\sim 7 \times 10^{-7} \text{ m}^{-1} \text{ sr}^{-1}$ at $0.532 \text{ }\mu\text{m}$ and $\sim 6 \times 10^{-8} \text{ m}^{-1} \text{ sr}^{-1}$ at $1.064 \text{ }\mu\text{m}$. The measured lidar power return P_r was corrected for range diminishment using the $1/r^2$ formula and compensated for extinction. The extinction compensation was accomplished using a vertical profile of laser line molecular transmittance for each laser wavelength computed from the HITRAN data base (Rothman et al, 1992) and radiosonde input data (pressure, temperature, and relative humidity) nearest in time to the measurements. Using these, a calibrated backscatter profile was produced. While the Nd:YAG lidar is self-calibrating using the Rayleigh backscatter signal, the calibration coefficient k_{cal} required for the CO_2 lidar measurements was determined from time integrated target particle board backscatter measurements and laboratory analysis of the particle target board samples. For both the Nd:YAG and CO_2 lidar, the returned power is integrated over a 30 sec period to increase the sensitivity of the signal. For the CO_2 heterodyne system, typical measured backscatter magnitudes from cirrus are $\sim 10^{-9} \text{ m}^{-1} \text{ sr}^{-1}$ while typical cirrus backscatter magnitudes from the Nd:YAG lidar at $0.532 \text{ }\mu\text{m}$ are $\sim 10^{-6} \text{ m}^{-1} \text{ sr}^{-1}$.

There are several factors that can affect the lidar backscatter measurement and its interpretation. For CO_2 lidar backscatter, the accuracy of the calibration coefficient is probably only within $\pm 20\%$ of its true value. Non-linear effects or saturation of the power return signal also must be considered for both lidars. For both lidar systems, specular reflection from flat cirrus particles or plates, which can produce jumps of two to three orders of magnitude in the measured backscatter, can usually be avoided by tilting the lidar beam slightly off vertical. In comparing backscatter magnitudes at different wavelengths, changes in particle composition or particle morphology within the cloud during the measurements must also be considered.

4. MEASUREMENT LOCATION AND SYNOPTIC WEATHER CONDITIONS

The lidar and radiosonde measurements described in this report were made at Hanscom Air Force Base which is located in northeast Massachusetts at latitude $42^{\circ} 27' N$, longitude $71^{\circ} 16' W$ at 70 m above sea level. Lidar measurements were made on nine days covering the period 7 August 2001 – 30 August 2001. The measurement site experienced air mass types of different origin (maritime tropical, Canadian, etc.) during this period which resulted in changes in the tropopause height between days. Cirrus was observed during the nine days associated with deep convection, weak waves in the synoptic-scale westerly flow, and surface frontal zones and jet streams. The daily measurement periods generally ran from 1700 UTC – 2400 UTC.

Three measurement days were selected for study -- 9 August, 14 August, and 16 August. These were days where extended periods of relatively uniform cirrus occurred that were not associated with deep convection. On these days, temperatures at the cirrus measurement altitudes ranged from $-30^{\circ}C$ to $-70^{\circ}C$ and the tropopause height ranged from ~ 13 km to 15.5 km.

On 9 August, the measurement area was dominated by a very warm, humid air mass in the troposphere with weak, westerly zonal flow at upper levels. This is depicted in Figure 3 which is a contour plot of the geopotential height and wind speed on the 300 mb pressure surface. Extensive cirrus was observed from 1300L – 1800L. The cirrus-generating mechanism was likely associated with a weak synoptic scale wave in the upper tropospheric westerly flow. With a tropopause located near 15.5 km, the cirrus was measured at altitudes from 12 to 15.5 km. On 14 August, a Canadian air mass dominated the region and a relatively strong polar jet stream axis oriented SW – NE was anchored over eastern Massachusetts (see Figure 4) with peak wind speeds exceeding 50 m/s from 9 km to 13 km altitude as measured by radiosonde. A distinct cirrus shield was associated with the jet stream and the shield's trailing edge lay just west of Hanscom AFB. The tropopause was lower on 14 August compared to 9 August with the

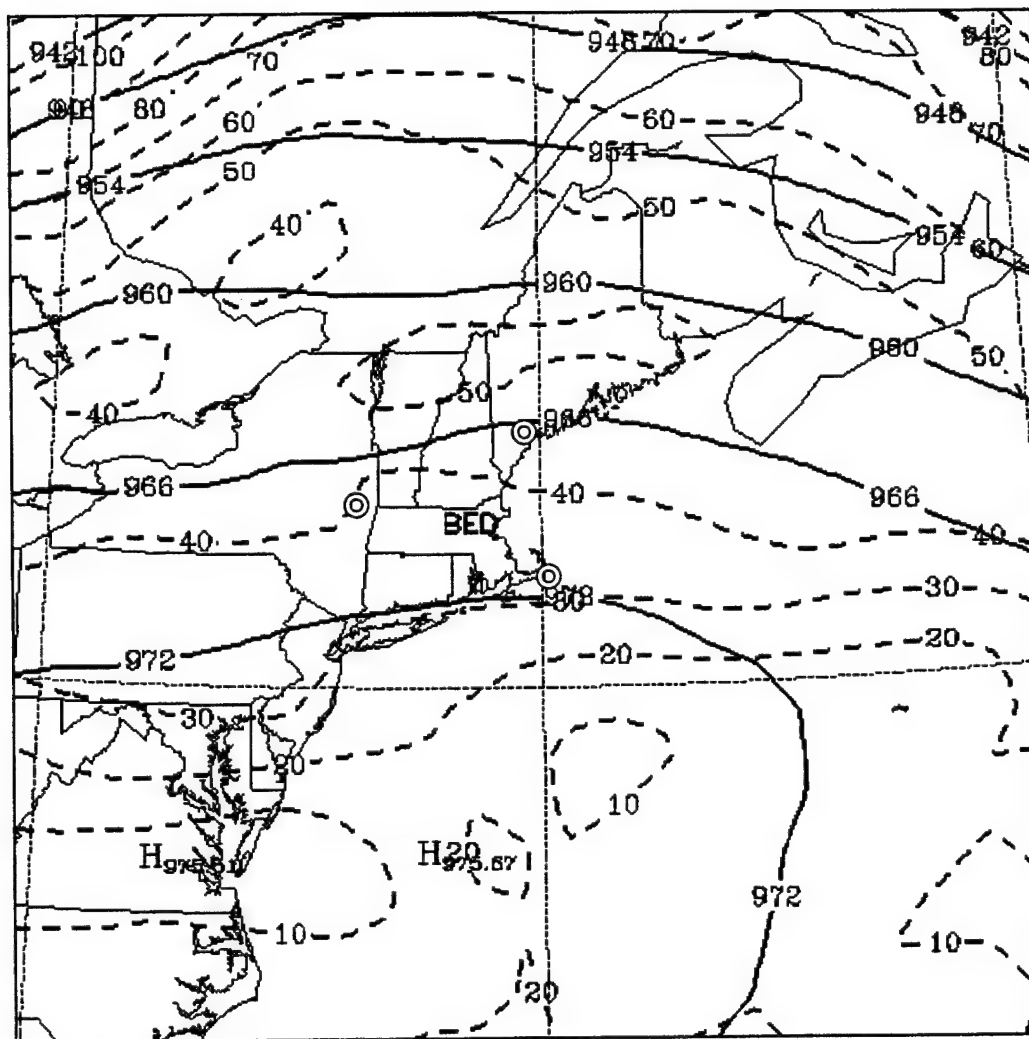


Figure 3. 300 mb. Analysis 10 August/00Z 2001. The solid lines depict geopotential height contours at 300 mb (units of decameters). The dashed lines denote wind speed in knots. Hanscom AFB is denoted by the identifier **BED**. Concentric circles show location of synoptic radiosonde sites used to compute area-averaged vertical velocity.

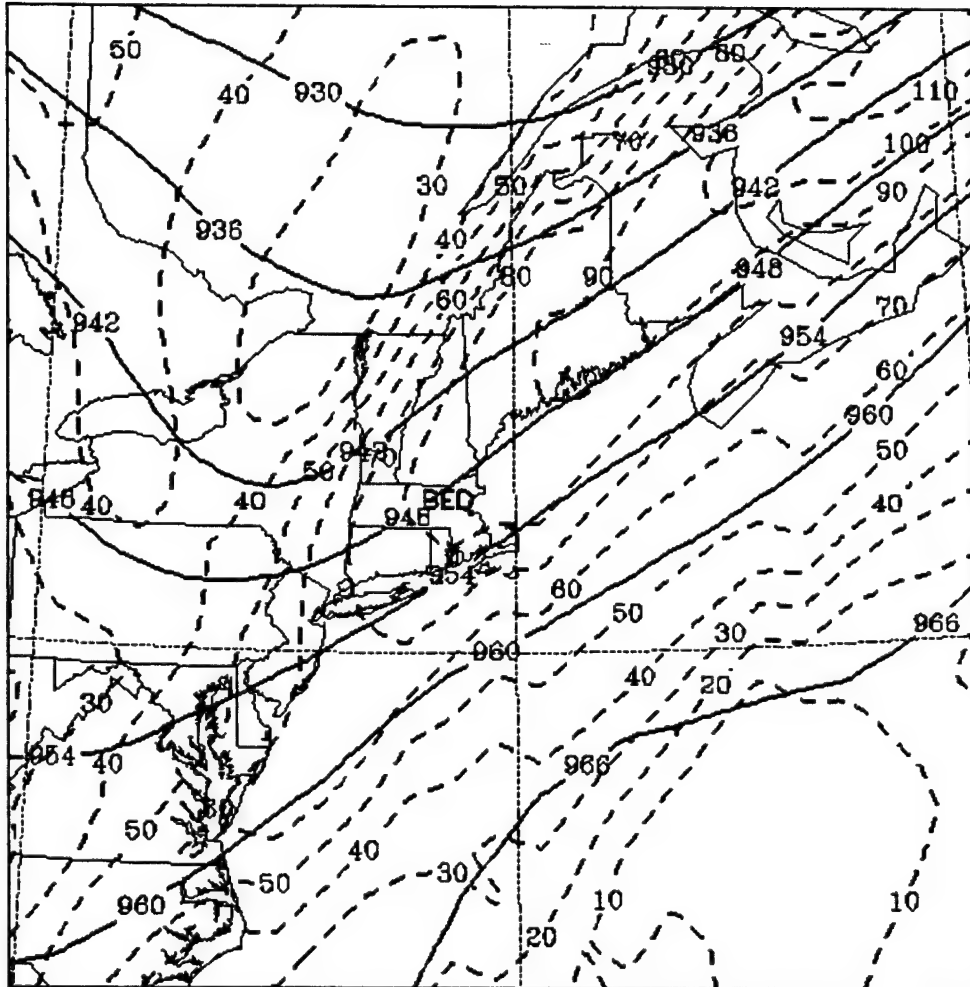


Figure 4. 300 mb. Analysis 15 August/00Z 2001 The solid lines depict geopotential height contours at 300 mb (units of decameters). The dashed lines depict wind speed in knots. Hanscom AFB is denoted by the identifier **BED**.

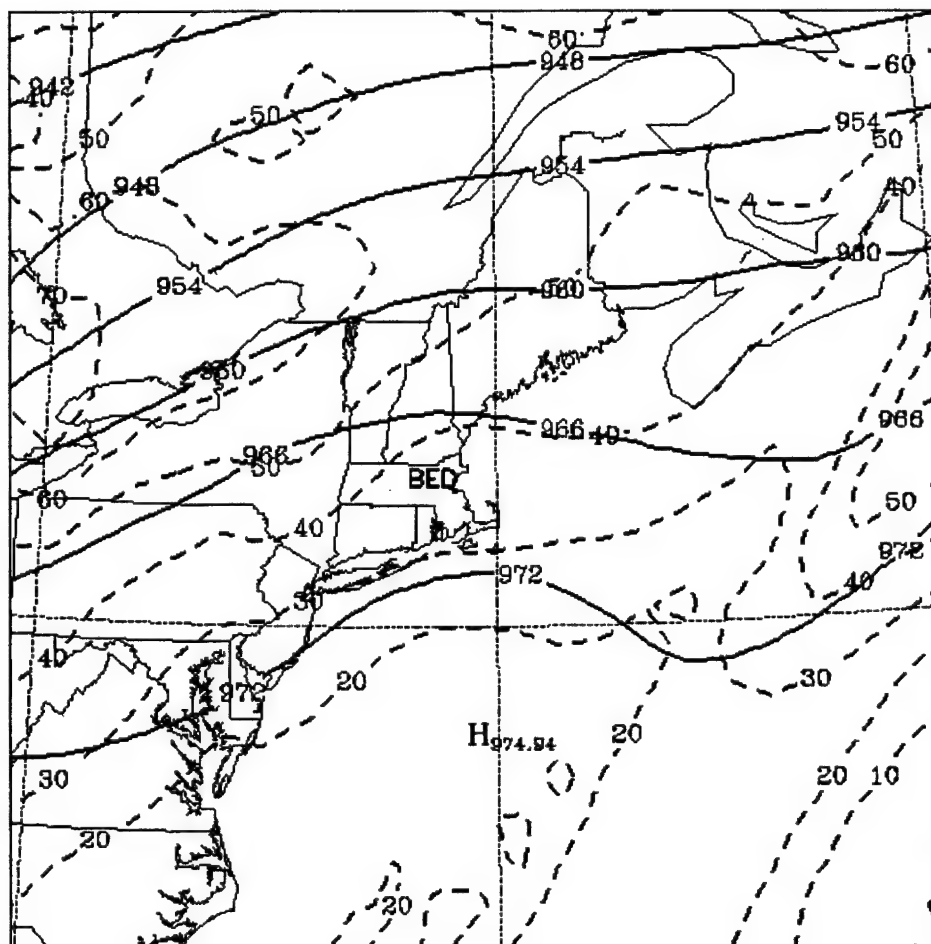


Figure 5. 300 mb. Analysis 17 August/00Z 2001 The solid lines depict geopotential height contours at 300 mb (units of decameters). The dashed lines depict wind speed in knots. Hanscom AFB is denoted by the identifier **BED**.

tropopause altitude being 13 km. On 16 August, the polar jet stream axis had moved well east of Massachusetts (see Figure 5) along with its associated cirrus shield.

However, an extensive area of scattered to broken cirrus ahead of a cold front in the Upper Midwest advanced into New England and persisted during most of the measurement period. The area remained under the influence of a modified Canadian air mass and the tropopause altitude increased slightly to 13.5 km. No jet stream structure was observed and weak westerly flow dominated through the troposphere with wind speeds remaining at or below 20 m/s.

Three daily samples of time vs. altitude profiles of uncalibrated lidar backscatter imagery for 10.591 μm wavelength are shown in Figures 6, 7, and 8. The imagery uses backscatter profiles which are produced approximately every 30 seconds. The light colored areas denote backscatter higher than the detector noise floor. The areas of enhanced backscatter below 4 km are associated with haze or aerosol particles.

Figures 9, 10, and 11 are plots of temperature and relative humidity as measured by the Hanscom AFB radiosonde launches. Area-averaged vertical velocity profiles are also plotted, which are diagnosed from 00Z radiosonde profiles forming a triangle – Albany, New York (ALB), Chatham, Massachusetts (CHH), and Gray, Maine (GYX) -- whose sides enclose Hanscom (BED) (see Figure 3). Vertical velocity is calculated from this triangle using the kinematic method (O'Brien, 1970). These radiosonde launches occurred approximately two to four hours after the cessation of daily lidar measurements.

On 9 August, the tropopause height was approximately 15 km, the base of the cirrus backscatter was evident at ~ 12.5 km and the top of the cirrus backscatter was approximately 15 km. This corresponds to a temperature range of -50°C to -70°C (see Figure 9). The tropopause height also serves to cap the upper altitude of the cirrus. On 14 August, the tropopause height was about 13 km (see Figure 10) and the cirrus backscatter extended from 9 km to 13 km (Figure 7). This corresponded to a temperature range of approximately -30°C to -60°C . Note the vertical striations of cirrus backscatter

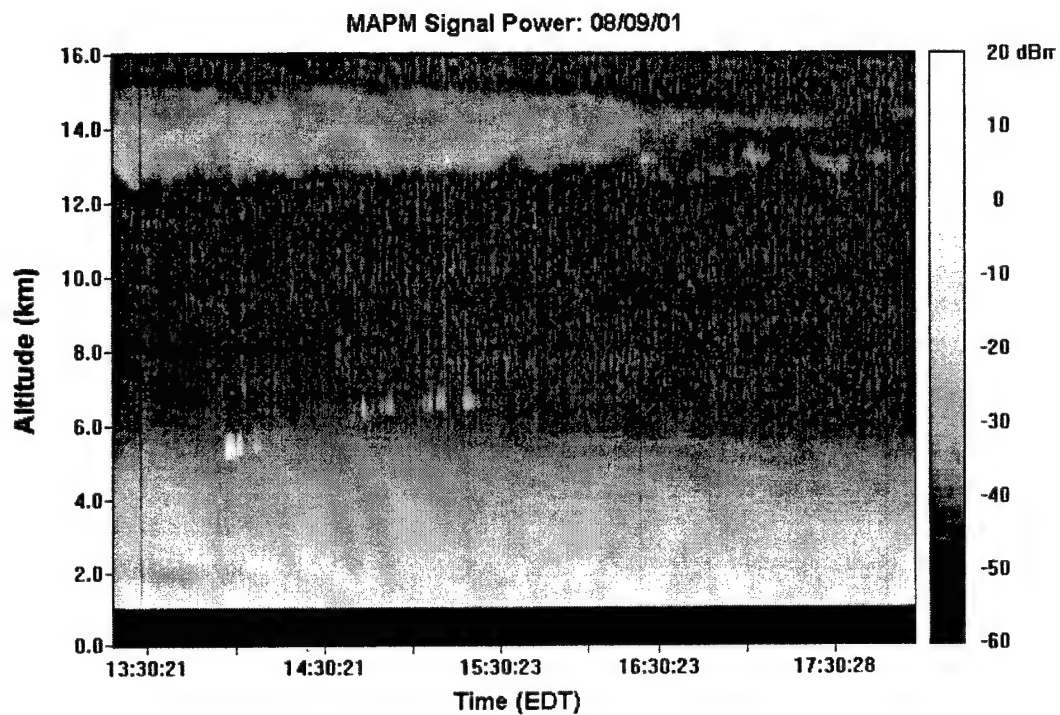


Figure 6. Time vs. altitude Cross-section of Lidar Backscatter Return for $10.6 \mu\text{m}$ for 9 August 2002. Cirrus clouds are observed above 12 km. Lighter colored areas below 7 km are associated with returns from haze particles and water droplet clouds.

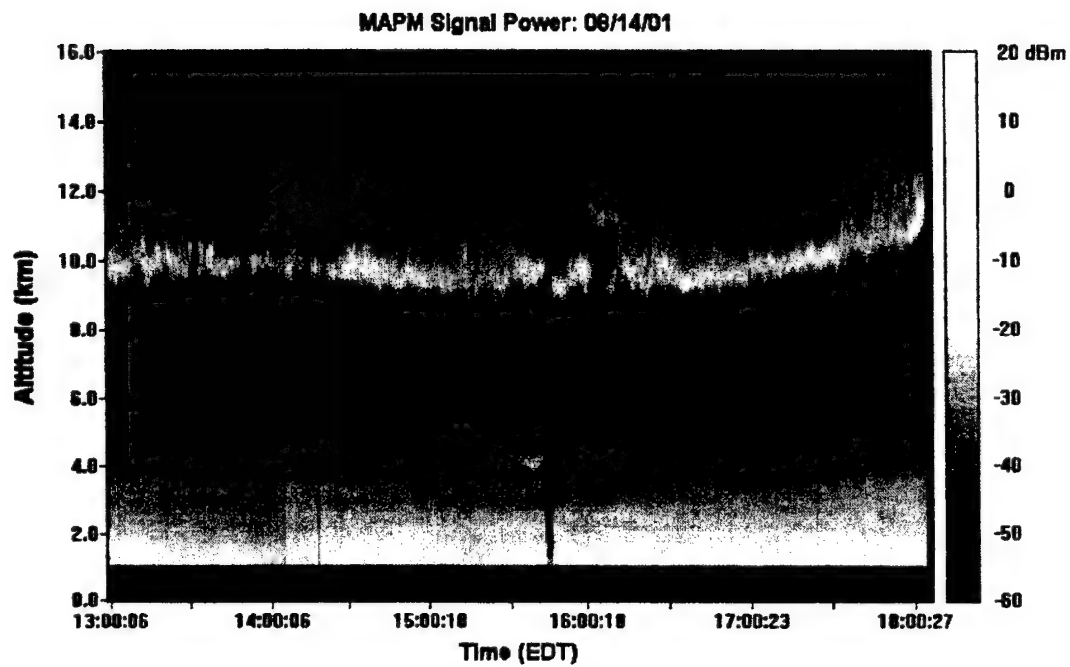


Figure 7. Time vs. Altitude Cross-section of Lidar Backscatter Return for $10.6\text{ }\mu\text{m}$ for 14 August 2002. Cirrus clouds are observed from about 9 km to 11.5 km. Lighter colored areas below 5 km are associated with returns from haze particles.

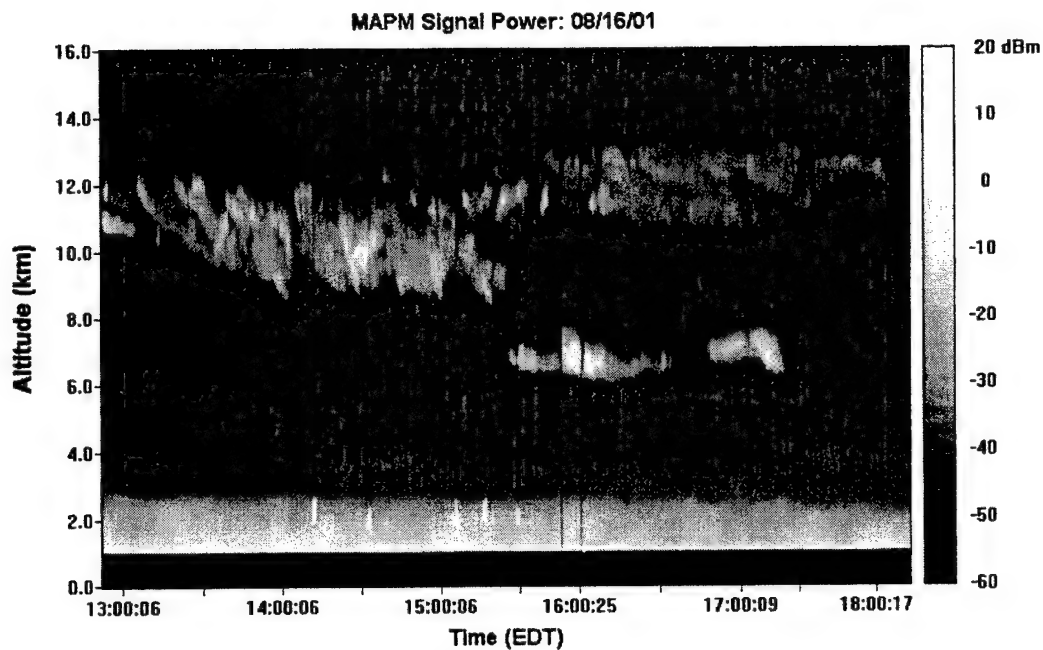


Figure 8. Time vs. Altitude Cross-section of Lidar Backscatter Return for $10.6\ \mu\text{m}$ for 16 August 2002. Cirrus clouds are observed from about 9 km to 13 km. Lighter colored areas below 7 km are associated with returns from water droplet clouds (cumulus and altostratus) and haze particles below 3 km.

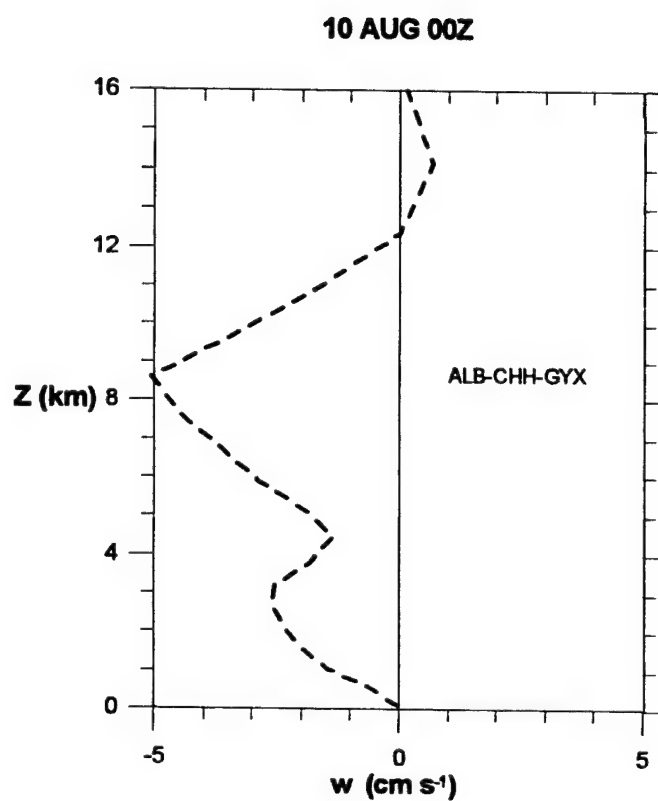
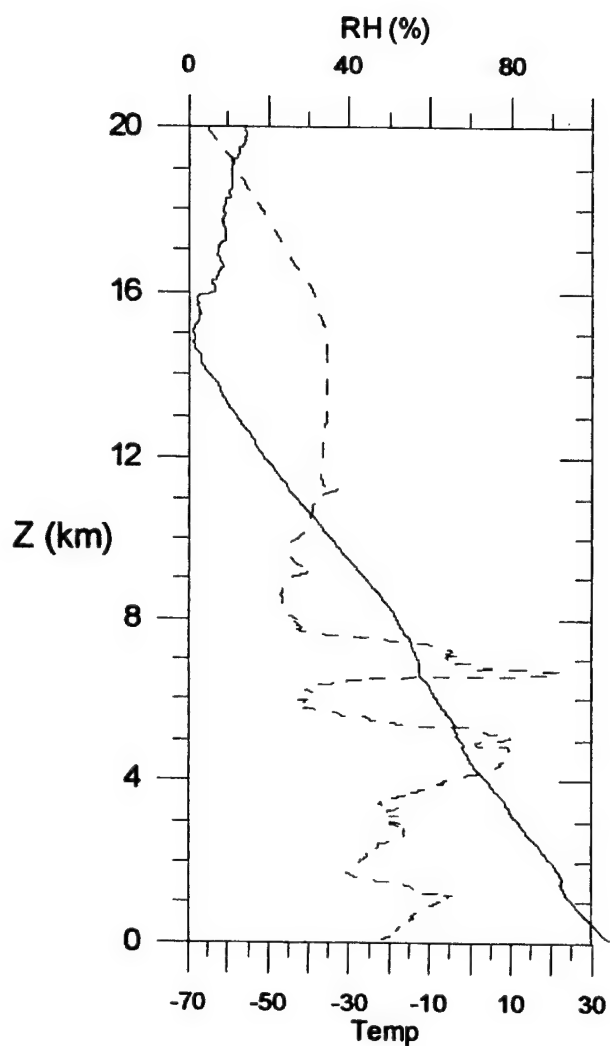


Figure 9. Radiosonde Temperature (C) and Relative Humidity Profile (%) for 9 August 19 GMT, at Hanscom AFB, MA. On the right is the diagnosed area-averaged vertical velocity (cm s^{-1}) for 10 Aug

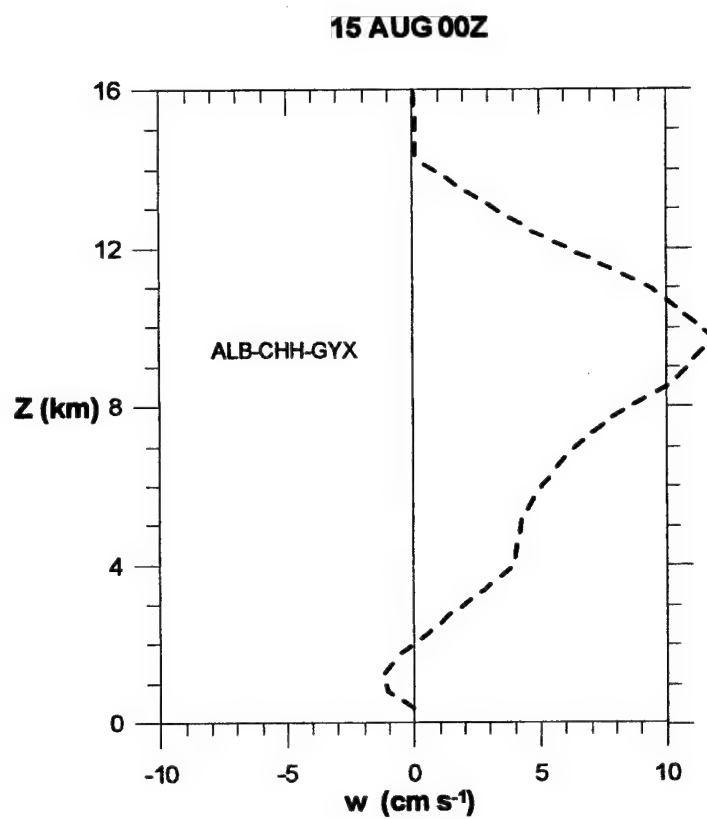
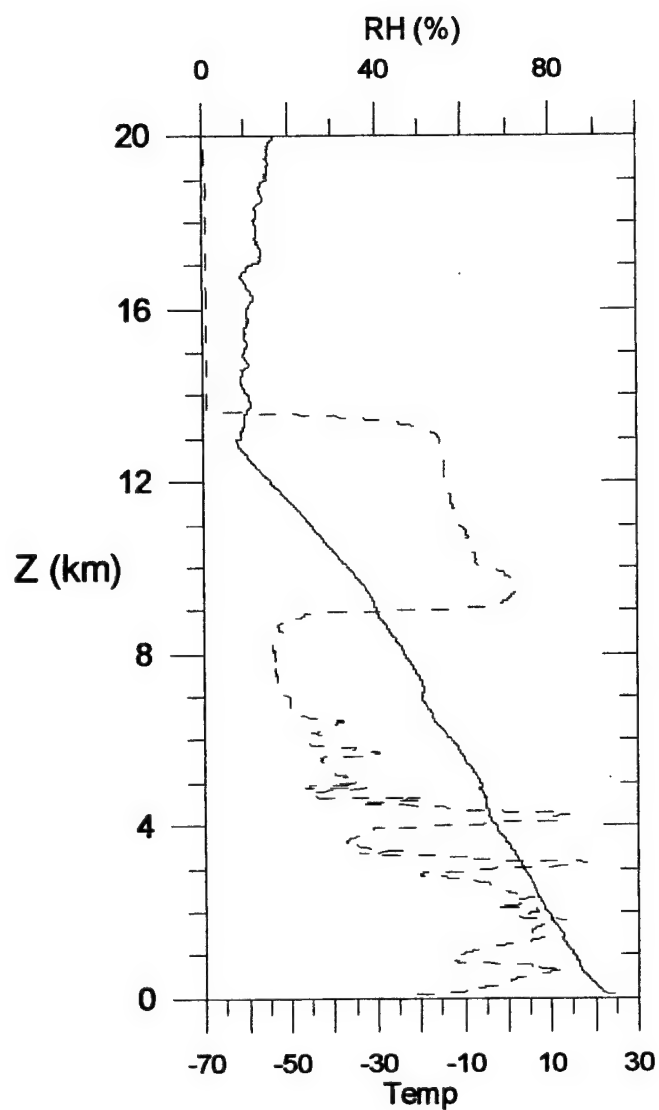


Figure 10. Radiosonde temperature (C) and Relative Humidity (%) Profile 14 Aug 19 GMT, at Hanscom AFB, MA. On the right is the diagnosed area-averaged vertical velocity (cm s^{-1}) for 15 Aug 00Z

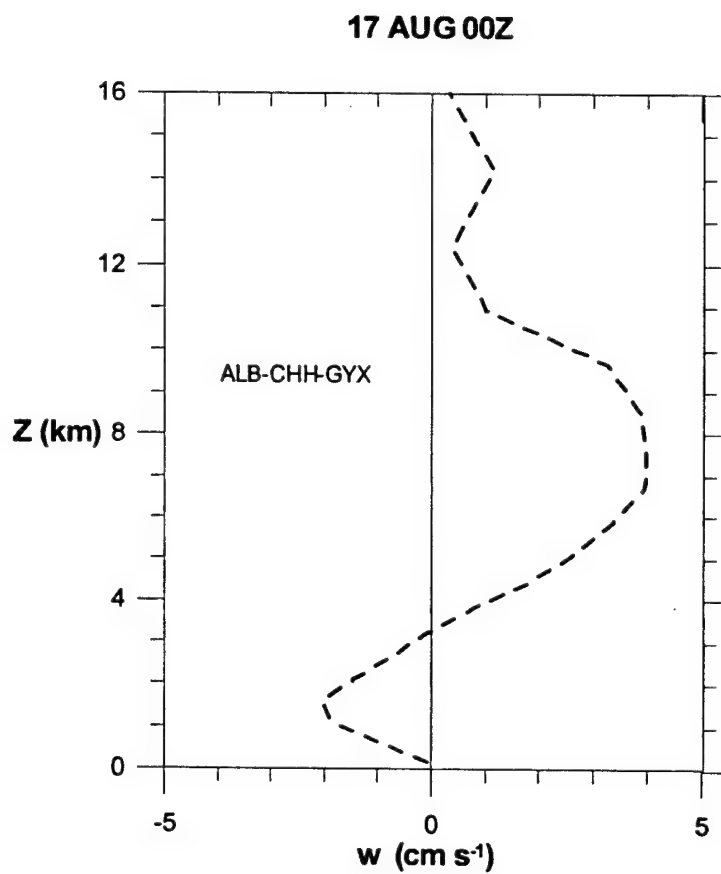
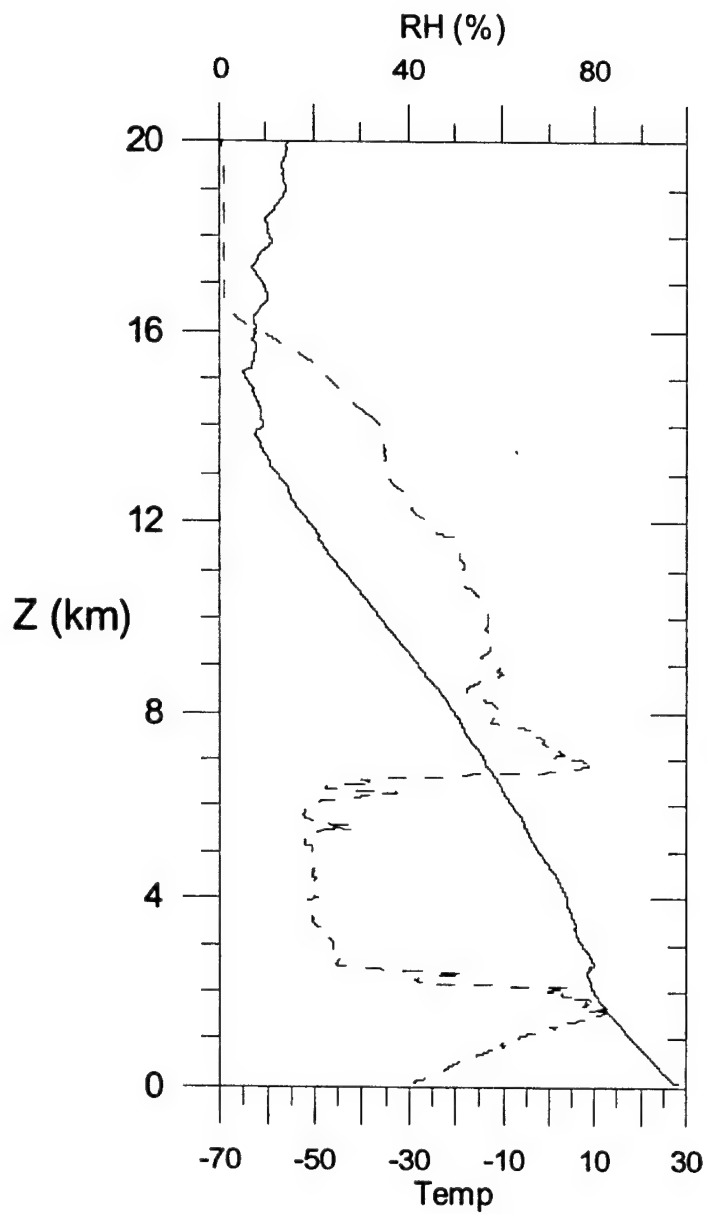


Figure 11. Radiosonde Temperature (C) and Relative Humidity (%) Vertical Profile: 16 August 19 GMT at Hanscom AFB, MA. On the right is the diagnosed area-averaged vertical velocity (cm s^{-1}) for 17 Aug 00Z

which are prevalent on this day but absent on the other two days. On 16 August, the tropopause height was ~ 13.8 km (Figure 11) and the cirrus altitudes varied from 9 km to 13.5 km (Figure 8). These figures illustrate qualitatively the variation in cirrus height and structure that occurred during the measurement period.

A weak qualitative correlation between the altitudes of maximum relative humidity, diagnosed vertical velocity, and altitudes of cirrus backscatter was observed. On 9 August, the vertical velocity peaked near 14 km, in the cirrus backscatter region, at ~ 0.7 cm/s, but the relative humidity was measured $< 40\%$ in the upper troposphere region. On 14 August, the correlation of both relative humidity and vertical velocity with cirrus backscatter was better. The vertical velocity peaked at > 10 cm/s near 10 km, and a relatively moist layer with peak relative humidity $\sim 70\%$, was observed from 9 km to 13 km. This corresponds closely to the $10.6 \mu\text{m}$ cirrus backscatter vertical extent. On 16 December, the relative humidity peaked at 80 % near 7 km while the vertical velocity showed a broad peak centered at 8 km with a maximum of 4 cm/s. These peaks were somewhat below the cirrus base altitudes of ~ 9 km and may have been associated with the lower altostratus or altocumulus (see Figure 8).

5. CALCULATION OF BACKSCATTER COEFFICIENT FROM SCATTERING THEORY

Using Eqs. (1) and (2), the theoretical volume backscatter coefficient can be calculated for a polydispersion of spheres. The backscattering amplitude $S_1(\pi)$ is calculated, using the expression described in van de Hulst (1957), as

$$-S_1(\pi) = S_2(\pi) = \sum_{n=1}^{\infty} \left(n + \frac{1}{2}\right) (-1)^n (a_n - b_n) \quad (5)$$

where a_n and b_n are scattering coefficients for spheres and are functions of sphere radius, electromagnetic wavelength, and the particle's complex refractive index. The scattering coefficients are calculated using Aden's (1951) algorithm employing spherical Bessel functions and Infeld's (1947) recursion formula for logarithmic derivatives. Upward recursion is used for spherical Bessel functions with real arguments while downward recursion is used for those functions with complex arguments (e.g. described by Kattawar and Plass, 1967). The wavelength-dependent refractive index for ice is determined from the tables of Warren (1984). Table II lists the complex refractive index for ice for the three lidar measurement wavelengths. A description of the calculation procedures for the spherical scattering coefficients a_n and b_n is provided in Appendix A.

Table 2. Refractive index for ice $m = m_r - i m_i$ $i = \sqrt{-1}$

Wavelength (μm)	m_r	m_i
10.6	1.1038	0.1246
1.064	1.3004	1.9×10^{-6}
0.532	1.3117	2.6×10^{-9}

Cirrus clouds are typically composed of non-spherical particles such as hollow columns, bullet rosettes, dendrites, hexagonal plates, capped columns, etc. Using ice spheres to approximate hexagonal ice crystals for their scattering and absorption properties can be inadequate and frequently misleading (Takano and Liou, 1995). In an attempt to address the non-spherical shape of cirrus particles, scattering calculations were also performed for very long ice cylinders where the length of the cylinders is significantly larger than the diameter. Here, the light on the cylinders is assumed to be of perpendicular incidence

from below and the cylinders are uniformly oriented in the horizontal plane such that the angle of obliquity $\alpha = 0$ (see Figure 2). Following van de Hulst (1957), the backscatter efficiency (per unit cylinder length) for light of perpendicular incidence on uniformly-oriented circular cylinders can be expressed as

$$\text{Case I } (E \parallel \text{axis}): \quad Q_{bsct} = \frac{4}{\pi x} |T_1(\pi)|^2 = \frac{4}{\pi x} i_1(\pi) \quad (\text{sr}^{-1}) \quad (6)$$

where the electric field E is parallel to the cylinder axis and

$$\text{Case 2 } (H \parallel \text{axis}): \quad Q_{bsct} = \frac{4}{\pi x} |T_2(\pi)|^2 = \frac{4}{\pi x} i_2(\pi) \quad (\text{sr}^{-1}) \quad (7)$$

where the magnetic field H is parallel to the cylinder axis. The scattering angle $\theta = \pi$, and T_1 and T_2 are the amplitudes of scattered light vibrating parallel and perpendicular to the electric field vector, respectively. The total backscatter efficiency for incident light is the average of Eqs. (6) and (7) (see van de Hulst, 1957) or

$$Q_{bsct} = 0.5 \left(\frac{4}{\pi x} i_1(\pi) + \frac{4}{\pi x} i_2(\pi) \right) = \frac{2}{\pi x} (i_1(\pi) + i_2(\pi)) \quad (\text{sr}^{-1}) \quad (8)$$

Here,

$$T_1(\theta) = b_0 + 2 \sum_{n=1}^{\infty} b_n \cos n\theta \quad (9)$$

and

$$T_2(\theta) = a_0 + 2 \sum_{n=1}^{\infty} a_n \cos n\theta \quad (10)$$

where a_n and b_n are the cylindrical scattering coefficients and are a function of cylinder radius, incident wavelength, and the scatterer's complex refractive index. Their solution is expressed in terms of the Bessel functions of integer order (e.g., Kerker, 1969) where forward and backward recursion techniques can be employed using Infeld's (1947) logarithmic recursion relation. A full description of calculation procedures for the scattering coefficients for a long cylinder is contained in Appendix B.

Analogous to Eq. (2), for a polydispersion of long, finite length circular ice cylinders with variable radius r , the backscatter coefficient, per unit cylinder length l , becomes

$$\frac{\beta_{\pi}}{l} = \int_0^{\infty} Q_{bsc} n(r) r dr \quad (\text{m}^{-2} \text{ sr}^{-1}) \quad (11)$$

In the evaluation of Eqs. (2) and (11), a modified gamma particle size distribution (Intrieri et al, 1993) is used to represent the cirrus cloud polydispersion and is of the form:

$$n(r) = \frac{N_o}{\Gamma(p)r_m} \left(\frac{r}{r_m} \right)^{p-1} \exp\left(-\frac{r}{r_m}\right) \quad (\# \text{ m}^{-3} \mu\text{m}^{-1}) \quad (12)$$

where N_o is the number density, Γ is the gamma function, p is an integral dispersion factor and r_m is the characteristic radius of the distribution. The characteristic radius r_m of the size distribution is related to the equivalent radius r_e by $r_e = (p+2)r_m$. For the measurement comparisons with theory, $p = 2$. An example plot of the modified gamma size distribution $n(r)$ normalized by N_o is depicted in Figure 12. Equation (2) is integrated over the particle radius size range of $\sim 0.01 \mu\text{m}$ to 6 mm for spheres and Eq. (11) is integrated over the cylinder radius size range of $0.01 \mu\text{m}$ to 2 mm . The relation between these ranges of particle size radius r and size parameter x as a function of wavelength is listed in Table 3 since the integrals involving scattering efficiencies are typically evaluated in terms of x .

Table 3. Numerical integration limits for size parameter x as a function of wavelength and particle type $x = 2\pi r/\lambda$

Wavelength (μm)	Spheres (x_{\min}, x_{\max})	Long Cylinders (x_{\min}, x_{\max})
10.6	0.006, 3557	0.006, 1200
1.064	0.059, 35431	0.059, 11810
0.532	0.118, 70863	0.118, 23620

In the backscatter and extinction ratio comparisons to be discussed subsequently, the number density N_o , which is a constant in Eq. (12), will cancel out. The number density N_o can also be estimated from the expressions defining backscatter and extinction coefficients for a polydispersion.

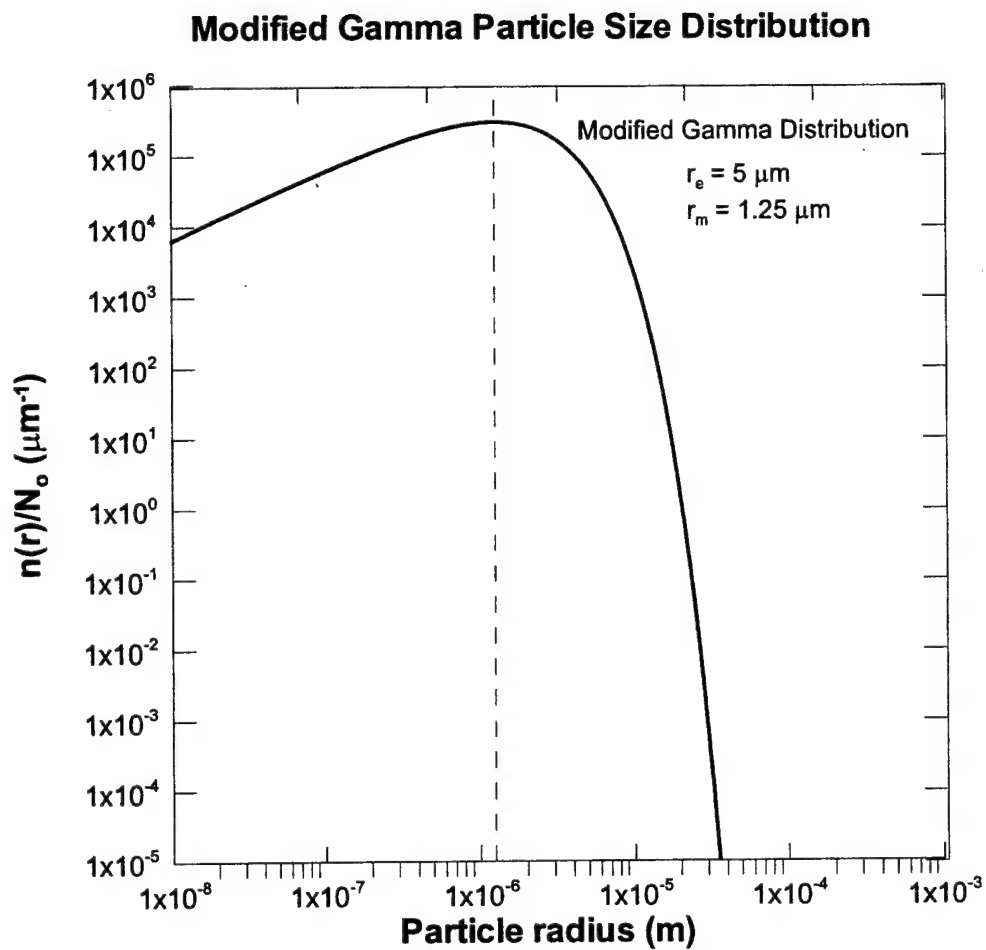


Figure 12. Normalized Modified Gamma Particle Size Distribution Calculated from Eq. (12) Used to Represent the Cirrus Cloud. Here the equivalent radius $r_e = 5 \mu\text{m}$ and the integral dispersion factor $p = 2$

6. COMPARISON OF MEASURED AND CALCULATED LIDAR CIRRUS BACKSCATTER RATIOS

Intrieri et al (1993) compared measured and theoretical calculations of backscatter coefficient ratios for lidar and radar to infer the effective particle size of cirrus. A similar approach is attempted here using lidar volume backscatter coefficient ratios for the three days of measurement: 9 August, 14 August, and 16 August.

The backscatter ratio γ_π for two lidar wavelengths given simultaneous measurements at a particular altitude z and time t is defined as:

$$\gamma_\pi = \frac{\beta_\pi(\lambda_1)}{\beta_\pi(\lambda_2)} \quad (13)$$

where λ_1 and λ_2 are the two lidar wavelengths.

For this approach, vertical profiles of measured lidar backscatter at each of the three wavelengths are interpolated to equal altitude levels separated by 100 m. The interpolated data are then smoothed using a Gaussian probability distribution with a standard deviation of 400 m. Except for possible missing data, backscatter measurements from the Nd:YAG lidar at 1.064 μm and 0.532 μm are considered simultaneous in time and altitude location. If the 10.6 μm (CO_2) and 0.532/1.064 μm (Nd:YAG) lidar wavelengths' backscatter measurements are within 16 seconds of each other and the interpolated height levels are equivalent, then the backscatter ratio γ_π (Eq. (13)) is evaluated at that altitude z and time t .

Measured and theoretical backscatter ratios are calculated for two different wavelength pairs: 10.591 μm /0.532 μm and 1.064 μm /0.532 μm . Lidar backscatter measurements are used from three days in the calculations: 9 Aug 2001, 14 Aug 2001, and 16 Aug 2001.

Time vs. height cross-sections of measured $\log_{10} \beta_{\pi} (\text{m}^{-1} \text{sr}^{-1})$ are shown in Figures 13 through 15 for 0.532 μm , 10.6 μm , and 1.064 μm , respectively. These may be useful in certain applications by providing some representative or characteristic time and altitude variation of cirrus backscatter magnitudes at visible and infrared wavelengths. Figure 13 displays contours of the logarithm (base 10) of the measured volume backscatter coefficient β_{π} at 0.532 μm plotted as a function of time and altitude for 9 August 2001 for altitudes above 10 km. At 0.532 μm , $\log_{10}(\beta_{\pi})$ magnitudes range from ~ -4.5 to almost -6.0 . Figure 14 is the same type of analysis as Figure 13 but for $\log_{10} \beta_{\pi}$ at 10.6 μm . For this wavelength, the range of magnitudes runs from ~ -6.5 to -8.5 . For 1.06 μm (Figure 15) on 9 August, the range of measured $\log_{10}(\beta_{\pi})$ is -5.0 to -6.0 .

Figure 16 shows contours of the measured backscatter ratio γ_{π} for 10.6 μm and 0.532 μm corresponding to the cloud backscatter plots of Figures 13 and 14. The measured γ_{π} ratios range from about 0.003 to 0.01. These can be compared with the theoretical ratio calculations plotted in Figure 17 using Eqs. (2) and (13) over a range of equivalent ice sphere radii r_e from 0.1 μm to 350 μm . This comparison shows that for particle sizes exceeding $\sim 0.6 \mu\text{m}$, the calculation for backscatter ratio (10.6/0.532) using scattering theory for spheres lies within the bounds of the measured backscatter ratio (10.6/0.532) from cirrus on 9 August.

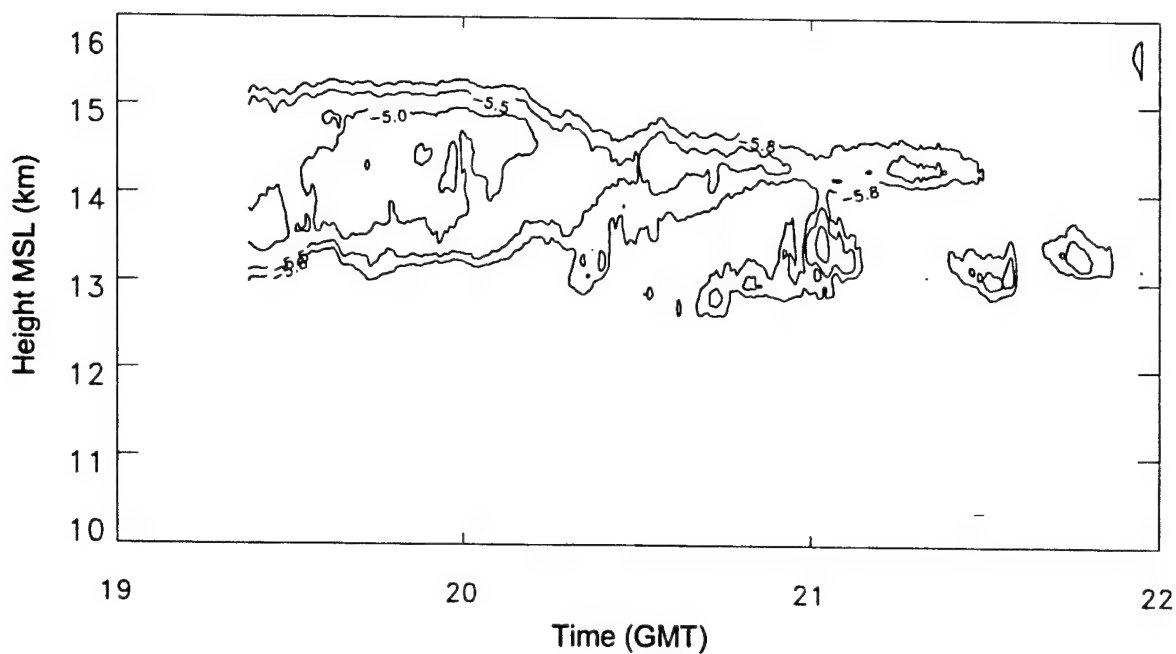


Figure 13. Contour Intervals of -5.8, -5.5, -5.0, and -4.5 ($\text{m}^{-1} \text{sr}^{-1}$) on a Plot of $\log_{10}(\beta_{\pi})$ at $0.532 \mu\text{m}$ for 9 August 2001

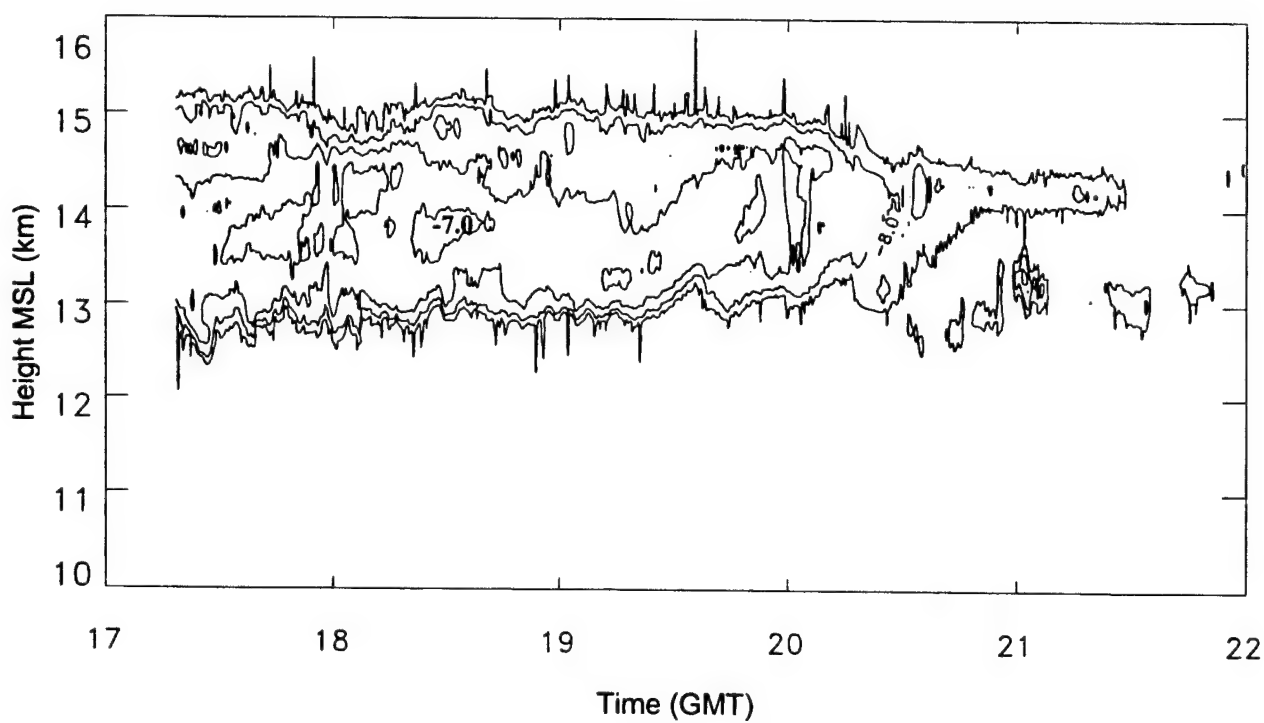


Figure 14. Contour Intervals of -8.5, -8.0, -7.5, -7.0, and -6.5 on a Plot of $\log_{10}(\beta_{\pi})$ at $10.6 \mu\text{m}$ for 9 August 2001

The same technique is also used for determining γ_π for 1.064 μm and 0.532 μm backscatter. Corresponding to the $\log_{10}(\beta_\pi)$ contours plotted in Figure 15, the measured backscatter ratio γ_π (1.064/0.532) is plotted in Figure 18 as a function of time and altitude. The measured (1.064/0.532) backscatter ratio range for 9 August is approximately 0.5 to 1.30. The theoretical calculation of γ_π as a function of equivalent radius r_e for ice spheres is plotted in Figure 19 along with the range of measured γ_π . Except for the region between 20 μm and 100 μm , the measured range of the ratio γ_π encloses the theoretical values for equivalent particle sizes exceeding $\sim 2.0 \mu\text{m}$. However, for either case, γ_π (10.6/0.532) or γ_π (1.064/0.532), little information can be gleaned concerning a preferred equivalent or mode cirrus particle size by comparing the measured range of values and the theoretical calculations over the range of equivalent ice particle radii.

To better understand the representativeness of these results, the measured backscatter ratio calculations are repeated for two more cirrus measurement days, 14 and 16 August. The $\log_{10} \beta_\pi$ contour analyses for 14 August are shown in Figures 20 through 22 for the three wavelengths. As seen from these figures and Figure 7, the cirrus altitudes on these days run from $\sim 9.5 - 12 \text{ km}$ with the principal cirrus layer centered near 10 km. The range of $\log_{10}(\beta_\pi)$ magnitudes at 10.6 μm was comparable to those measured on 9 August, $-8.5 \text{ m}^{-1} \text{ sr}^{-1}$ to $-6.5 \text{ m}^{-1} \text{ sr}^{-1}$, but cloud center values of $\log_{10}(\beta_\pi)$ were slightly lower for $\lambda = 0.532 \mu\text{m}$ and $\lambda = 1.06 \mu\text{m}$, with maximum values of -5.0 and -5.5 observed, respectively. The typical measured γ_π ratio range for (10.6/0.532) for 14 August was 1×10^{-3} to 5×10^{-2} according to Figure 23. This encompassed a lower particle size limit for the theoretical calculation of $\sim r_e = 0.5 \mu\text{m}$ but exceeds by a factor of 5 the maximum value of calculated γ_π as depicted in Figure 17. On 14 August, the range of measured backscatter ratio γ_π (1.064/0.532) at cirrus altitudes is about 0.1 to 0.5, according to Figure 24. This encompasses only those particles whose equivalent radius is less than $\sim 2.0 \mu\text{m}$ according to Figure 19.

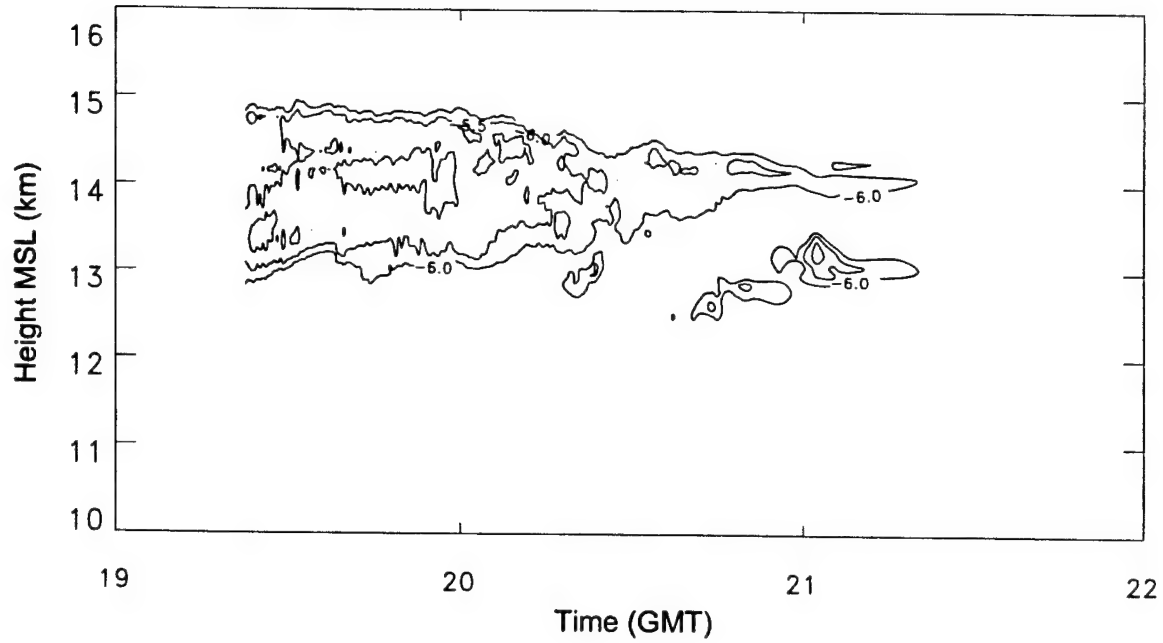


Figure 15: Contour Intervals of -6.0, -5.5, and -5.0 ($\text{m}^{-1} \text{sr}^{-1}$) on a Plot of $\log_{10}(\beta_{\pi})$ at $1.064 \mu\text{m}$ for 9 August 2001

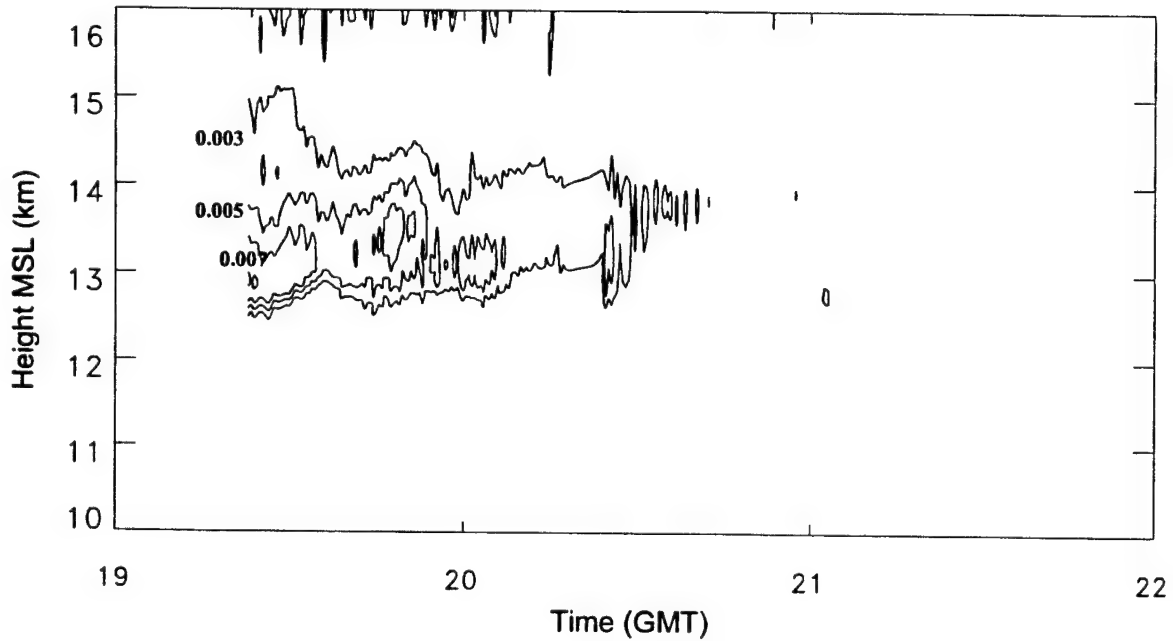


Figure 16. Contour Intervals of 0.003, 0.005, 0.007, and 0.01 on a Plot of Measured $\gamma_{\pi}(10.6\mu\text{m}/0.532\mu\text{m})$ for 9 August 2001

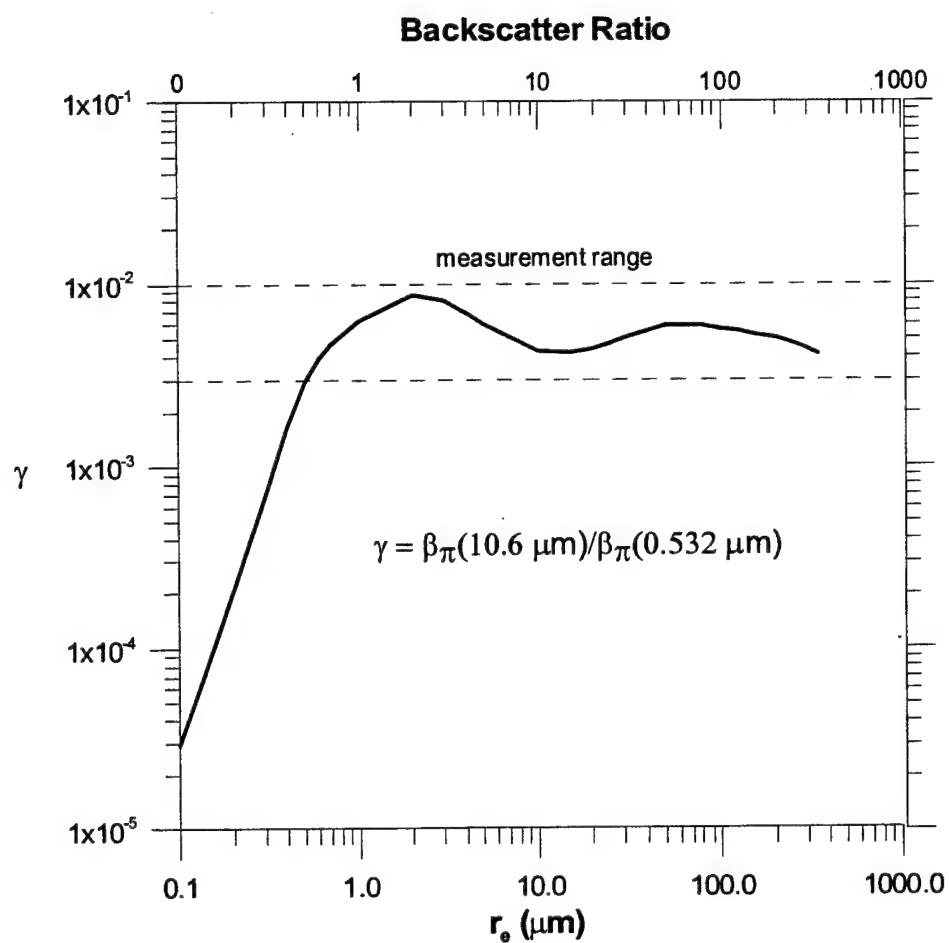


Figure 17. Backscatter Coefficient Ratio γ_{π} for Ice Spheres as a Function of Equivalent Radius for $\lambda=10.6 \mu\text{m}$, $0.532 \mu\text{m}$. Dashed lines represent range of measured γ_{π} in cirrus for 9 August.

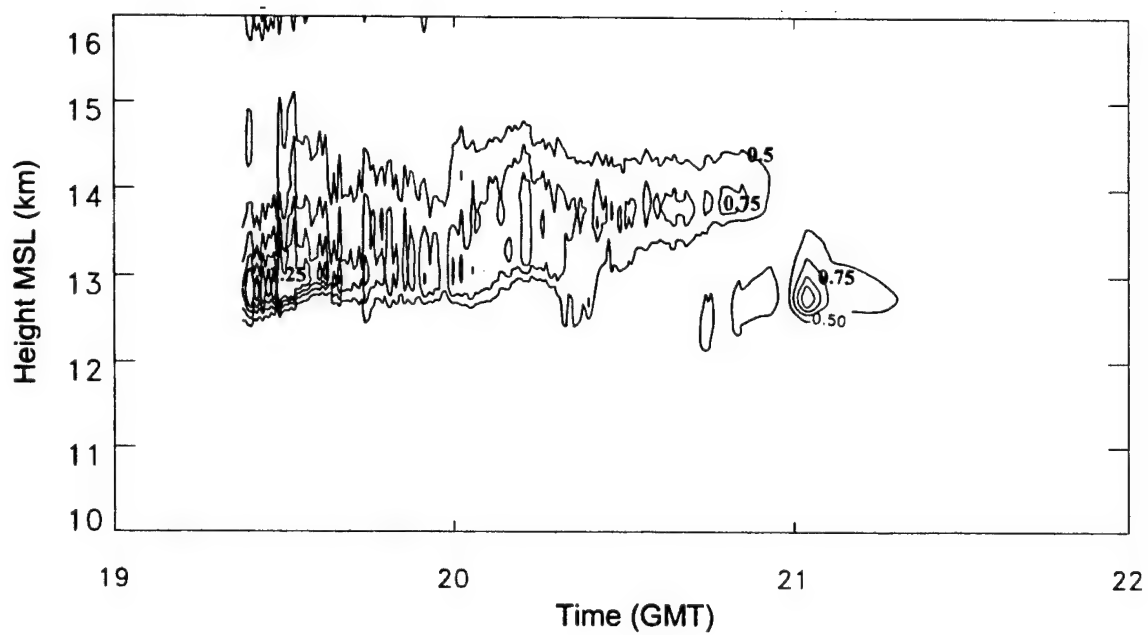


Figure 18. Measured $\gamma_{\pi}(1.064/0.532)$ for 9 August : Contour Interval: 0.5, 0.75, 1.0, 1.25

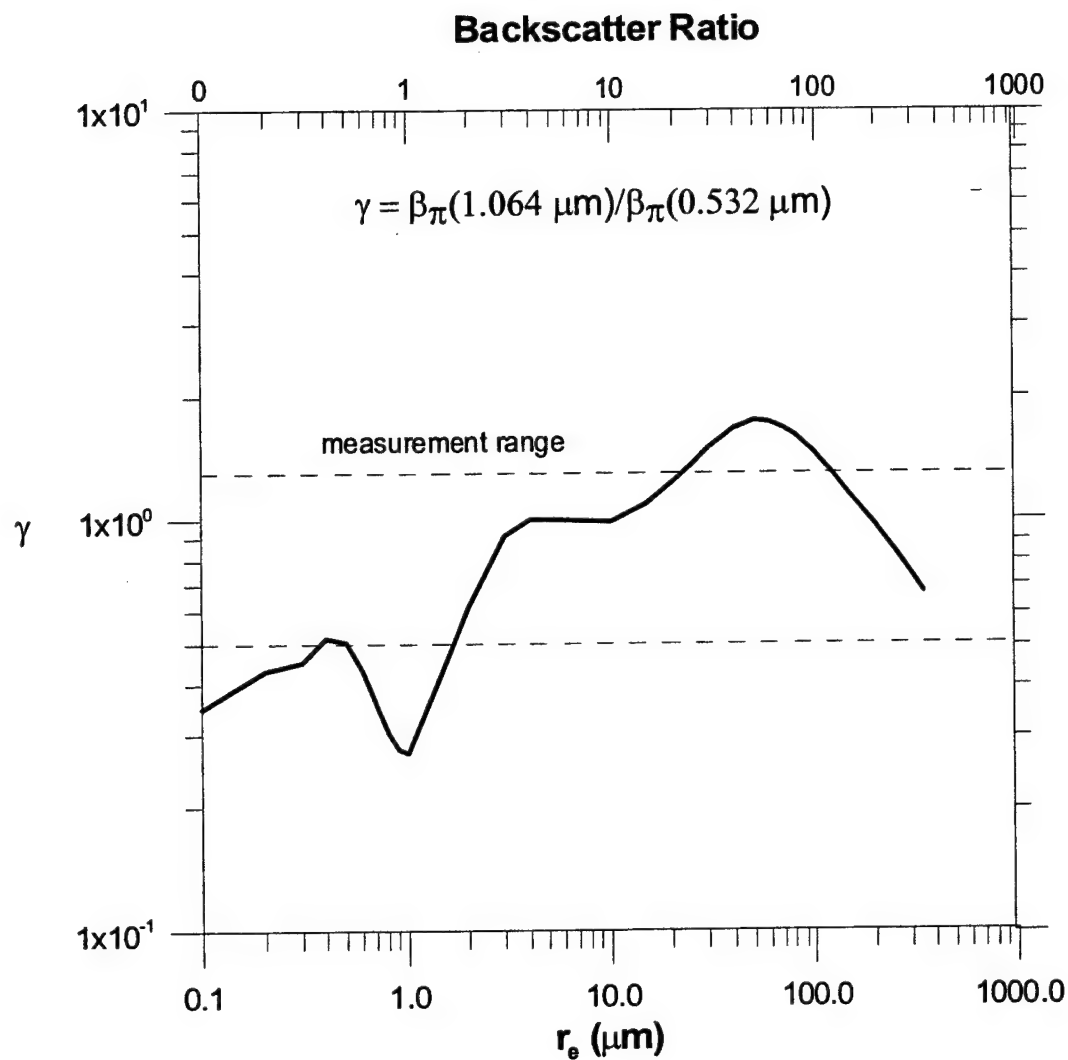


Figure 19. Backscatter Ratio γ_{π} for Ice Spheres as Function of Equivalent Radius for $\lambda=1.064 \mu\text{m}$, $0.532 \mu\text{m}$. Dashed lines represent range of measured γ_{π} values in cirrus for 9 August 2001

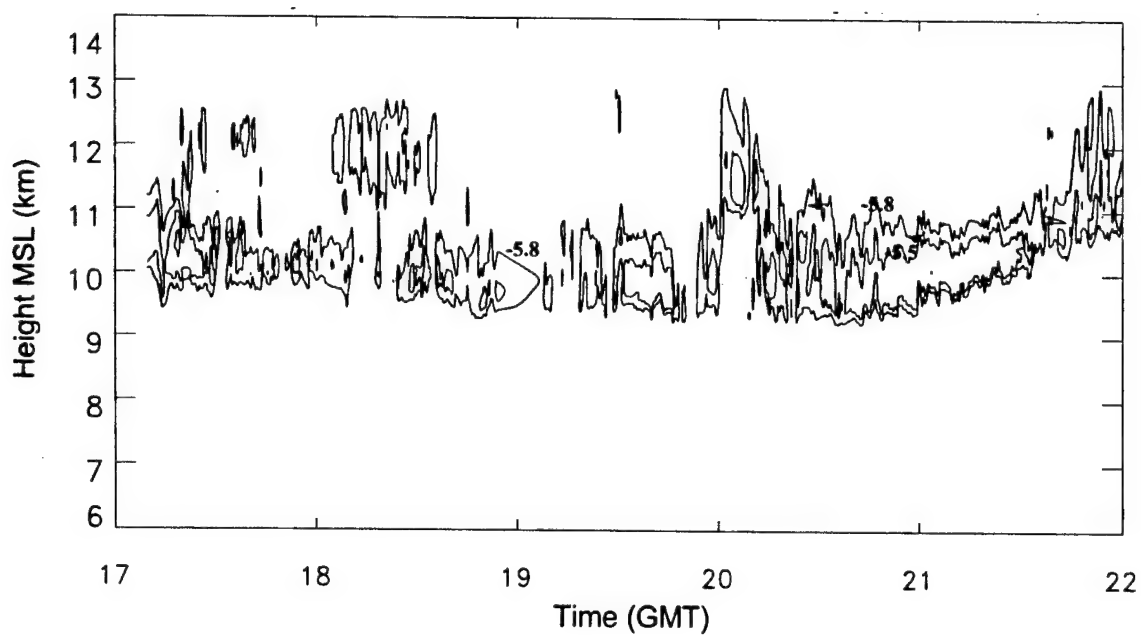


Figure 20. Contour Intervals of -5.8, -5.5, -5.0, and -4.5 ($\text{m}^{-1} \text{sr}^{-1}$) on a Plot of $\log_{10}(\beta_{\pi})$ at $\lambda = 0.532 \mu\text{m}$ for 14 August 2001:

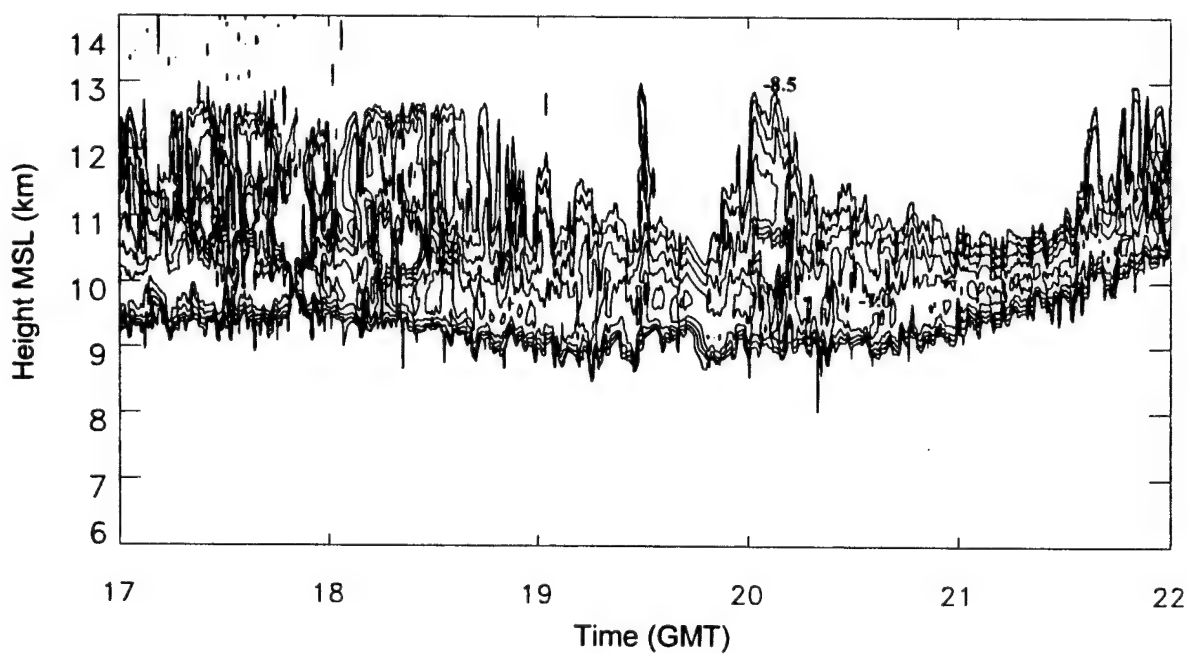


Figure 21. Contour Intervals of -8.5, -8.0, -7.5, -7.0, and -6.5 ($\text{m}^{-1} \text{sr}^{-1}$) on a Plot of $\log_{10}(\beta_{\pi})$ at $10.6 \mu\text{m}$ for 14 August

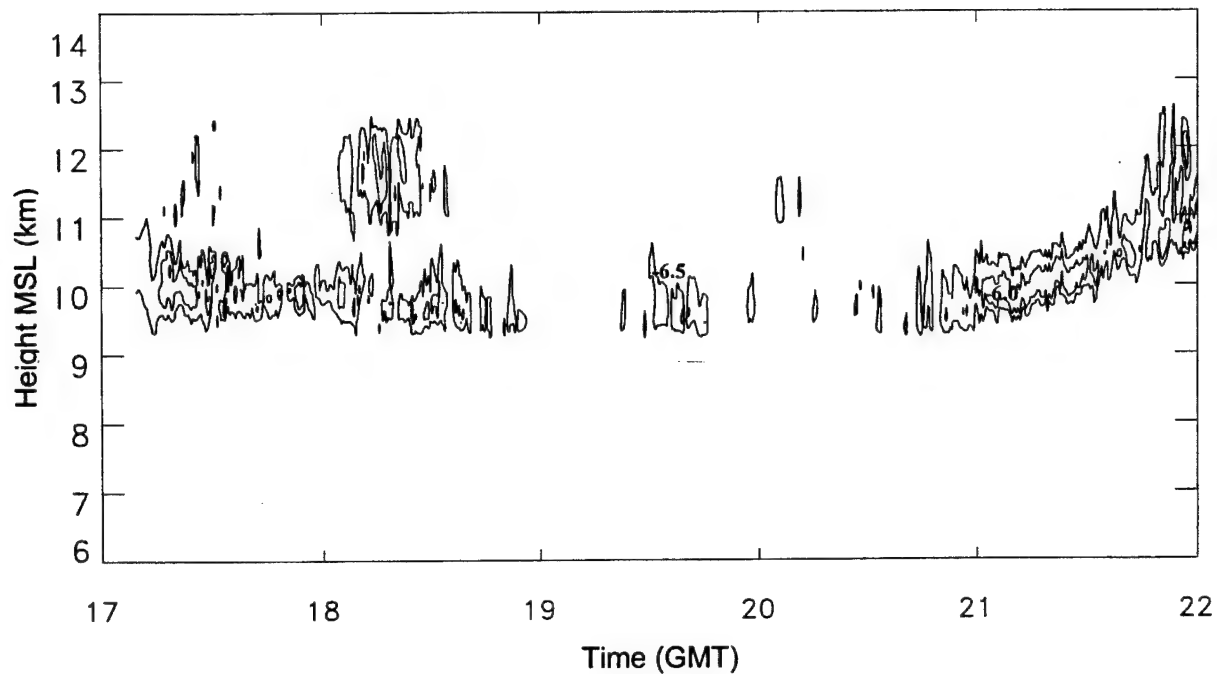


Figure 22. Contour Intervals of -6.5, -6.0, -5.5, -5.0, and -4.5 ($\text{m}^{-1}\text{sr}^{-1}$) on a Plot of $\log_{10}(\beta_{\pi})$ at $\lambda = 1.06 \mu\text{m}$ for 14 August

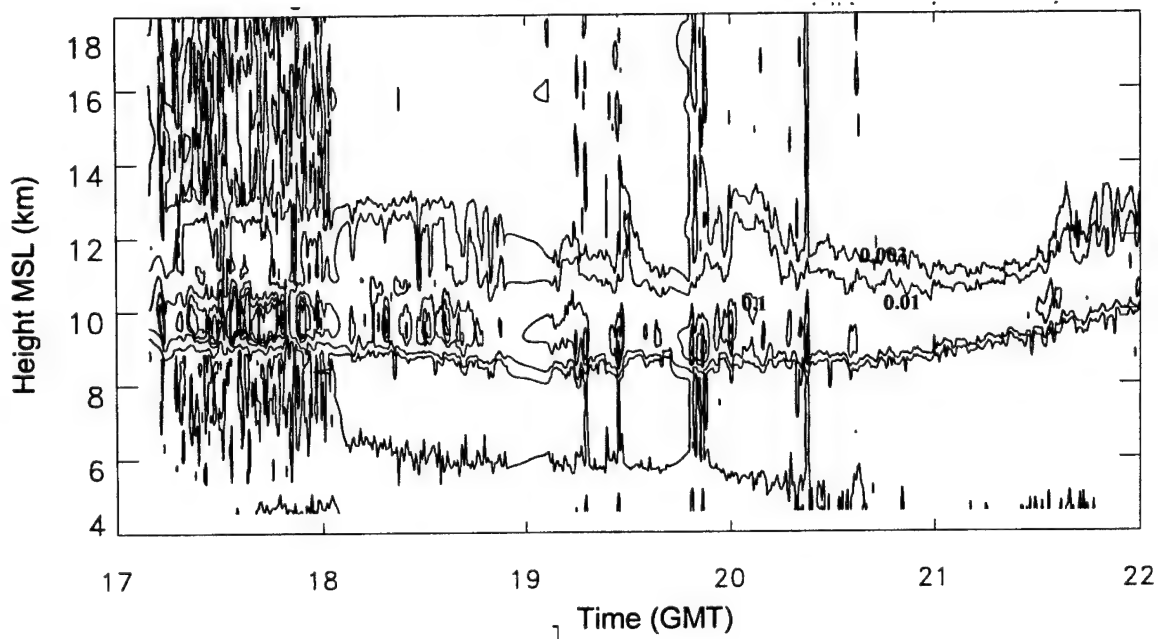


Figure 23. Contour Intervals of 0.003, 0.01, 0.1 and 0.3 on a Plot of $\gamma_{\pi}(10.6/0.532)$ for 14 August

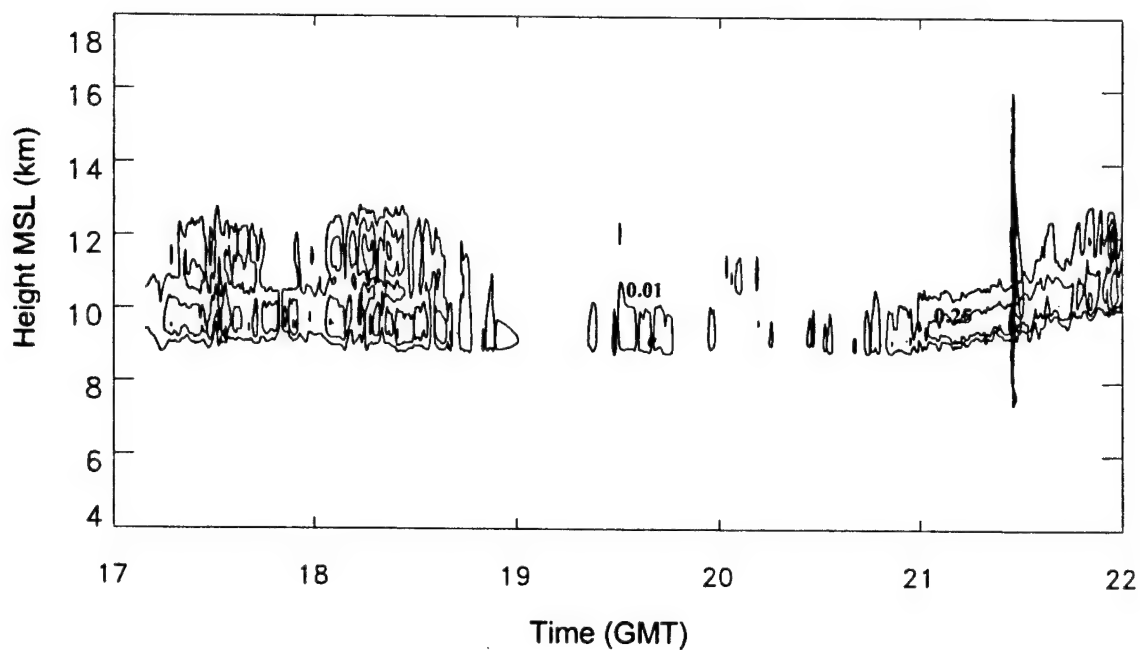


Figure 24. Contour Intervals of 0.01, 0.25, 0.5, and 1.0 on a Plot of $\gamma_{\pi}(1.064/0.532)$ for 14 August 2002:

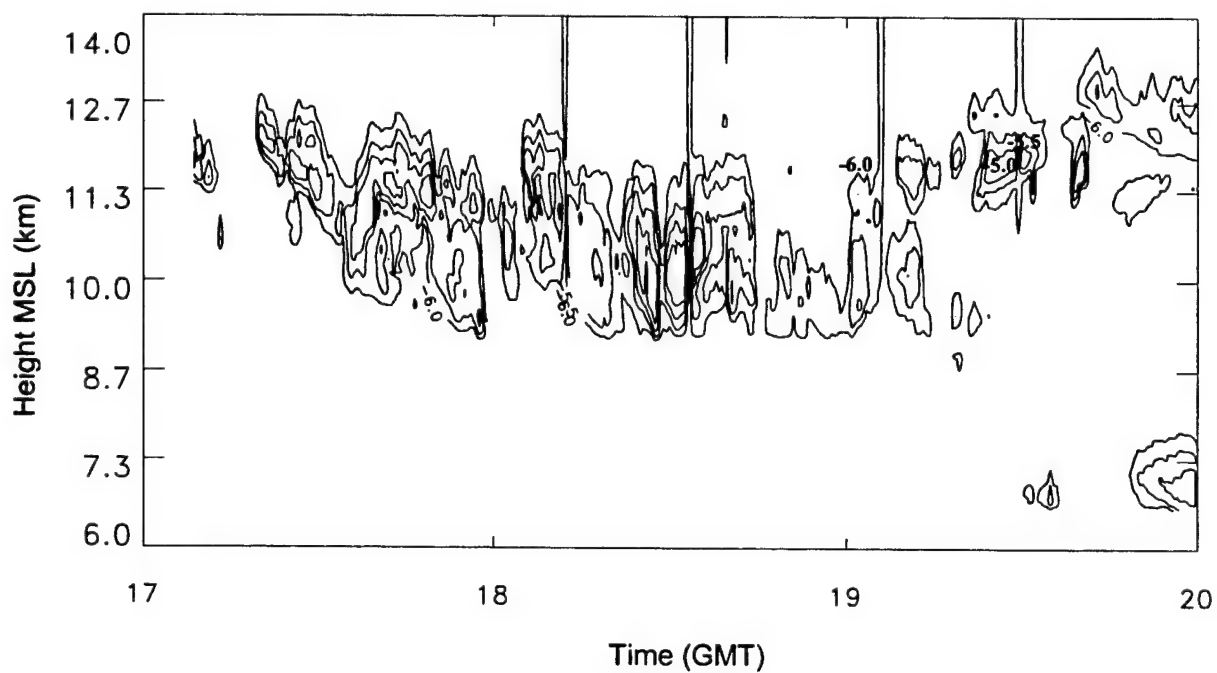


Figure 25. Contour Intervals of -6.0, -5.5, -5.0, and -4.5 on a Plot of $\log_{10}(\beta_{\pi})$ at $\lambda = 0.532 \mu\text{m}$ for 16 August 2001

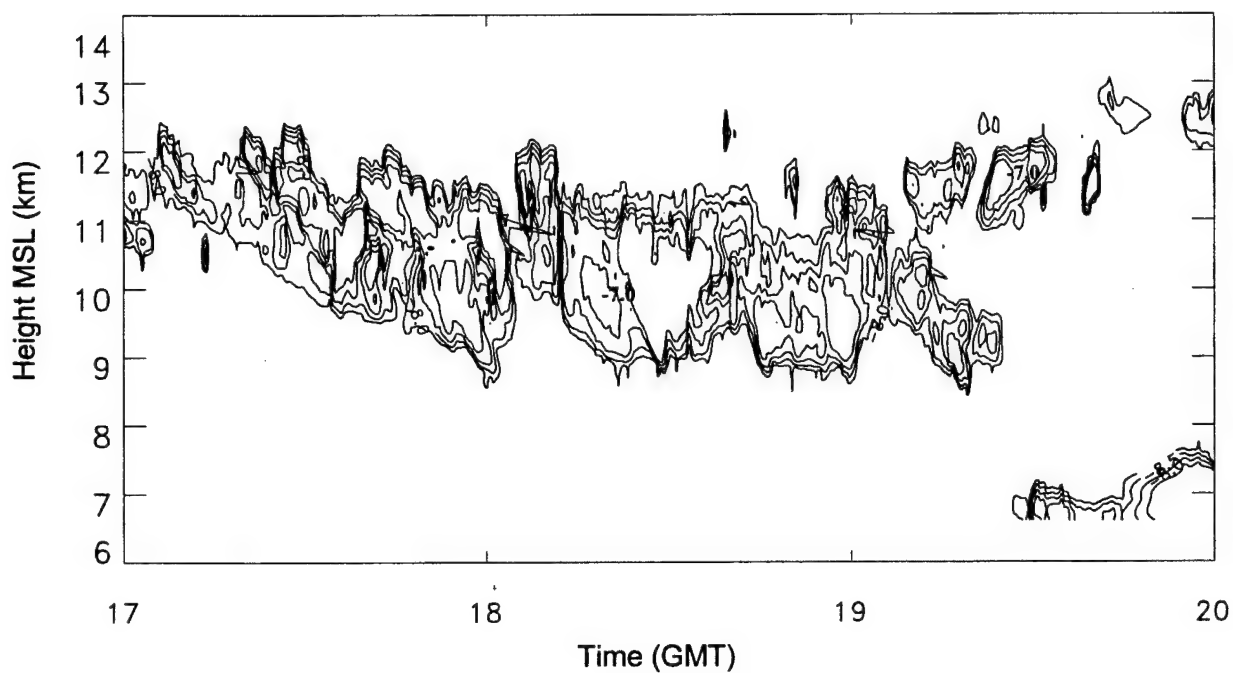


Figure 26. $\log_{10}(\beta_\pi)$ at $\lambda = 10.6 \mu\text{m}$ for 16 August 2001: Contour Interval: -8.5, -8.0, -7.5, -7.0 ($\text{m}^{-1} \text{sr}^{-1}$)

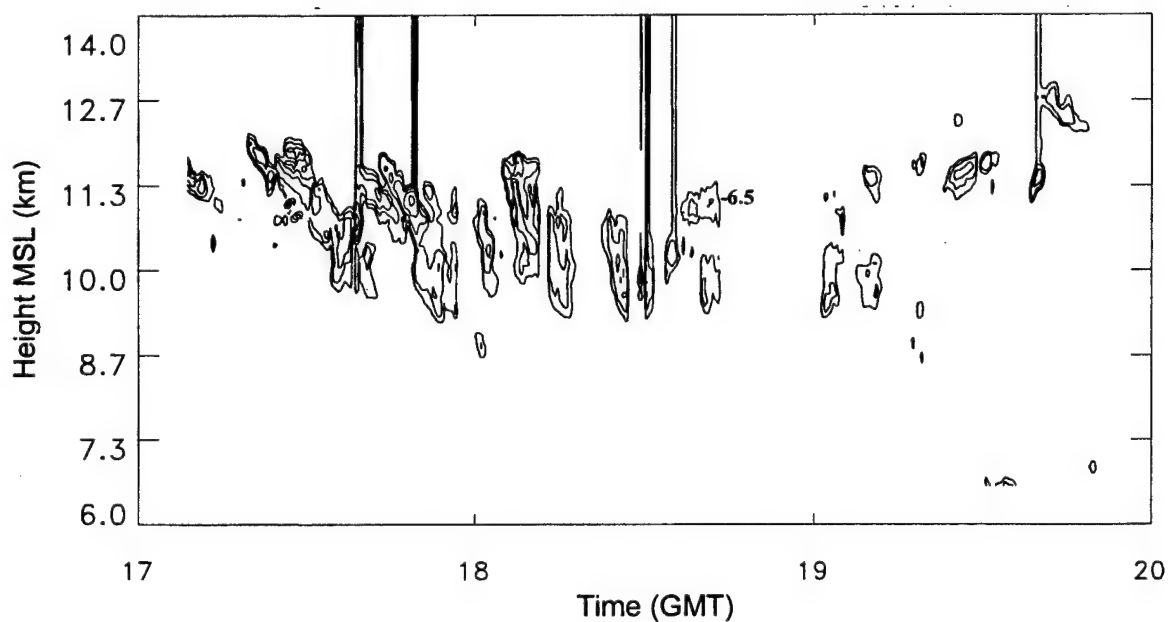


Figure 27. $\log_{10}(\beta_\pi)$ at $\lambda = 1.064 \mu\text{m}$ for 16 August 2001: Contour Intervals: -6.5, -6.0, -5.5, -5.0, -4.5

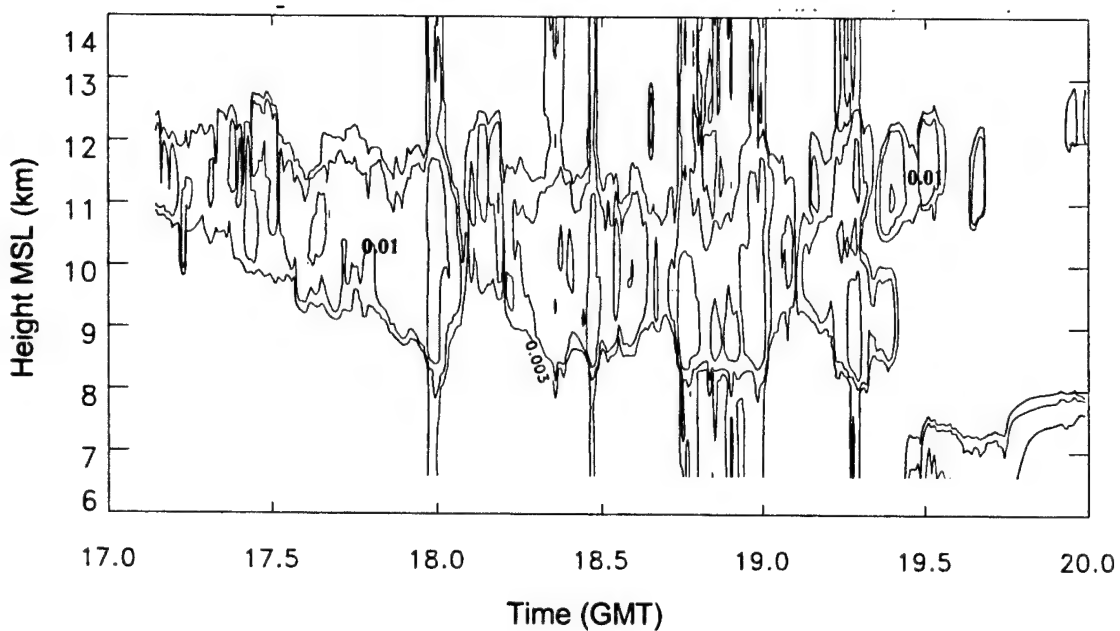


Figure 28. $\gamma_\pi(10.6/0.532)$ Analysis for 16 August 2001: Contour Interval 0.003, 0.01, 0.10

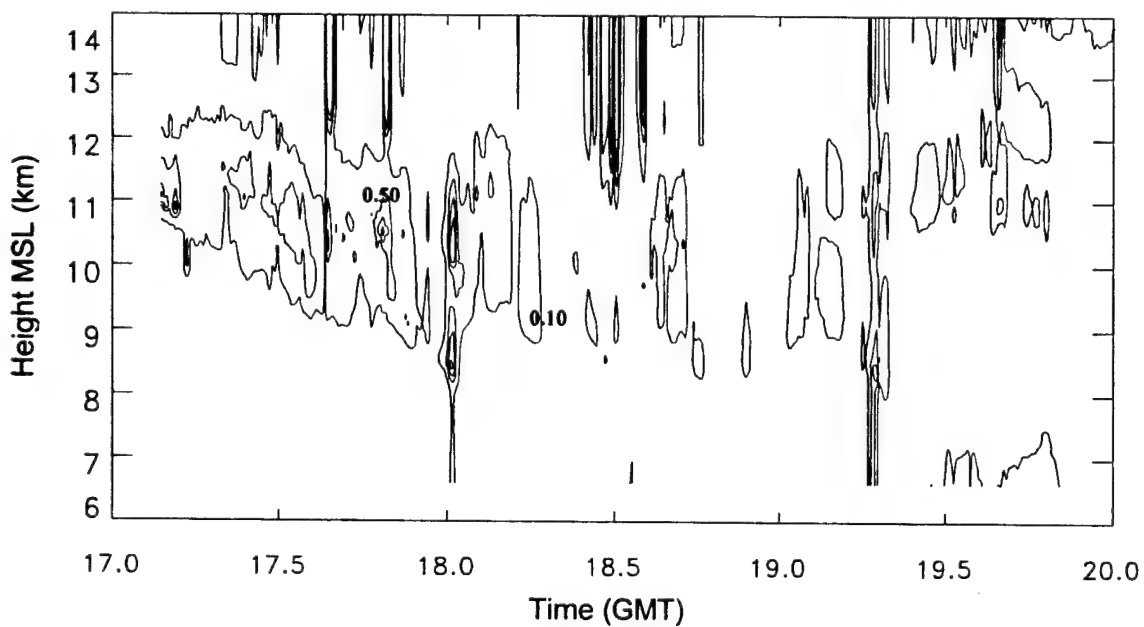


Figure 29. $\gamma_\pi(1.064/0.532)$ for 16 August 2001: Analysis for Contour Intervals: 0.1. 0.5. 1.0. 1.5

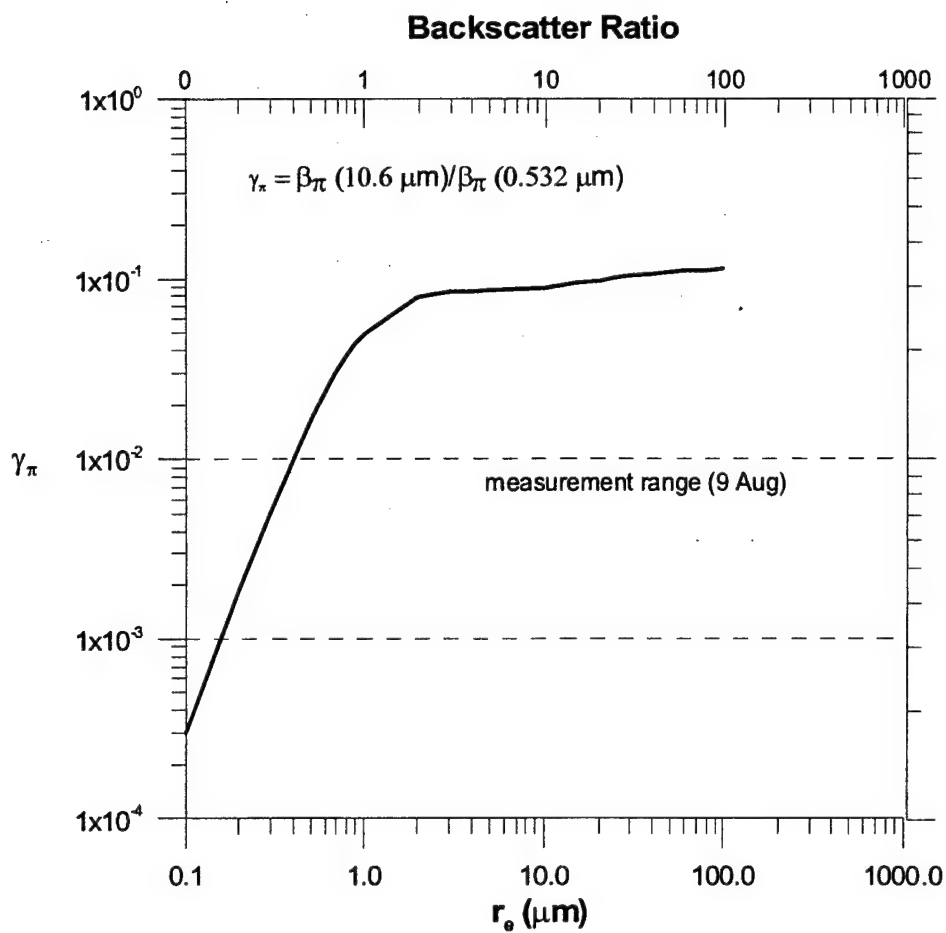


Figure 30. Backscatter Ratio γ_{π} for Long Perpendicularly-oriented Ice Cylinders as a Function of Cylinder Radius for $\lambda=10.6 \mu\text{m}$, $0.532 \mu\text{m}$

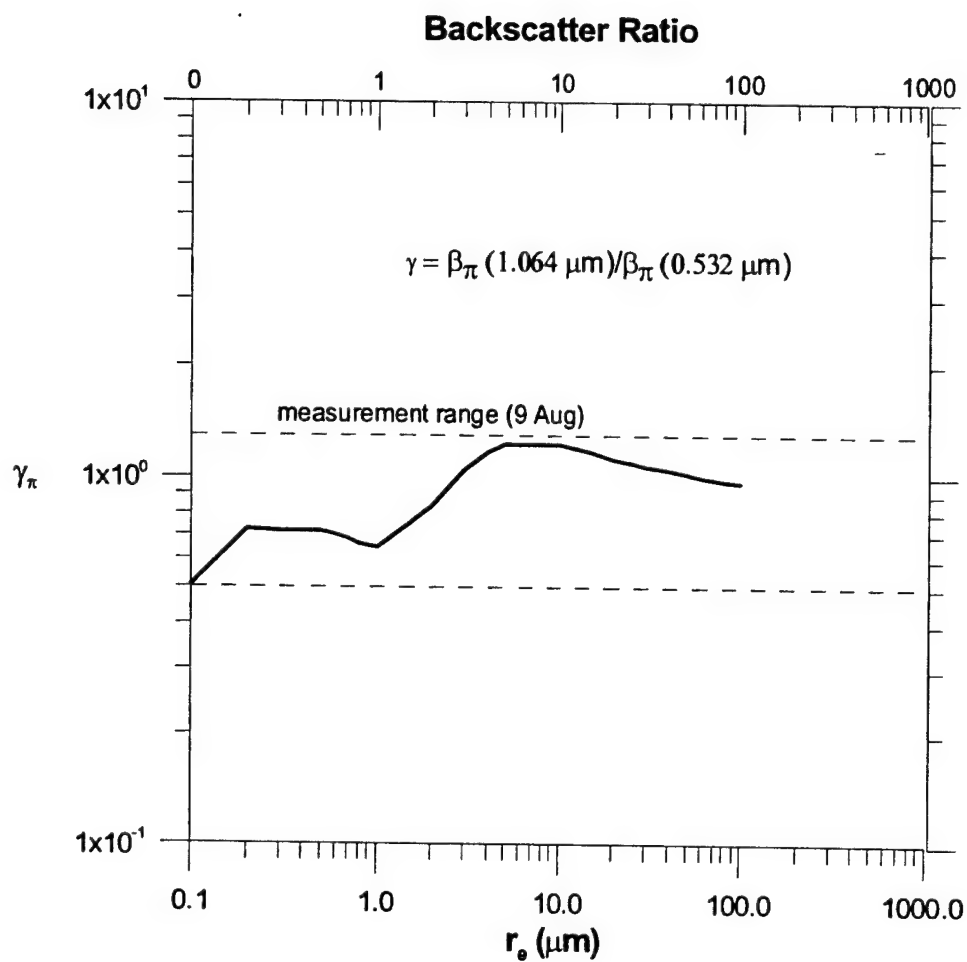


Figure 31. Backscatter Ratio γ_{π} for Long Perpendicularly-oriented Cylinders as a Function of Cylinder Diameter for $\lambda = 1.064 \mu\text{m}$, 0.532

For 16 August, the measured cirrus altitudes spanned the region from about 9 km to 12.5 km, encompassing a temperature range of -30°C to -60°C (see Figures 8 and 11). The measured $\log_{10}(\beta_{\pi})$ time vs. height contour plots at cirrus altitudes for each of the three wavelengths are depicted in Figures 25 through 27. $\log_{10}(\beta_{\pi})$ magnitudes ranged from -8.5 to $-6.5 \text{ m}^{-1} \text{ sr}^{-1}$ for $\lambda = 10.6 \text{ }\mu\text{m}$ and from -6.0 to $-4.5 \text{ m}^{-1} \text{ sr}^{-1}$ for $0.532 \text{ }\mu\text{m}$ with cloud center magnitudes exceeding $-7.0 \text{ m}^{-1} \text{ sr}^{-1}$ and $-4.5 \text{ m}^{-1} \text{ sr}^{-1}$ for $10.6 \text{ }\mu\text{m}$ and $0.532 \text{ }\mu\text{m}$, respectively. The range of measured lidar cirrus backscatter $\log_{10}(\beta_{\pi})$ for all three days is summarized by wavelength in Table 4.

Table 4. Measured Lidar Cirrus Backscatter Coefficient $\log_{10}(\beta_{\pi})$ Ranges for 9, 14 and 16 August 2001

Date	0.532 μm	1.06 μm	10.6 μm	Altitude Range	Temp. Range
9 Aug	-6.0 to -4.5	-6.0 to -5.0	-8.5 to -6.5	12.8 km – 15.3 km	-55C to -70 C
14 Aug	-6.0 to -5.0	-6.5 to -5.5	-8.5 to -6.5	9.0 km – 13.0 km	-30C to -60C
16 Aug	-6.0 to -4.5	-6.5 to -5.5	-8.5 to -6.5	9.0 km – 13.5 km	-30C to -60C

The measured $\gamma_{\pi}(10.6/0.532)$ in cirrus for 16 August ranged from 0.003 to 0.01 (Figure 28), encompassing the theoretical ratio curve for particle sizes exceeding $0.6 \text{ }\mu\text{m}$ (see Figure 17), except for near the center of the cirrus layer where values at times equal or exceeded 0.10. The measured $\gamma_{\pi}(1.064/0.532)$ ratio varied from 0.1 to ~ 1.0 before 18 GMT and stayed roughly within the 0.1 to 0.5 range after 18 GMT (Figure 29). The $\gamma_{\pi}(1.064/0.532)$ measurements before 18 GMT roughly enclose the γ_{π} ratios expected from theory in figure 19 but the measurements after 18 GMT are generally at the low end of the theoretical backscatter ratio values, indicative of particle sizes less than a couple of μm in radius.

The range of γ_{π} ratios calculated from lidar measurements and scattering theory for ice spheres ($1 \text{ }\mu\text{m} \leq r_e \leq 100 \text{ }\mu\text{m}$) are summarized in Table 5.

Table 5. Measured Lidar Cirrus Backscatter Coefficient Ratio Ranges for 9, 14 and 16 August 2001

Date	γ_{π} (10.6/0.532)	γ_{π} (1.06/0.532)	Altitude Range	Temp. Range
9 Aug	0.003 – 0.01	0.5 – 1.30	12.8 km – 15.3 km	-55C to -70 C
14 Aug	0.001 – 0.05	0.1 – 0.50	9.0 km – 13.0 km	-30C to -60C
16 Aug	0.003 – 0.10	0.1 – 1.00	9.0 km – 13.5 km	-30C to -60C
Theory	0.004 – 0.01	0.3 – 2.00		

It is also useful to compare the lidar-measured cirrus γ_{π} with the γ_{π} computed from theory for long ice cylinders or rods using Eq. (11). The theoretical γ_{π} ratios (10.6/0.532) and (1.064/0.532) for ice cylinders are plotted in Figures 30 and 31, respectively, along with the range of measured γ_{π} for the 9 August cirrus layers. The computed γ_{π} (10.6/0.532) for ice cylinders exceeds that for spheres by almost an order of magnitude over the range of equivalent radii while the computed γ_{π} (1.064/0.532) for ice cylinders exhibits magnitudes similar to that calculated from spheres. Thus, the measured range of γ_{π} (10.6/0.532) for 9 August only accounts for a relatively small size range of equivalent radii ($< 1.0 \mu\text{m}$) theoretically associated with long ice cylinders. However, the measured range of γ_{π} (1.064/0.532) encloses nearly the entire range of cylinder radii associated with calculated γ_{π} from $0.1 \mu\text{m}$ to 0.1 mm . Thus for either case, using spheres or cylinders, no significant information can be deduced concerning preferred particle size.

This last conclusion is also supported by the results contained in Appendix C which describe the normalized backscatter and extinction integration kernel (scattering efficiency per particle radius) behavior as a function of ice sphere radius for the three lidar wavelengths.

7. ESTIMATES OF ICE WATER CONTENT FROM CIRRUS BACKSCATTER

The bulk microphysical properties of cirrus can be characterized by particle number density N_0 or ice water content ρ_{iwc} . If the particle size distribution $n(r)$ is known for a polydispersion of ice spheres, the ice water content ρ_{iwc} can be computed as:

$$\rho_{iwc} = \frac{4\pi}{3} \rho_{ice} \int_0^{\infty} n(r) r^3 dr \quad (\text{kg m}^{-3}) \quad (14)$$

where ρ_{ice} is the density of ice (which is a weak function of temperature). Using Eqs. (2), (12), and (14), the measured backscatter β_{π} and, assuming an equivalent or modal sphere radius, ρ_{iwc} can be computed.

Analogously, for a polydispersion of ice cylinders, the ice water content is expressed as

$$\rho_{iwc} = \pi \rho_{ice} \int_0^{\infty} n(r) l r^2 dr \quad (\text{kg m}^{-3}) \quad (15)$$

where l is the cylinder length. Note that the inversion of Eq. (11) needed for equation (15), using Eq. (12), yields number density N_0 times cylinder length l , $N_0 \cdot l$ (m^{-2}), instead of number density N_0 (m^{-3}) as is the case with spheres (Eq. (2)).

Calculations of time series of ρ_{iwc} for a polydispersion of ice spheres for the lidar measurements on 9 August at 14 km altitude, 14 August at 10 km altitude, and 16 August at 10 km altitude are shown in Figures 32 through 34. Results are displayed assuming equivalent radii of 10 μm and 100 μm . The particular altitudes selected represent the location near where maximum β_{π} was measured in the lower half of the cirrus altitude regions. For 9 August, using the measured backscatter at 14 km altitude and temperature of -65°C , the time series of calculated ice water contents show relatively good agreement between wavelengths for ice water content magnitudes exceeding $1 \times 10^{-3} \text{ g m}^{-3}$. Typical ice water content values calculated ranged between 1×10^{-3} and $5 \times 10^{-2} \text{ g m}^{-3}$ for $r_e = 100 \mu\text{m}$ and between 2×10^{-4} to $3 \times 10^{-3} \text{ g m}^{-3}$ for $r_e = 10 \mu\text{m}$. The calculations are compared with other values listed in the literature. Heymsfield (1977) reported ice water content values for cirrus at a temperature of -50°C ranging from $\sim 3 \times 10^{-4} \text{ g m}^{-3}$ to $8 \times 10^{-3} \text{ g m}^{-3}$ using particle size spectra measurements from *in-situ* particle measurement

probes. Heymsfield (1994) reported a mean ice water content of $3.9 \times 10^{-3} \text{ g m}^{-3}$ for tropical cirrus *in-situ* measurements made near Kwajalein with temperatures between -60°C and -70°C . This value is plotted as a dashed line on Figure 32.

Time series calculations of ice water content are plotted in Figures 33 and 34 using the backscatter measurements at 10 km altitude on 14 August and 16 August, respectively, for all three wavelengths. On both days, the air temperature at 10 km was approximately -35°C . Heymsfield (1994) listed ice water contents computed from *in-situ* particle size probe measurements in cirrus as a function of temperature made during the FIRE campaign and averaged over a 1 km interval. For temperatures near -35°C , measured ice water contents for cirrus not associated with deep synoptic-scale systems averaged $8.6 \times 10^{-3} \text{ g m}^{-3}$ with a median value of $\sim 1 \times 10^{-2} \text{ g m}^{-3}$. This mean value is plotted as a dashed line on the figures. ρ_{iwc} calculations for 14 August show these magnitudes regularly being achieved only for the β_π measurements at $10.6 \mu\text{m}$ assuming $r_e = 100 \mu\text{m}$, and are not achieved using β_π measurements at $1.06 \mu\text{m}$. For 16 August, the mean *in-situ* ice water content magnitudes are achieved routinely for measurements at $10.6 \mu\text{m}$ and more frequently for β_π measurements at $0.532 \mu\text{m}$, again assuming an equivalent radius of $100 \mu\text{m}$. In no instance, for either 14 or 16 August, are ρ_{iwc} magnitudes of $1 \times 10^{-2} \text{ g m}^{-3}$ achieved for β_π measurements at $1.06 \mu\text{m}$. It should be noted that the backscatter signal at $0.532 \mu\text{m}$ is self-calibrated against the Rayleigh component. While the same technique of calibration is also applied to the $1.06 \mu\text{m}$ signal, a weaker Rayleigh component typically introduces a higher uncertainty.

Calculations of ice water content were also accomplished for the scattering efficiencies of long circular cylinders on 9 August at 14 km altitude for the three wavelengths and are plotted in Figure 35. The ratios of ice water content for spheres (*iwc*) and ice water

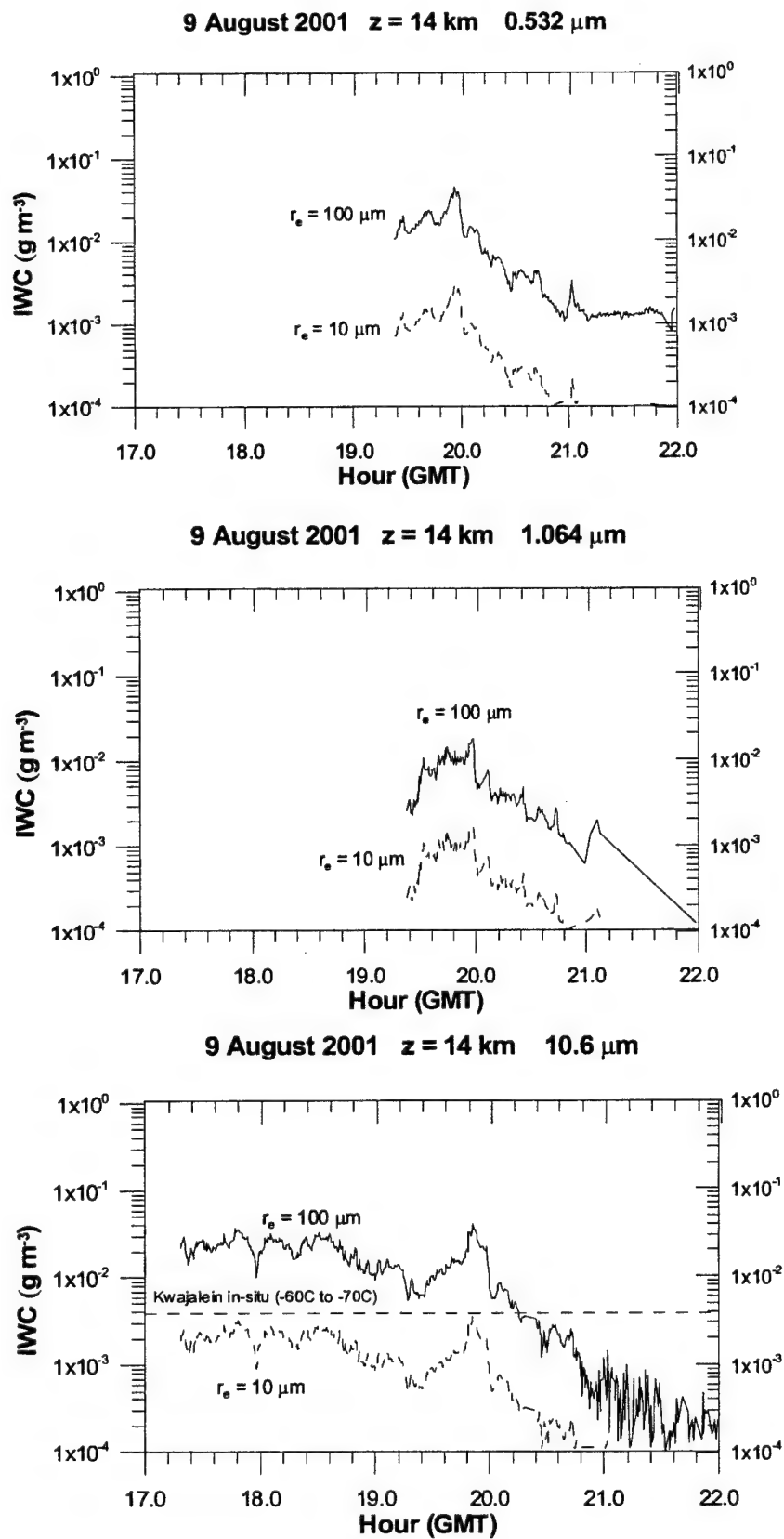


Figure 32. Ice Water Content (iwc) Calculations for 9 Aug Using Backscatter Measurements and Assuming a Modified Gamma Polydispersion of Ice Spheres

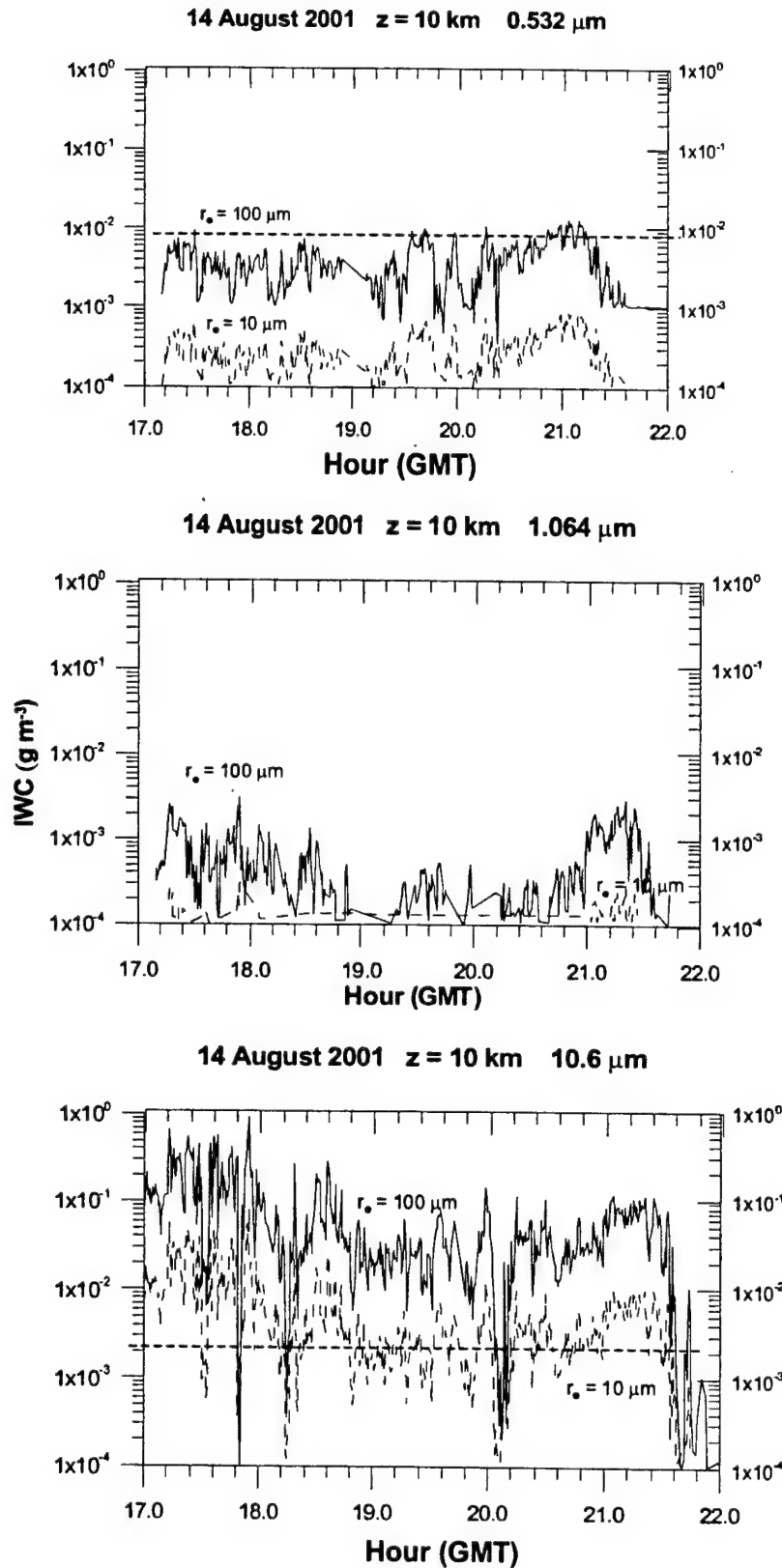


Figure 33. Ice Water Content (g m^{-3}) calculations for 14 Aug Using Backscatter Measurements and Assuming a Modified Gamma Polydispersion of Ice Spheres

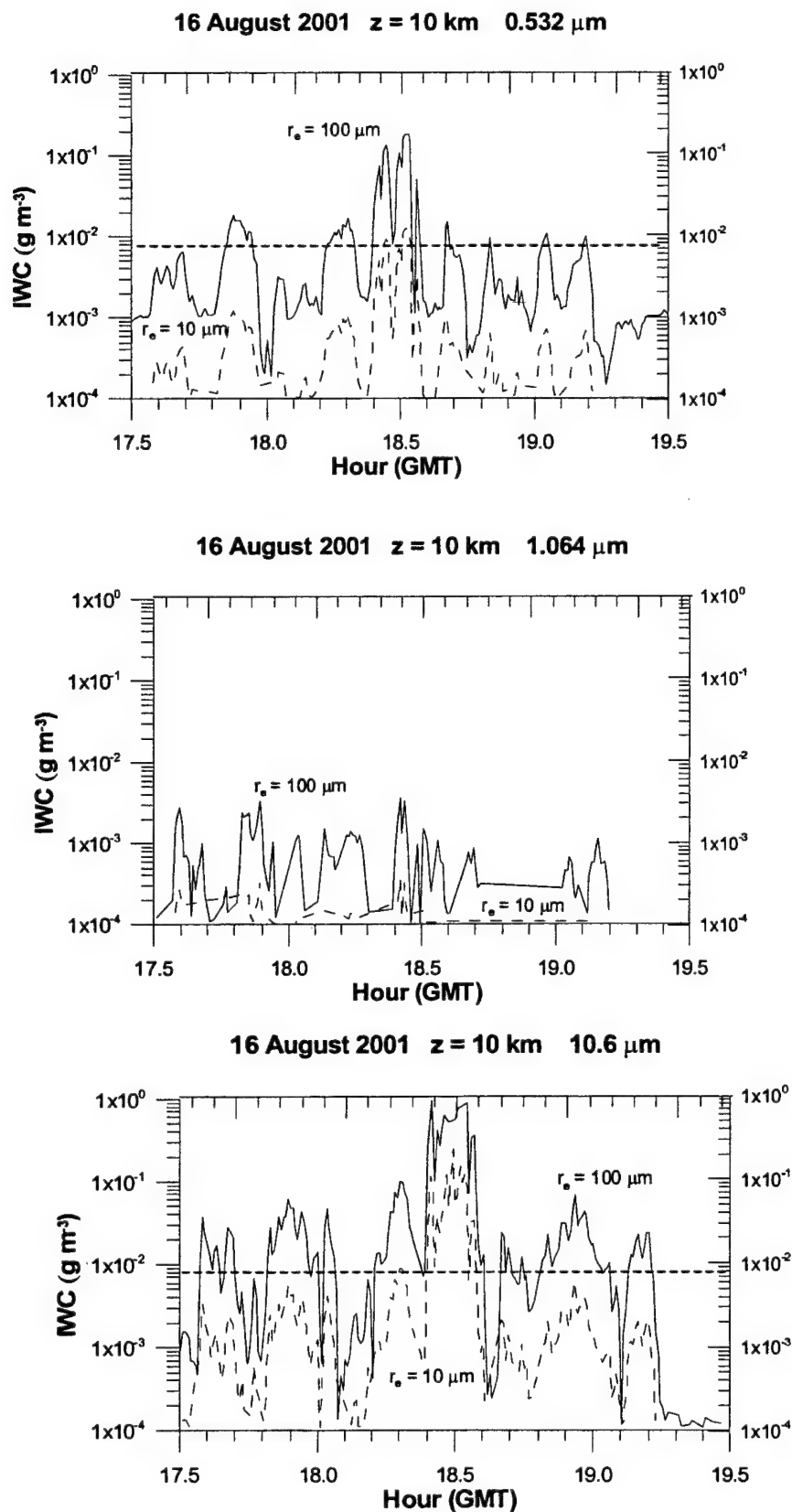


Figure 34. Ice Water Content (g m^{-3}) Calculations for 16 Aug Using Backscatter Measurements and Assuming a Modified Gamma Polydispersion of Ice Spheres

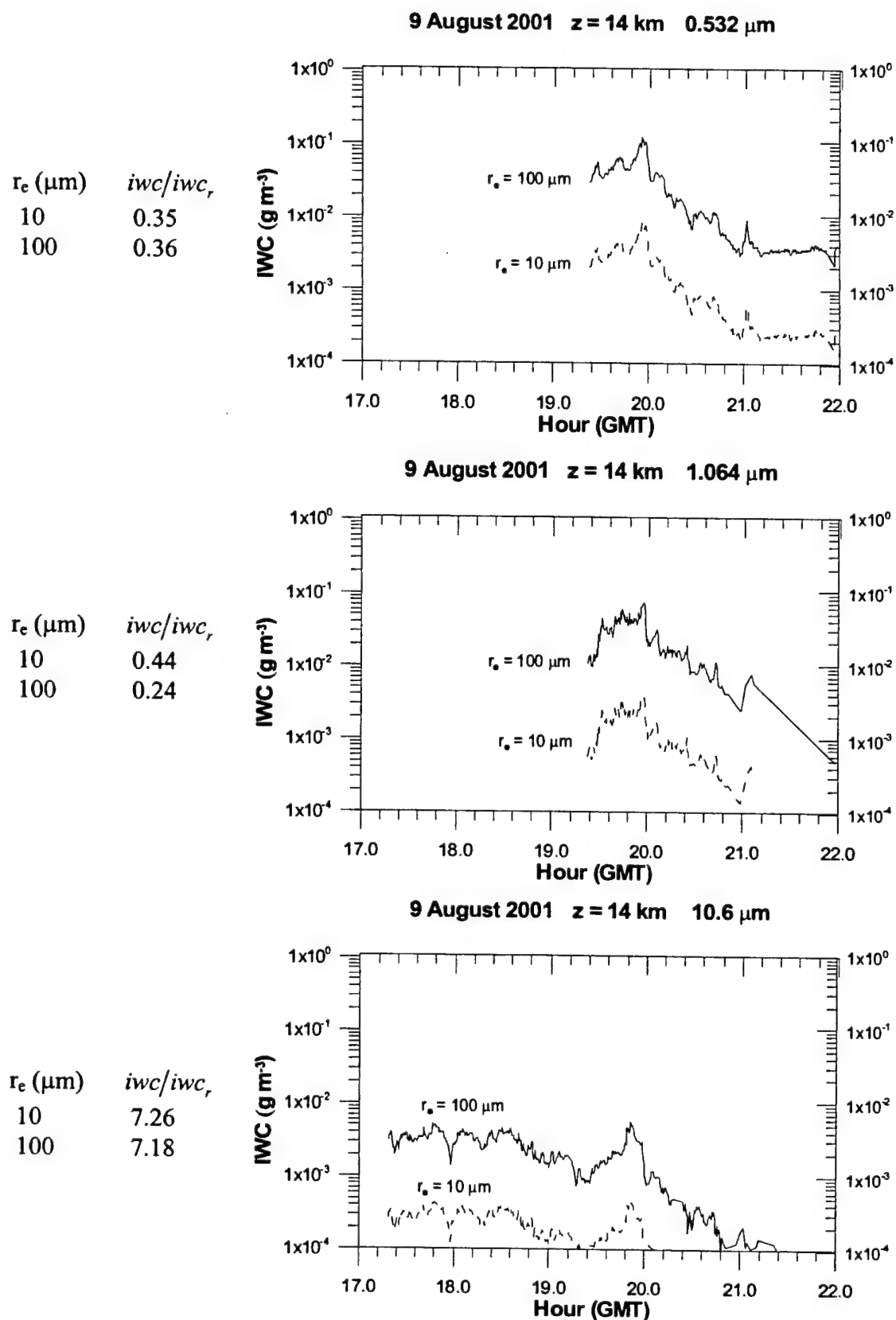


Figure 35. Ice Water Content (iwc) Calculations Using Backscatter Measurements and Assuming a Polydispersion of Long Circular Cylindrical Scatterers

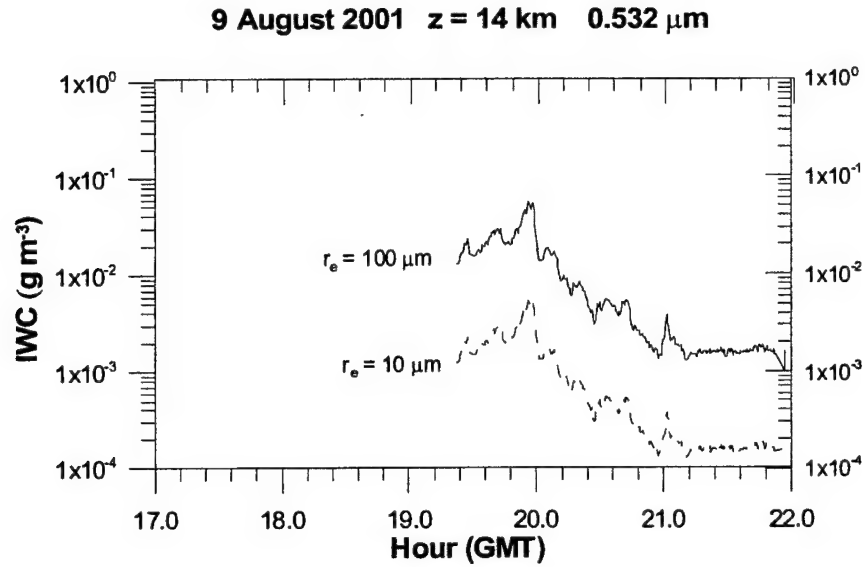


Figure 36. Time Series of ρ_{iwc} Computed for 9 August at 14 km From the Derived β_{ext} Measurements for $\lambda = 0.532 \mu\text{m}$ for the Two Equivalent Radii 10 μm and 100 μm .

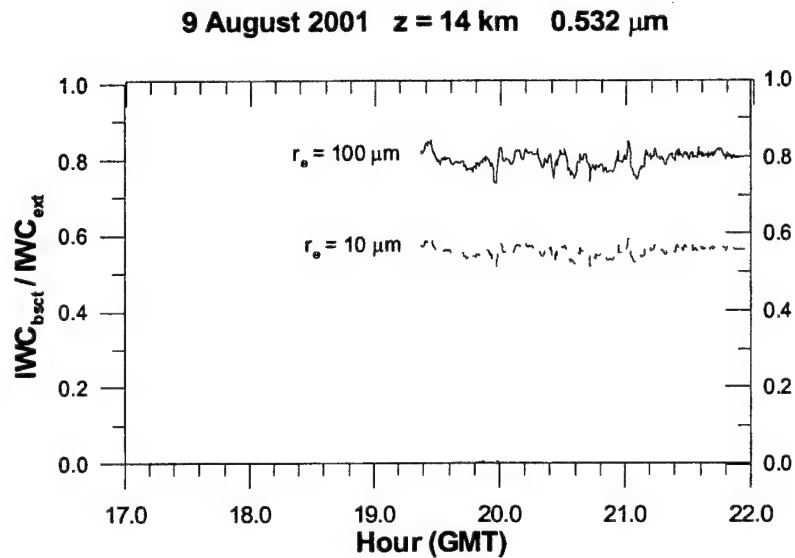


Figure 37. The Ratio of Ice Water Content Calculated using Extinction and Backscatter Measurements for 9 Aug at $\lambda = 0.532 \mu\text{m}$ for the Two Equivalent Radii 10 μm and 100 μm is Plotted as a Function of Time.

content for long circular cylinders (iwc_r) are also listed by the figures for each equivalent radius r_e . For the wavelengths of 0.532 μm and 1.064 μm , the ratio $\frac{iwc}{iwc_r}$ is less than one, ~ 0.3 to 0.4. However, for 10.6 μm , the ratio $\frac{iwc}{iwc_r}$ is significantly greater than one, being ~ 7 . This implies, that for a given particle equivalent radius, the integrated backscatter efficiency Q_{bsct} is significantly larger for long circular ice cylinders than for ice spheres at $\lambda = 10.6 \mu\text{m}$. For $\lambda = 0.532 \mu\text{m}$ and 1.064 μm , however, integrated Q_{bsct} for ice spheres is 2 – 3 times the size of the backscatter efficiency for ice cylinders.

Using Eq. (14) and Eq. (19) below, the ice water content is also calculated using the derived extinction values for $\lambda = 0.532 \mu\text{m}$ that are presented in the next section. A time series of the ice water content values calculated using the extinction coefficients is plotted for 9 August using the two equivalent radii of 10 μm and 100 μm in Figure 36. The ratio of ice water content computed from backscatter measurements and ice water content computed from the extinction measurements $\frac{iwc_{\beta_s}}{iwc_{\beta_{ext}}}$ is also plotted for the two equivalent radii and displayed in Figure 37. The ice water content ratio varies from ~ 0.55 for $r_e = 10 \mu\text{m}$ to ~ 0.80 for $r_e = 100 \mu\text{m}$. The proximity of the calculated ratios to unity indicate a similarity in the numerical integration for backscatter and extinction at $\lambda = 0.532 \mu\text{m}$ when the entire particle size distribution is spanned. This similarity exists despite the non-spherical shape of the measured ice particles and the distinct difference in character of backscatter and extinction efficiencies Q_{bsct} and Q_{ext} at optical wavelengths as a function of size parameter x (see Appendix C).

8. RANGE-RESOLVED EXTINCTION AT LIDAR WAVELENGTHS IN CIRRUS

The extinction coefficient for the Nd:YAG lidar wavelength 0.532 μm can be calculated using a technique previously applied to high altitude cirrus by Nee et al (1998). In this technique, it is assumed that the extinction-to-backscatter ratio

S where

$$S = \frac{\beta_{ext}(z)}{\beta_{\pi}(z)} \quad (sr) \quad (16)$$

is an empirical constant within the cloud and β_{ext} is the wavelength-dependent extinction coefficient. For a given cloud, an effective value of S can be determined using the equation

$$S = 2 \ln \left(\frac{\beta_{\pi}(z_1)}{\beta_{\pi}(z_2)} \right) \left[\int_{z_1}^{z_2} \beta_{\pi}(z) dz \right]^{-1} \quad (sr) \quad (17)$$

where z_1 and z_2 are the lower and upper altitude limits of the cloud. The value $\beta_{\pi}(z_2)$ is essentially the backscatter measured at the top of the cloud and $\beta_{\pi}(z_1)$ is the backscatter at the base. Since backscatter outside the cloud is dominated by Rayleigh scattering at cirrus altitudes, the upper value $\beta_{\pi}(z_2)$ is set to the value computed from Rayleigh scattering theory. The Rayleigh volume backscatter coefficient for air is expressed as

$$\beta_{\pi} = \frac{9}{N\lambda^4} \left| \frac{m^2 - 1}{m^2 + 2} \right|^2 \quad (m^{-1}sr^{-1}) \quad (18)$$

where m is the refractive index of air, N is the number of air molecules per unit volume, and λ is the optical wavelength (0.532 μm). Here $N = \frac{N_A \rho}{M}$ where N_A is Avogadro's number, ρ is the density of air, and M is the molecular weight of air. A derivation of Eq. (18) is presented in Appendix D.

Figure 38 shows a vertical profile of the Rayleigh volume backscatter coefficient β_{π} for the two lidar wavelengths, $\lambda = 0.532 \mu m$ and $\lambda = 1.06 \mu m$ computed from the radiosonde launch on 9 August (see Figure 9). For 0.532 μm , the characteristic β_{π} value is $6 \times 10^{-7} m^{-1} sr^{-1}$ at 10 km and $3 \times 10^{-7} m^{-1} sr^{-1}$ at 15 km. For $\lambda = 1.064 \mu m$, the characteristic β_{π} value is $4 \times 10^{-8} m^{-1} sr^{-1}$ at 10 km and $2 \times 10^{-8} m^{-1} sr^{-1}$ at 15 km.

For 9 August and 16 August data, the extinction-to-backscatter ratio S was determined to be 50 and 28, respectively, from the integrated lidar backscatter measurements at $\lambda =$

0.532 μm . For 14 August, a value of $S = 30$ was used, consistent with the ratio used by Nee et al (1998) and consistent with the observations by Sassen and Cho (1992). The extinction-to-backscatter ratio S can also be calculated as a function of the particle size using scattering theory along with the expression for β_π (Eq. (2)) and the expression for extinction by single scattering by a polydispersion $n(r)$:

$$\beta_{ext} = \int_0^\infty Q_{ext} n(r) \pi r^2 dr \quad (\text{m}^{-1}) \quad (19)$$

Q_{ext} is the extinction efficiency for ice spheres, which is a function of the wavelength, particle size, and particle index of refraction. Here, the extinction efficiency for spheres is defined as a function of the scattering amplitude S_1 evaluated at scattering angle $\theta = 0$:

$$Q_{ext} = \frac{4}{x^2} \text{Re}\{S_1(0)\} \quad (20)$$

where $S_1(0)$ is evaluated after van de Hulst (1957) as

$$S_1(0) = \frac{1}{2} \sum_{n=1}^{\infty} (2n+1)(a_n + b_n) \quad (21)$$

The extinction efficiency for uniform perpendicularly-oriented long cylinders is determined in an analogous form to that described by Eq. (8) for cylindrical backscatter. Results of the theoretical calculations for S for both spheres and ice cylinders are displayed in Figure 39 for a range of ice sphere equivalent radii from 0.1 μm to 350 μm along with the measured range of values (28 – 50). For particle radii greater than $\sim 1 \mu\text{m}$, the theoretical calculations of S for ice spheres range between 18 and 28, slightly less than that observed from the lidar backscatter measurements. Values of S calculated for ice cylinders with equivalent radii greater than $\sim 10 \mu\text{m}$ lie within the range of lidar-measured values.

The altitude-dependent extinction coefficient is calculated as

$$\beta_{ext}(z) = S \cdot \beta_\pi(z) \quad (\text{m}^{-1}) \quad (22)$$

where S is assumed to be constant within the cloud. There are provisions to recursively correct the backscatter to eliminate the effect of extinction. For these profiles, the corrected backscatter is then used to recalculate the extinction profile. For most cases,

the optical thickness is sufficiently small so that no recursive correction is applied. In general, the error associated with the evaluation of Eq. (22) is $\sim 1 \times 10^{-5} \text{ m}^{-1}$ (0.01 km^{-1}). There are two systematic biases associated with the derived extinction profile. First, S is applied to all altitudes over the cloud layer depth including those with and without cloud. This may result in an overestimate of extinction since S is much smaller ($\sim 8\pi/3$) for Rayleigh scatterers than for the cloudy part. Another source of bias is due to the solar background subtraction and “shutter function” effect. These types of bias should not be a problem if the higher error level of 10^{-5} m^{-1} is accepted for the extinction.

Time vs. altitude contour plots of extinction coefficient β_{ext} , computed for $\lambda = 0.532 \mu\text{m}$ using the measured backscatter and equations described above, for 9, 14, and 16 August, are shown in figures 40 through 42, respectively. Near the center of the cirrus layer from 13.8 km to 14.5 km around 20 GMT on 9 August, the extinction coefficient at $0.532 \mu\text{m}$ exceeds 0.5 km^{-1} . Over a 2 km layer depth, the extinction coefficient exceeds 0.1 km^{-1} for a period on the order of one hour on 9 August. On 14 August, the cirrus extinction coefficient is less than on 9 August with values exceeding 0.1 km^{-1} only near the center of the cirrus layer $\sim 10 \text{ km}$. For 16 August, some layers approaching a 2 km depth over which the extinction coefficient exceeds 0.5 km^{-1} are observed around 1830 GMT near 10 km and some areas exceeding 0.3 km^{-1} are found at higher altitudes between 12 and 13 km after 20 GMT. These results indicate that higher altitude cirrus ($\sim 14 \text{ km}$) unconnected with any distinct weather system or thunderstorm activity can be associated with as large or larger optical extinction values ($> 0.5 \text{ km}^{-1}$) than those associated with cirrus at lower altitudes ($\sim 9 \text{ km}$).

For comparison with passive remote sensing retrievals, the cirrus optical depth τ_c is calculated using the altitude-dependent lidar-measured extinction coefficient β_{ext} for $\lambda = 0.532 \mu\text{m}$. This is plotted as a time series in Figure 43 for the three measurement days. Here, the cirrus optical depth τ_c is defined as

$$\tau_c = \int_{z_1}^{z_2} \beta_{ext}(z) dz \quad (23)$$

where Z_1 and Z_2 represent the altitude integration limits for the observed cirrus layers. The dashed lines in Figure 43 denote the optical depth regions associated with subvisual cirrus ($\tau_c \leq 0.03$), thin cirrus ($0.03 \leq \tau_c \leq 0.30$), and cirrus up to the attenuation-limited

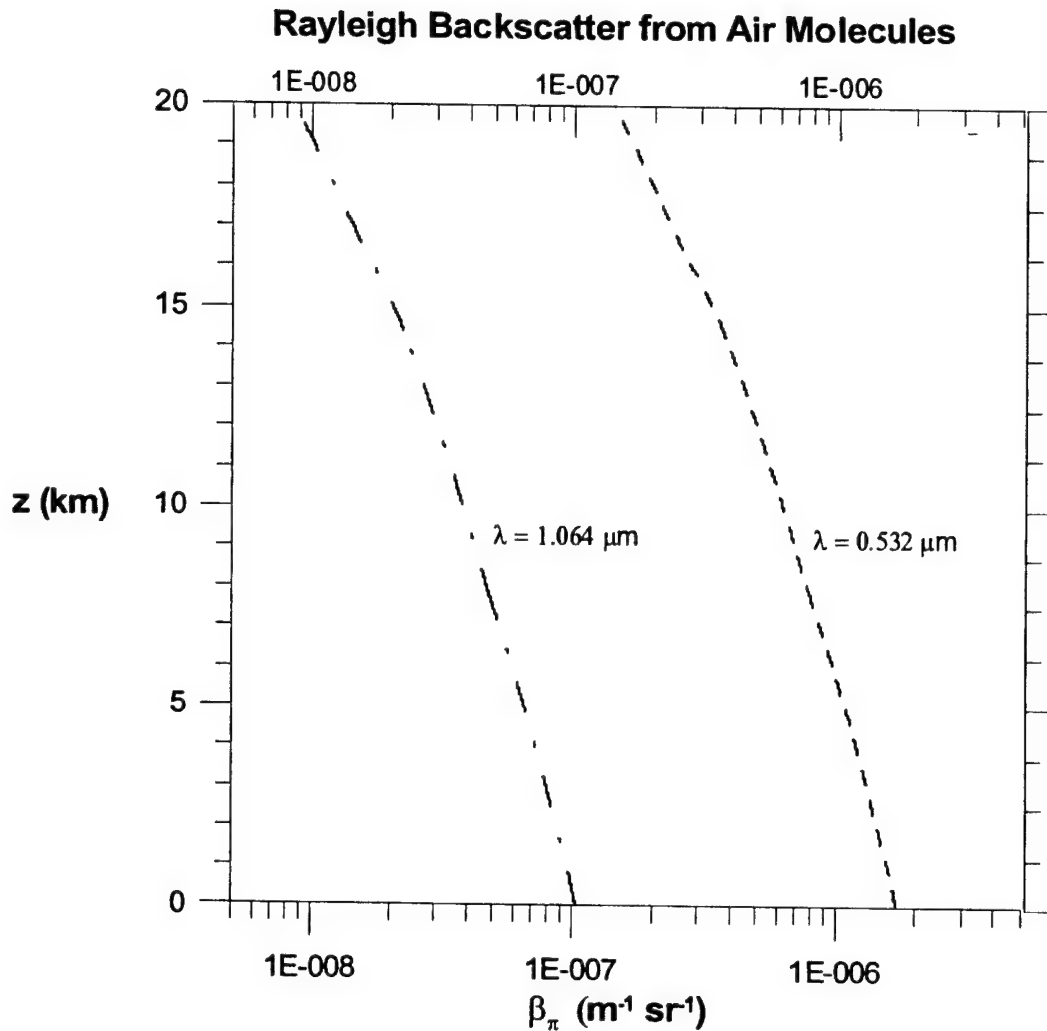


Figure 38. Rayleigh Volume Backscatter Coefficient β_π for Air Molecules for 9 August 2001 19 GMT Hanscom AFB

532 nm Extinction/Backscatter Ratio

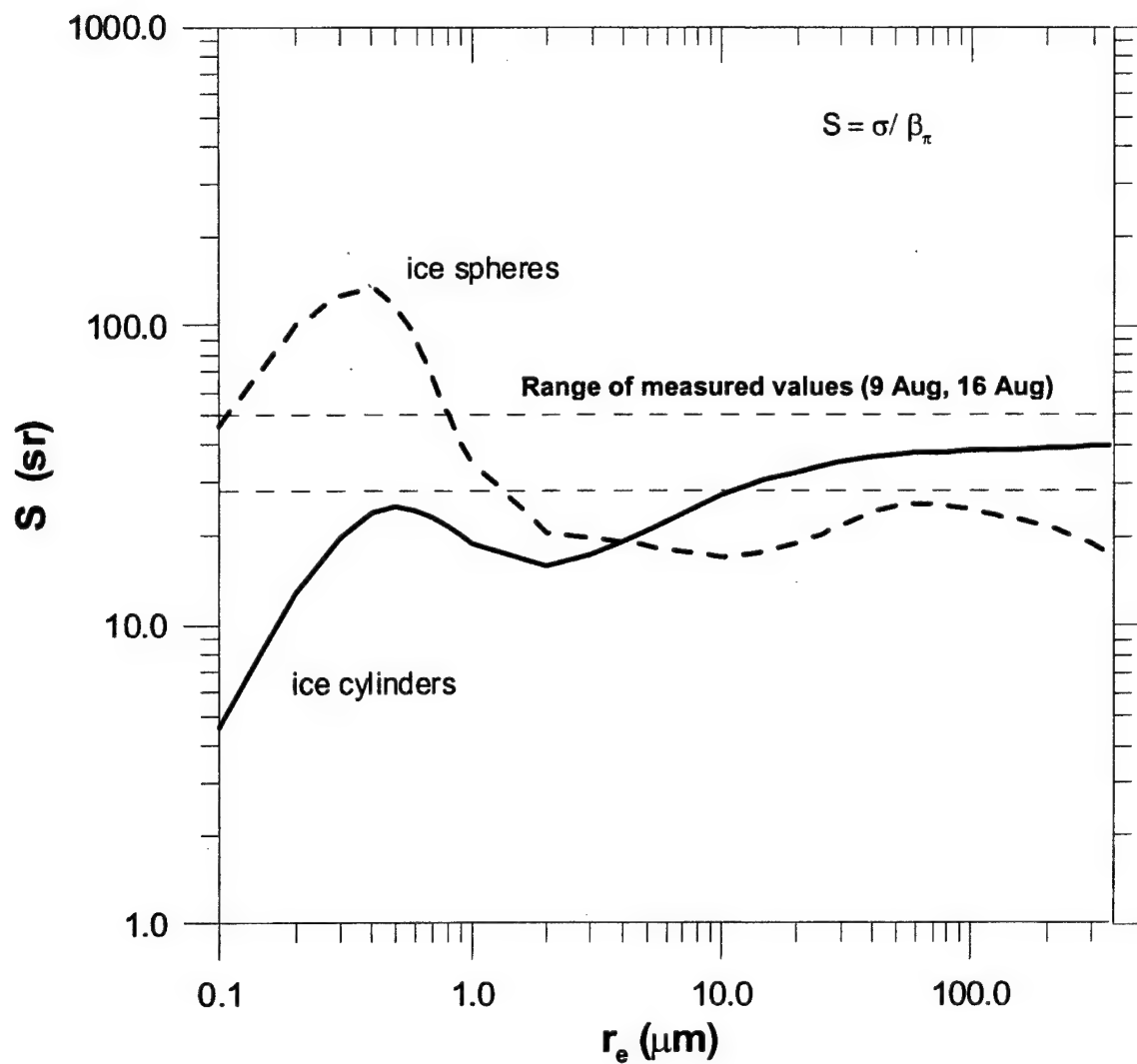


Figure 39. Extinction to Backscatter Ratio S : Measured vs. Theoretical Calculations of S at $\lambda = 0.532 \mu\text{m}$ for a Polydispersion of Ice Spheres (Dashed Line) and Long Ice Cylinders with Light at Perpendicular Incidence (Solid Line).

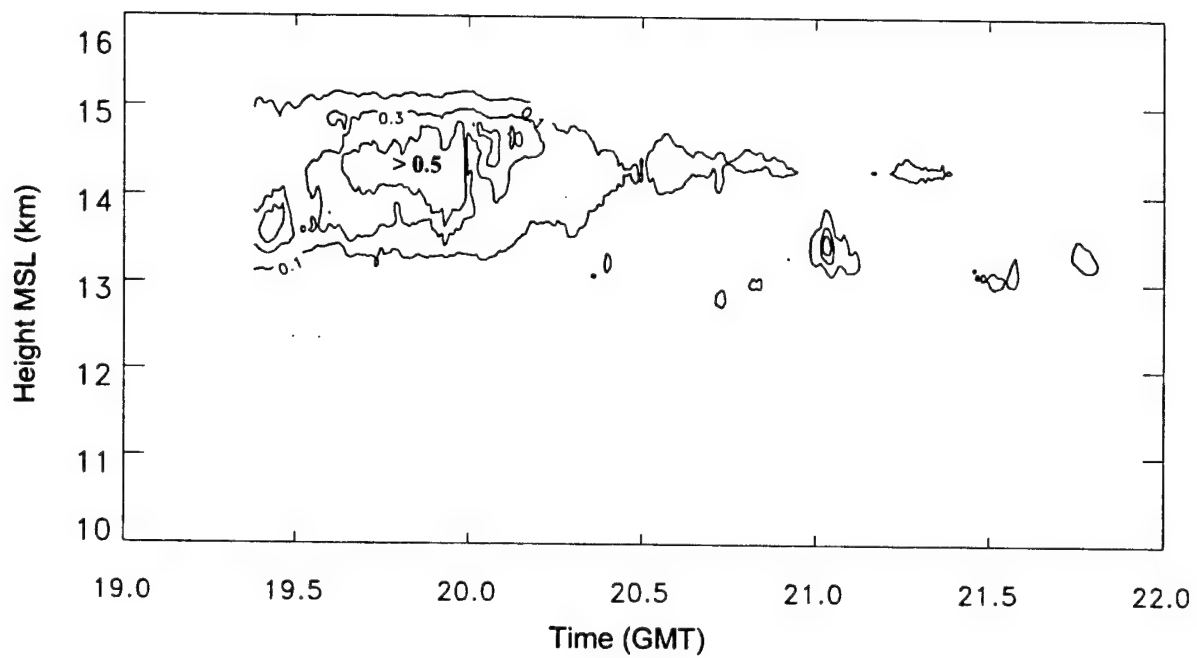


Figure 40. Measured β_{ext} at $\lambda = 0.532 \mu\text{m}$ on 9 August 2001. Contour Intervals Are: 0.1, 0.3, and 0.5 km^{-1}

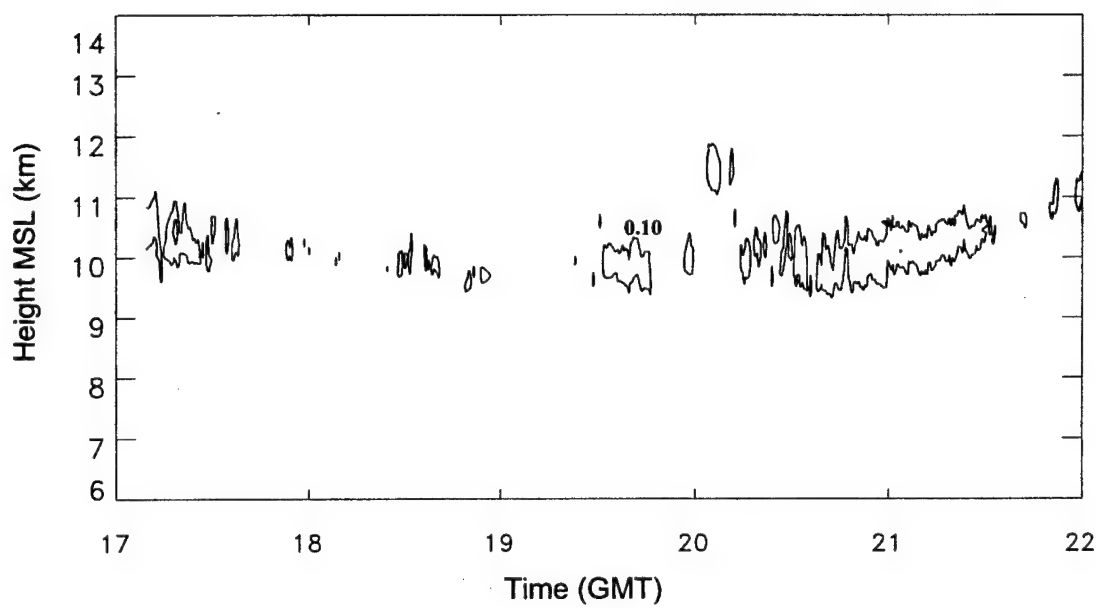


Figure 41. Measured β_{ext} (km^{-1}) at $\lambda = 0.532 \mu\text{m}$ for 14 August 2001.
Contour Intervals Are : 0.1, 0.3, and 0.5 km^{-1}

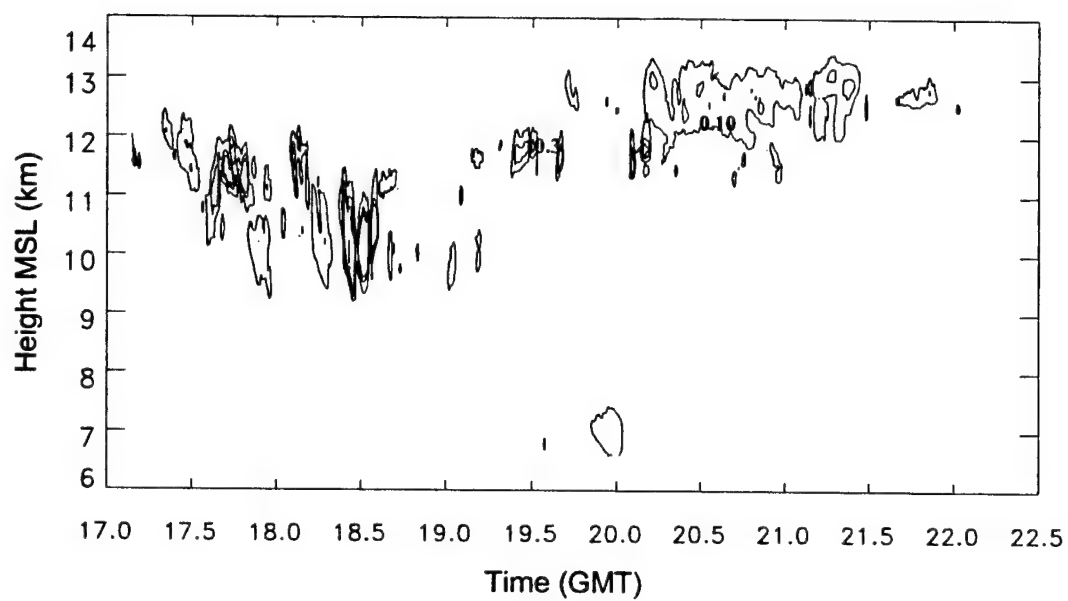


Figure 42. Measured β_{ext} (km^{-1}) at $\lambda = 0.532 \mu\text{m}$ for 16 August 2001.
Contour Intervals Are: 0.1, 0.3, and 0.5 km^{-1}

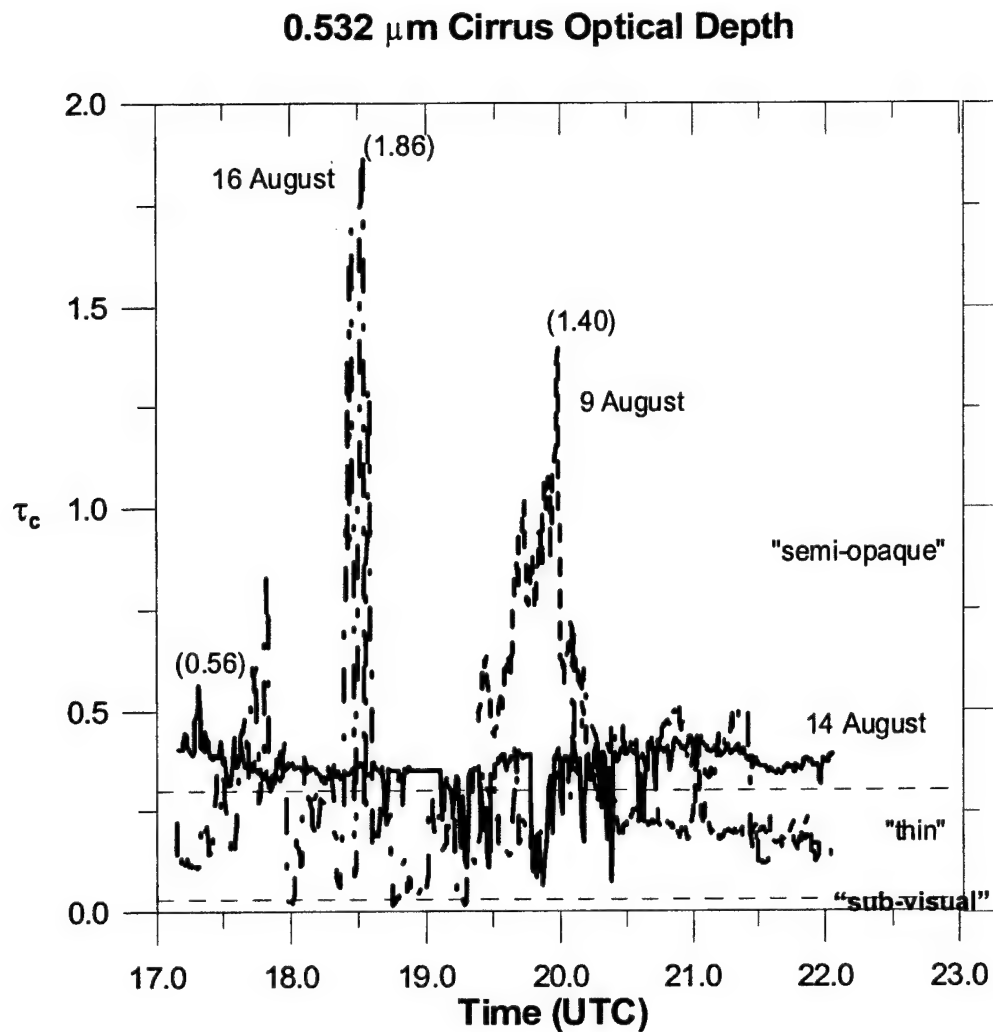


Figure 43. Time Series of Measured Cirrus Optical Depth τ_c ($\lambda = 0.532 \mu\text{m}$) for 9 August, 14 August, and 16 August 2002. Numbers in parentheses denote maximum observed values. Dashed lines mark descriptive regions of cirrus type according to optical depth (subvisual, thin, and semi-opaque) after Sassen and Cho (1992).

opacity ($0.3 \leq \tau_c \leq 3.0$) (Sassen and Cho, 1992). However, the range for subvisual values lies below the optical depth error threshold here for a 10 km thick layer (~ 0.10).

For 9 August, the integration limits Z_1 and Z_2 are 10 km and 16 km, respectively, while for 14 and 16 August, the integration limits are 6.6 km and 17 km. For 9 August, the mean cirrus optical depth τ_c is 0.39 with a maximum value of 1.40 and minimum value of 0.15. For 14 August, the mean cirrus optical depth τ_c is ~ 0.35 with a maximum of 0.56 and minimum of 0.06. For 16 August, the mean cirrus optical depth is ~ 0.29 with a maximum value of 1.86 and minimum value of 0.02. Excluding the peak areas in Figure 43, and using the optical depth criteria of Sassen and Cho (1992), thin cirrus is the predominant type during the 9 August and 16 August measurements (prior to 20 GMT), while semi-opaque cirrus is the characteristic cirrus type for 14 August.

9. SUMMARY AND CONCLUSION

Range-resolved lidar backscatter measurements of cirrus were made at three wavelengths -- $0.532 \mu\text{m}$, $1.064 \mu\text{m}$, and $10.591 \mu\text{m}$ -- over a temperature range of -30°C to -70°C and altitude range of 9 km to 15.5 km on several days in August 2001 at Hanscom AFB, Massachusetts. Three days were selected for analysis and study -- 9 August, 14 August, and 16 August. The cirrus backscatter measurements were analyzed in combination with scattering theory calculations to better understand their behavior with respect to wavelength, characteristic particle size, ice water content, and comparative optical properties.

Lidar-measured volume backscatter coefficients β_π were analyzed for the three wavelengths as a function of time and altitude. For $\lambda = 0.532 \mu\text{m}$ and $1.064 \mu\text{m}$, $\log_{10} \beta_\pi$ magnitudes ranged from -4.5 to $-6.0 \text{ m}^{-1} \text{ sr}^{-1}$ within the cirrus cloud area, with values of -5.0 frequently occurring near the cloud center, while $\log_{10} \beta_\pi$ magnitudes for $\lambda = 10.6 \mu\text{m}$ ranged typically from -6.5 to $-8.5 \text{ m}^{-1} \text{ sr}^{-1}$ with typical cloud center values

near -7.0 . The measured volume backscatter coefficient ratios γ_π were determined as a function of time and altitude for the wavelength ratios 10.6/1.064 and 10.6/0.532.

The measured backscatter ratio magnitudes γ_π were compared with magnitudes computed from scattering theory for both ice spheres and long circular cylinders using a modified gamma particle size distribution $n(r)$. Measured γ_π (10.6/0.532) during the three measurement days ranged from 1×10^{-3} to 1×10^{-1} while measured γ_π (1.064/0.532) ranged from 0.1 – 1.30. General agreement existed between the overall range of measured backscatter ratio magnitudes and those computed from theory for both wavelength pairs, but there was no consistent information which could be discerned concerning characteristic cirrus particle size associated with the γ_π measurements and the behavior of the theoretical backscatter ratio function as a particle size.

Assuming the modified gamma particle size distribution and given an equivalent or modal particle size, calculations of the time series of ice water content ρ_{iwc} were made from the backscatter measurements at the three wavelengths using scattering theory. Typical values of ρ_{iwc} computed for 9 August 20 GMT at 14 km ranged from $\sim 1 \times 10^{-3}$ g m $^{-3}$ to $\sim 5 \times 10^{-2}$ g m $^{-3}$ for an equivalent sphere radius of 100 μm while the calculated ice water content for an equivalent sphere radius of 10 μm was smaller by more than an order of magnitude. ρ_{iwc} values significantly exceeding 1×10^{-2} g m $^{-3}$, given $r_e = 100$ μm , were observed on 16 August for β_π for both $\lambda = 0.532$ μm and 10.6 μm and for 10.6 μm on 14 August. Similar calculations were also performed for long ice cylinders assuming uniform orientation and light of perpendicular incidence. For the shorter wavelengths (0.532 μm and 1.064 μm), ρ_{iwc} calculated assuming cylinders exceeded that for spheres by a factor of 2 or 3, while ρ_{iwc} calculated assuming spheres exceeded that computed for ice cylinders by a factor of seven for backscatter at 10.6 μm .

Using knowledge of the Rayleigh backscatter coefficient ($\text{m}^{-1} \text{sr}^{-1}$) for air molecules, the cirrus backscatter, and assuming a constant value in-cloud, estimates of extinction-to-backscatter ratio S (sr) in cirrus were computed for 9 and 16 August for $\lambda = 0.532 \mu\text{m}$. The measured values of S ranged from 28 sr to 50 sr. The measured values of S agreed generally with theoretical values for both ice spheres and long ice cylinders for particle size distributions where the equivalent radii exceeded $\sim 1 \mu\text{m}$. The derived values of S were applied to the time and height profiles of the measured cirrus β_π to produce corresponding estimates of cirrus particle extinction β_{ext} (m^{-1}). These estimates showed β_{ext} at $\lambda = 0.532 \mu\text{m}$ exceeding 0.5 km^{-1} on 9 August and 16 August near 14 km and near 10 km altitude, respectively, and β_{ext} exceeding 0.1 km^{-1} in the vicinity of 10 km on 14 August. These cirrus extinction profiles correspond to peak optical depth values τ_c of 1.4 and 1.9 on 9 August and 16 August, respectively, and 0.6 on 14 August.

These results also imply that accurate determination of characteristic and bulk microphysical properties of cirrus clouds will be difficult, at best, using only lidar backscatter measurements. This is a result of the nearly constant backscatter coefficient ratio γ_π for optical wavelength pairs over a wide range of modal or characteristic particle size parameters. For cirrus, the characteristic sizes of the polydispersion usually exceed the few μm threshold where the onset of a nearly constant lidar backscatter ratio γ_π is encountered. The availability of backscatter β_π measurements at longer wavelengths, such as $\lambda = 3.2 \text{ mm}$ or $\lambda = 8.6 \text{ mm}$ for cloud radar, should significantly increase the variation of γ_π with size parameter when paired with optical wavelengths.

References

- Aden, A.L., 1951: Electromagnetic scattering from spheres with sizes comparable to the wavelength. *J. Appl. Phys.*, **22**, 601- 605.
- Infeld, L., 1947: The influence of the width of the gap upon the theory of antennas. *Quart. Appl. Math.*, **5**, 113-132.
- Intrieri, J.M., G. L. Stephens, W.L. Eberhard, and T. Uttal, 1993: A method for determining cirrus cloud particle sizes using lidar and radar backscatter technique. *J. Appl. Met.*, **32**, 1074 – 1082.
- Heymsfield, A.J., 1977: Precipitation development in stratiform ice clouds: a microphysical and dynamical study. *J. Atmos. Sci.*, **34**, 367-381.
- Heymsfield, A.J., 1994: Microphysical structures of stratiform and cirrus clouds, in *Aerosols-Cloud-Climate Interactions*, ed. P.V. Hobbs, Academic Press, New York, 233 pp.
- Kattawar, G.W., and G.N. Plass, 1967: Electromagnetic scattering from absorbing spheres. *Appl. Opt.*, **6**, 1377-1382.
- Kerker, M., 1969: *The Scattering of Light and Other Electromagnetic Radiation*. Academic Press, New York, 666 pp.
- Nee, J.B., C.N. Len, W.N. Chen, and C.I. Lin, 1998: Lidar observations of cirrus clouds in the tropopause at Chung-Li (25N, 121E). *J. Atmos. Sci.*, **55**, 2249-2257.
- O'Brien, J.J., 1970: Alternative solutions to the classical vertical velocity problem. *J. Appl. Met.*, **9**, 197- 203.
- Rothman, L.S., R. R. Gamache, R.H. Tipping, C.P. Rinsland, M.A.H. Smith, D. C. Benner, V.M. Devi, J.-M. Flaud, C. Camy-Peyret, A. Perrin, A. Goldman, S.T. Massie, L. R. Brown, and R.A. Toth, 1992: The HITRAN molecular database: Editions of 1991 and 1992. *J. Quant. Spectrosc. Radiat. Transfer*, **48**, 469-507.
- Sassen, K., and B.S. Cho, 1992: Sub-visual thin cirrus lidar dataset for satellite verification and climatological research. *J. Appl. Met.*, **31**, 1275-1285.
- Takano, Y., and K.N. Liou, 1995: Radiative transfer in cirrus clouds: Part III: Light scattering by irregular ice crystals. *J. Atmos. Sci.*, **52**, 818 – 837.
- van de Hulst, H.C., 1957: *Light Scattering by Small Particles*. Dover Publications, New York, 470 pp.

Warren, S.G., 1984: Optical constants of ice from the ultraviolet to the microwave.
Appl. Opt., **23**, 1206-1225.

APPENDIX A. CALCULATION OF SCATTERING COEFFICIENTS FOR A SPHERE

A rather straightforward algorithm for calculating the spherical scattering coefficients and handling their recursion problem was derived by Aden (1951). Here the scattering coefficients are defined as

$$a_n = \frac{j_n(x)}{h_n^{(2)}(x)} \left\{ \frac{\sigma_n(x) - m\sigma_n(y)}{\rho_n(x) - m\sigma_n(y)} \right\} \quad (\text{A1})$$

$$b_n = \frac{j_n(x)}{h_n^{(2)}(x)} \left\{ \frac{\sigma_n(y) - m\sigma_n(x)}{\sigma_n(y) - m\rho_n(x)} \right\} \quad (\text{A2})$$

where

$$\rho_n(x) \equiv \frac{d}{dx} \ln [x h_n^{(2)}(x)] = \frac{h_{n-1}^{(2)}(x)}{h_n^{(2)}(x)} - \frac{n}{x} \quad (\text{A3})$$

and

$$\sigma_n(x) \equiv \frac{d}{dx} \ln [x j_n(x)] = \frac{j_{n-1}(x)}{j_n(x)} - \frac{n}{x} \quad (\text{A4})$$

are expressed in terms of the Riccati-Bessel functions $j_n(x)$, $n_n(x)$.

For the lowest orders, integers $n = 0, n = 1$

$xj_n(x)$, $xn_n(x)$ are defined as:

$$\begin{aligned} xj_0(x) &= \sin x \\ xj_1(x) &= \frac{\sin x}{x} - \cos x \end{aligned} \quad (\text{A5})$$

$$\begin{aligned}
xn_0(x) &= -\cos x \\
xn_1(x) &= \frac{-\cos x}{x} - \sin x
\end{aligned}
\tag{A6}$$

Noting that $y = mkr = mx$; $m = m(\lambda) = m_r - im_i$, the complex index of refraction where $i = \sqrt{-1}$, requires the use of complex variables such that

$$z = x + iy \text{ then } |z|^2 = (x^2 + y^2) ; \text{ also } \bar{z} = x - iy, |\bar{z}| = |z|$$

Given $y = m_r x - im_i x$ then

$$\begin{aligned}
\sin y &= \sin(m_r x) \cosh(-m_i x) + i \cos(m_r x) \sinh(-m_i x) \\
\cos y &= \cos(m_r x) \cosh(-m_i x) - i \sin(m_r x) \sinh(-m_i x)
\end{aligned}$$

Higher order terms of the Riccati-Bessel functions can be determined using recursion relations for spherical Bessel functions --also known as Bessel functions of fractional order:

$$\begin{aligned}
j'_n(x) &= j_{n-1}(x) - \frac{n+1}{x} j_{n+1}(x) \\
j_{n+1}(x) &= \frac{(2n+1)}{x} j_n(x) - j_{n-1}(x)
\end{aligned}
\tag{A7}$$

$$\text{and } h_n^{(2)}(x) = j_n(x) - in_n(x)$$

which is the second Hankel function of order n. The Hankel function employs the same recursion relations as other spherical Bessel functions.

In the case of spherical Bessel functions, if significant imaginary components exist in the index of refraction, the arguments for the hyperbolic trigonometric functions can, as x increases, become too large for the machine data type and floating point overflow will

occur. This can be avoided by expressing (4) in exponential form and factoring out exponential terms in the numerator and denominator which have a positive exponent.

The recursion relation for the logarithmic derivatives derived from Infeld (1947) is:

$$\sigma_n(x) = \frac{x^2 + nx\sigma_{n-1}(x) - n^2}{nx - x^2\sigma_{n-1}(x)} \quad (\text{A8})$$

Thus, using the logarithmic derivatives (3,4), recursion relations, and (8), the scattering coefficients a_n and b_n can readily be calculated.

Given the expression for scattering efficiency Q_{sct} and extinction efficiency Q_{ext} (van de Hulst, 1957)

$$Q_{sct} = \frac{2}{x^2} \sum_{n=1}^{\infty} (2n+1) \{ |a_n|^2 + |b_n|^2 \} \quad (\text{A9})$$

$$Q_{ext} = \frac{2}{x^2} \sum_{n=1}^{\infty} (2n+1) \text{Re}(a_n + b_n) \quad (\text{A10})$$

convergence criteria for evaluating all sphere scattering efficiency calculations were set arbitrarily as:

$$\left[|Q_{sct}(n) - Q_{sct}(n-1)| \frac{x^2}{2} \text{ and } |Q_{ext}(n) - Q_{ext}(n-1)| \frac{x^2}{2} \right] < 10^{-9}$$

Stephens (1961) discussed the numerical mode which develops when calculating the extinction and scattering efficiencies Q_{ext} , Q_{sct} for water spheres and becomes negatively unbounded as the size parameter $x \rightarrow 0$. Encounters with this mode may occur, in practice, at microwave or lower frequencies. One remedy is to use van de Hulst's (1957)

series expansion for small x ($\sim x < 0.01$) in lieu of the standard determination using amplitude coefficients:

$$Q_{ext} = -\text{Im} \left\{ 4x \frac{m^2 - 1}{m^2 + 2} + \frac{4}{15} x^3 \left(\frac{m^2 - 1}{m^2 + 2} \right)^2 \frac{m^4 + 27m^2 + 38}{2m^2 + 3} \right\} + x^4 \text{Re} \left\{ \frac{8}{3} \left(\frac{m^2 - 1}{m^2 + 2} \right)^2 \right\} + \dots \quad (\text{A11})$$

$$Q_{scf} = x^4 \frac{8}{3} \left| \frac{m^2 - 1}{m^2 + 2} \right|^2 + \dots$$

For very small x and mx Rayleigh scattering (e.g. $x < 0.01$), series expansions should also be used for calculation of the scattering amplitudes S_1 and S_2 . Following van de Hulst (1957), these are:

$$S_1 = \frac{isx^3}{2} \left[3 + (3t + 3u \cos \theta + 5w \cos \theta) x^2 - 3isx^3 + \dots \right] \quad (\text{A12})$$

$$S_2 = \frac{isx^3}{2} \left[3 \cos \theta + (3t \cos \theta + 3u + 5w \cos 2\theta) x^2 - 3isx^3 \cos \theta + \dots \right] \quad (\text{A13})$$

where

$$s = \frac{2}{3} \frac{m^2 - 1}{m^2 + 2}, \quad t = \frac{3}{5} \frac{m^2 - 2}{m^2 + 2},$$

$$u = \frac{1}{30} (m^2 + 2), \quad w = \frac{1}{10} \frac{m^2 + 2}{m^2 + 3};$$

References

Aden, A.L., 1951: Electromagnetic scattering from spheres with sizes comparable to the wavelength. *J. Appl. Phys.*, **22**, 601-605.

Infeld, L., 1947: The influence of the width of the gap upon the theory of antennas. *Quart. Appl. Math.*, **5**, 113-132.

Stephens, J.J., 1961: Spectrally averaged total attenuation, scattering, and absorption cross-sections of infrared radiation. *J. Meteor.*, **18**, 822-828.

van de Hulst, H.C., 1957: *Light Scattering by Small Particles*. Dover, New York, 470 pp.

APPENDIX B: CALCULATION OF SCATTERING EFFICIENCIES FOR A LONG CIRCULAR CYLINDER (ROD)

Solutions for the scattering coefficients a_n and b_n at perpendicular incidence are expressed in terms of the Bessel functions of integer order (van de Hulst (1957), Kerker (1969)):

$$\text{Case 1:} \quad b_n = \frac{mJ'_n(y)J_n(x) - J_n(y)J'_n(x)}{mJ'_n(y)H_n(x) - J_n(y)H'_n(x)} \quad (\text{B1})$$

$$\text{Case 2:} \quad a_n = \frac{J'_n(y)J_n(x) - mJ_n(y)J'_n(x)}{J'_n(y)H_n(x) - mJ_n(y)H'_n(x)} \quad (\text{B2})$$

Here, J_n is the Bessel function of the first kind of order n where primes denote first derivatives, m is the complex index of refraction $m = m_r - im_i$ of the scatterer where

$i = \sqrt{-1}$, $x = \frac{2\pi r}{\lambda}$, the size parameter, and $y = mx$. $H_n(x)$ is the Hankel function of the second kind, $H_n^{(2)}(x) = J_n(x) - iY_n(x)$, where $Y_n(x)$ is the Bessel function of the second kind of order n . $Y_n(x)$ is also referred to as the Neumann or Weber function.

The Bessel functions of integer order are calculated using a series expansion for $x \leq 30$ and an asymptotic expression for $x > 30$. For Bessel functions of the first kind J_n , these expressions are:

$$J_\nu(z) = \sum_{n=0}^{\infty} \frac{(-1)^n (1/2z)^{2n+\nu}}{n! \Gamma(\nu+n+1)} \quad (\text{series}) \quad x \leq 30 \quad (\text{B3a})$$

$$J_\nu(z) = \sqrt{2/\pi z} \cos\left(z - \frac{1}{2}\nu\pi - \frac{1}{4}\pi\right) \quad (\text{asymptotic}) \quad x > 30 \quad (\text{B3b})$$

where ν and n are integers, Γ is the gamma function, and z may be real (x) or complex (y).

For Bessel functions of the second kind Y_n , the Weber or Neumann functions, the equations used are:

$$Y_n(z) = -\frac{\left(\frac{1}{2}z\right)^{-n}}{\pi} \sum_{k=0}^{n-1} \frac{(n-k-1)!}{k!} \left(\frac{1}{4}z^2\right)^k + \frac{2}{\pi} \ln\left(\frac{1}{2}z\right) J_n(z) - \frac{\left(\frac{1}{2}z\right)^n}{\pi} \sum_{k=0}^{\infty} \left\{ \psi(k+1) + \psi(n+k+1) \right\} \cdot \frac{\left(-\frac{1}{4}z^2\right)^k}{k!(n+k)!} \quad (\text{series}) \quad x \leq 30 \quad (\text{B4a})$$

$$\psi(1) = -\gamma \quad (\text{Euler's constant} \sim 0.5772....)$$

where

$$\psi(n) = -\gamma + \sum_{k=1}^{n-1} k^{-1}$$

$$Y_n(z) = \sqrt{2/(\pi z)} \sin\left(z - \frac{1}{2}n\pi - \frac{1}{4}\pi\right) \quad (\text{asymptotic}) \quad x > 30 \quad (\text{B4b})$$

Equations (B3) and (B4) can be found in Chapter 9 of Abramowitz and Stegun (1964) and other texts such as Arfken (1985). Appropriate series and asymptotic size parameter regimes were determined empirically and checked against the Harvard computation tables (1947), tables in Abramowitz and Stegun (1964), and Jahnke and Emde (1945).

In practice, only the functions for integer orders 0 and 1 are determined using the given values of x and y . The higher order Bessel functions needed for evaluation of Eqs. (B1) and (B2) including the first derivatives are calculated using the following recursion relations:

$$\text{forward:} \quad Y_{n+1}(z) = \frac{2n}{z} Y_n(z) - Y_{n-1}(z) \quad (\text{B5a})$$

$$\text{backward:} \quad J_{n-1}(z) = \frac{2n}{z} J_n(z) - J_{n+1}(z) \quad (\text{B5b})$$

first derivative:
$$J'_n(z) = J_{n-1}(z) - \frac{n}{z} J_n(z) \quad (\text{B5c})$$

Forward recursion can be used for Bessel functions of the second kind (Weber functions) while backward recursion must be used for Bessel functions of the first kind. The backward or downward recursion is performed using a technique described by Abramowitz and Stegun (1964) and attributed to J.C.P. Miller (Bickley et al, 1952). As opposed to the spherical or Bessel functions of fractional order, the appearance of numerical error in forward recursion using Eq. (B5a) appears for integer orders as small as 9 or 10. Also, the downward recursion algorithm seems to require more care in determining the "starting" n value compared to the spherical Bessel functions.

A hybrid recursion scheme was used due to the floating point overflow encountered in the asymptotic form of Eq. (B3b), which occurs when a significant imaginary component $m_i * x$ is reached for the complex size parameter y . Using "standard" procedures, the scattering coefficients are expressed explicitly in terms of the Bessel functions. Another approach is to rewrite the scattering coefficients in terms of the derivative of the logarithm for the Bessel functions of the first kind with complex argument, and by factoring, eliminate the positive imaginary exponents that cause the overflow. To accomplish this, Eqs. (B1) and (B2) are re-written as

$$b_n = \frac{m\sigma_n(y)J_n(x) - J'_n(x)}{m\sigma_n(y)H_n(x) - H'_n(x)} \quad (\text{B6})$$

$$a_n = \frac{\sigma_n(y)J_n(x) - mJ'_n(x)}{\sigma_n(y)H_n(x) - mH'_n(x)} \quad (\text{B7})$$

where $\sigma_n(y) = \frac{d}{dy} \ln[J_n(y)]$. Infeld's (1947) recursion relation

$$\sigma_n(y) = \frac{y^2 + ny\sigma_{n-1}(y) - n^2}{ny - y^2\sigma_{n-1}(y)} \quad (\text{B8})$$

is applied to the logarithmic basis functions (orders 0 and 1) and using downward recursion, the scattering coefficients can then be calculated for any order n . Given $y = x_r + x_i$ where $x_r = m_r x$ and $x_i = -m_i x$, the derivative of the logarithmic basis function for order 0, using Eq. (B3b), is:

$$\sigma_0(y) = \frac{1 + [\cos(2x_r) - i \sin(2x_r)](-ie^{2x_i})}{-i + [\cos(2x_r) - i \sin(2x_r)]e^{2x_i}} \quad (B9)$$

Evaluation of Eqs. (B3) – (B9) were accomplished for size parameters ranging from 1×10^{-10} to 100,000 and for integer orders exceeding 80,000. The Bessel function calculations were compared with tables 9.1 and 9.4 in Abramowitz and Stegun (1964) for size parameters x and integer orders up to 100 and with the tables of Chapter 8 in Jahnke and Emde (1945).

Given the expression for scattering efficiency Q_{scf} and extinction efficiency Q_{ext} (van de Hulst, 1957)

Case 1: $v = 0$, (E || axis)

$$Q_{ext} = \frac{2}{x} \sum_{n=-\infty}^{\infty} \text{Re } b_n = \frac{2}{x} \left[\text{Re } b_0 + 2 \sum_{n=1}^{\infty} \text{Re } b_n \right] ; \quad Q_{scf} = \frac{2}{x} \sum_{n=-\infty}^{\infty} |b_n|^2 = \frac{2}{x} \left[|b_0|^2 + 2 \sum_{n=1}^{\infty} |b_n|^2 \right] \quad (B10)$$

Case 2: $u = 0$, (H || axis)

$$Q_{ext} = \frac{2}{x} \sum_{n=-\infty}^{\infty} \text{Re } a_n = \frac{2}{x} \left[\text{Re } a_0 + 2 \sum_{n=1}^{\infty} \text{Re } a_n \right] ; \quad Q_{scf} = \frac{2}{x} \sum_{n=-\infty}^{\infty} |a_n|^2 = \frac{2}{x} \left[|a_0|^2 + 2 \sum_{n=1}^{\infty} |a_n|^2 \right] \quad (B11)$$

where E and H denote the electric and magnetic field vector amplitudes, respectively, convergence criteria for evaluating all cylindrical scattering efficiency calculations were set arbitrarily, using the Case 1 functions, as:

$$\left[\left| Q_{scf}(n) - Q_{scf}(n-1) \right| \frac{x^2}{2} \text{ and } \left| Q_{ext}(n) - Q_{ext}(n-1) \right| \frac{x^2}{2} \right] < 10^{-9}$$

References

Abramowitz, M., and I.A. Stegun, 1964: *Handbook of Mathematical Functions*. New York, Dover Press, 1046 pp.

Arfken, G., 1985: *Mathematical Methods for Physicists*. Academic Press, Inc., New York, 985 pp.

Bickley, W.G., L.J. Comrie, D.H. Sadler, J.C.P. Miller, and A.J. Thompson, 1952: *Mathematical Tables Vol. X. Bessel Functions Part II Functions of Positive Integer Order*. British Association for the Advancement of Science, University Press, Cambridge.

Harvard Computation Laboratory, 1947: *Tables of the Bessel Functions of the First Kind of Orders Zero and One*. Harvard University Press, Cambridge, Massachusetts.

Infeld, L., 1947: The influence of the width of the gap upon the theory of antennas. *Quart. Appl. Math.*, **5**, 113-132.

Jahnke, E., and F. Emde, 1945: *Tables of Functions with Formulae and Curves*. Dover Publications, New York, 382 pp.

Kerker, M., 1969: *The Scattering of Light and Other Electromagnetic Radiation*. New York, Academic Press, 666 pp.

van de Hulst, H.C., 1957: *Light Scattering by Small Particles*. Dover Press, New York, 470 pp.

APPENDIX C: NORMALIZED BACKSCATTER AND EXTINCTION KERNEL FUNCTIONS FOR ICE SPHERES AT LIDAR WAVELENGTHS

Given expressions for volume backscatter and extinction coefficients for a polydispersion of spheres:

$$\beta_{\pi}(r, \lambda, m) = \int_0^{\infty} \frac{Q_{bsct}(m, r, \lambda)}{4\pi} n(r) \pi r^2 dr \quad (\text{m}^{-1} \text{ sr}^{-1}) \quad (\text{C1})$$

$$\beta_{ext}(r, \lambda, m) = \int_0^{\infty} Q_{ext}(m, r, \lambda) n(r) \pi r^2 dr \quad (\text{m}^{-1}) \quad (\text{C2})$$

these can be written in a generalized form

$$g(x, \lambda, m) = \int_{x_a}^{x_b} K(x, \lambda, m) f(x) dx \quad (\text{C3})$$

where $x \equiv \ln r$, $g(x, \lambda, m)$ is either the volume backscatter or extinction coefficient, $K(x, \lambda, m)$ is a kernel function, and $f(x)$ is the size distribution function. In practice (e.g. Qing et al, 1989), $f(x)$ can be expressed as the non-dimensional volume density function

$$f(x) = \frac{4\pi}{3} r^3 \frac{dN}{d \ln r} \quad (\text{C4})$$

given $n(r) = \frac{dN}{dr}$, and K is expressed as:

$$K(x, \lambda, m) = \frac{3}{4r} Q_L \quad (\text{m}^{-1} \text{ sr}^{-1} \text{ or } \text{m}^{-1}) \quad (\text{C5})$$

where $Q_L = \frac{Q_{bsct}}{4\pi}$ or Q_{ext} .

Normalized plots of the kernel functions K as a function of ice sphere radius for the three lidar wavelengths are shown below.

For lidar backscatter kernels associated with ice spheres, the particle radius range of influence runs from $\sim 0.1 \mu\text{m}$ to $\sim 10 \mu\text{m}$ for the shorter wavelengths ($0.532 \mu\text{m}$ and $1.064 \mu\text{m}$) and $\sim 1 \mu\text{m}$ to $\sim 10 \mu\text{m}$ for $\lambda = 10.6 \mu\text{m}$. For extinction kernels, the shorter

lidar wavelengths are characterized by a relatively narrow but smoother radius range of influence ($0.1 \mu\text{m} - 5.0 \mu\text{m}$) compared to backscatter. Extinction at the $10.6 \mu\text{m}$ wavelength retains a strong influence for particle sizes up to $10 \mu\text{m}$ and this influence does not decrease until the sphere radius exceeds $10 \mu\text{m}$ and diminishes in a manner similar to the other wavelengths. The markedly different behavior at $\lambda = 10.6 \mu\text{m}$, compared to the shorter wavelengths, is likely due to the large imaginary component of the refractive index for ice and its strong component of ice particle absorption.

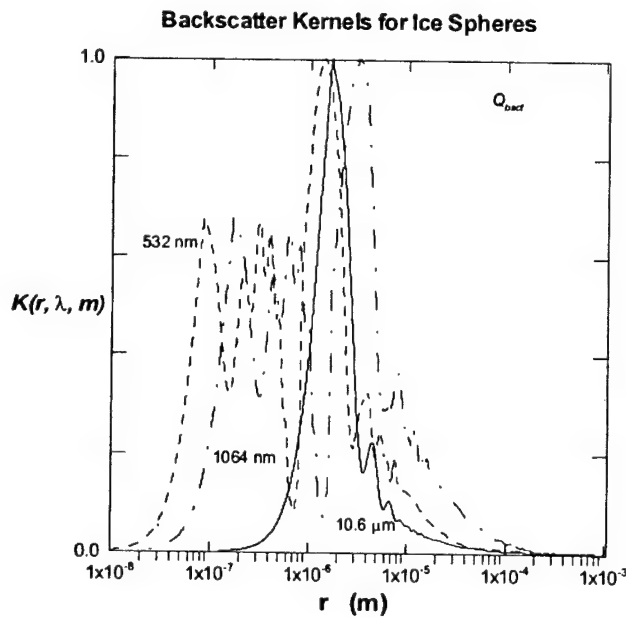


Figure C1. $K_{\pi}(r, \lambda, m)$ (normalized) for wavelengths $\lambda = 0.532 \mu\text{m}$, $1.064 \mu\text{m}$, and $10.6 \mu\text{m}$.

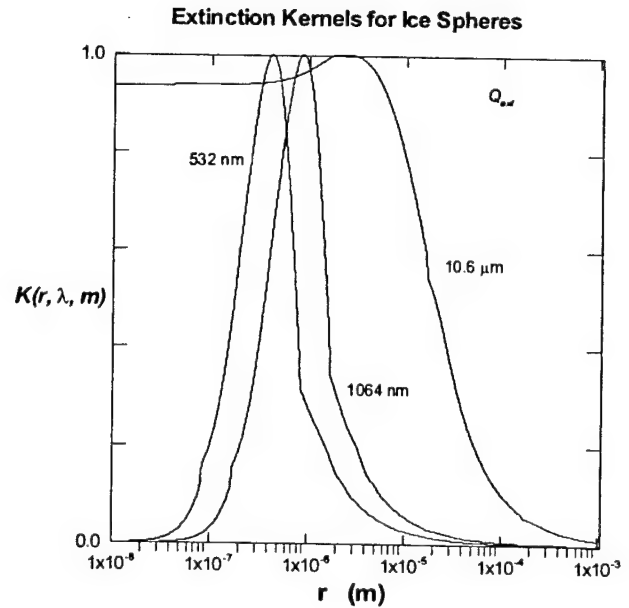


Figure C2. $K_{\text{ext}}(r, \lambda, m)$ (normalized) for wavelengths $\lambda = 0.532 \mu\text{m}$, $1.064 \mu\text{m}$, and $10.6 \mu\text{m}$.

Reference

Qing, P., H. Nakane, Y. Sasano, and S. Kitamura, 1989: Numerical simulation of the retrieval of aerosol size distribution from multiwavelength laser radar measurements. *Appl. Opt.*, **28**, 5259-5265.

APPENDIX D: RAYLEIGH BACKSCATTER CROSS-SECTION AND VOLUME BACKSCATTER COEFFICIENT FOR AIR

From van de Hulst (1957), the backscatter cross-section σ is

$$\sigma = 4\pi r^2 I(r, \theta = \pi) / I_0 \quad (m^2) \quad (D1)$$

where I_0 is the intensity of the incident light, I is the intensity of the scattered light at a large distance r from the scattering particle and θ is the scattering angle.

For isotropically polarized Rayleigh scattering, the scattering intensity is

$$I = \frac{(1 + \cos^2 \theta) k^4 |\alpha|^2 I_0}{2r^2} \quad (D2)$$

Thus

$$\sigma = 2\pi (1 + \cos^2 \theta) k^4 |\alpha|^2 \quad \text{where} \quad (D3)$$

$k = \frac{2\pi}{\lambda}$ and α is the polarization volume. α is expressed using the Lorentz-Lorenz

formula applicable to molecular optics (van de Hulst (1957)):

$$\alpha = \frac{1}{4\pi N} \frac{3(m^2 - 1)}{(m^2 + 2)} \quad (m^3) \quad (D4)$$

Here $N = \frac{N_A \rho}{M}$, the number of molecules per unit volume, where N_A is Avogadro's number, ρ is the density of air, and M is the molecular weight of air. In Eq. (D4), m is the refractive index of air, which is a real quantity. Substituting Eq. (D4) into Eq. (D3) yields

$$\sigma = \frac{9}{8\pi N^2} (1 + \cos^2 \theta) k^4 \left| \frac{m^2 - 1}{m^2 + 2} \right|^2 \quad (m^2) \quad (D5)$$

After Liou (1980), the average scattering cross-section $\bar{\sigma}$ is expressed in terms of the scattering coefficient β_{sct} (m^{-1}) and N as

$$\bar{\sigma} = \beta_{sct} / N \quad (D6)$$

If the scattering angle $\theta = \pi$, the volume backscatter coefficient can be written as

$$\beta_{\pi} = \frac{N\sigma_{\pi}}{4\pi} = \frac{9k^4}{16\pi^2 N} \left| \frac{m^2 - 1}{m^2 + 2} \right|^2 = \frac{9\pi^2}{N\lambda^4} \left| \frac{m^2 - 1}{m^2 + 2} \right|^2 \quad (m^{-1}sr^{-1}) \quad (D7)$$

References

- Liou, K.N., 1980: *An Introduction to Atmospheric Radiation*. Academic Press, New York, 392 pp.
- van de Hulst, H.C., 1957: *Light Scattering by Small Particles*. Dover Press, Inc., New York, 470 pp.